UNIVERSITY OF COPENHAGEN

Physics of non-equilibrium membranes

Feld, Kasper Emil

Publication date:
2012

Document version
Early version, also known as pre-print

Citation for published version (APA):
Feld, K. E. (2012). *Physics of non-equilibrium membranes*. Biophysics-Membranes: Faculty of Science, University of Copenhagen.

Download date: 08. apr.. 2020

Niels Bohr Institute
FACULTY OF SCIENCE
UNIVERSITY OF COPENHAGEN

PhD thesis

Physics of non-equilibrium membranes

Kasper Emil Feld

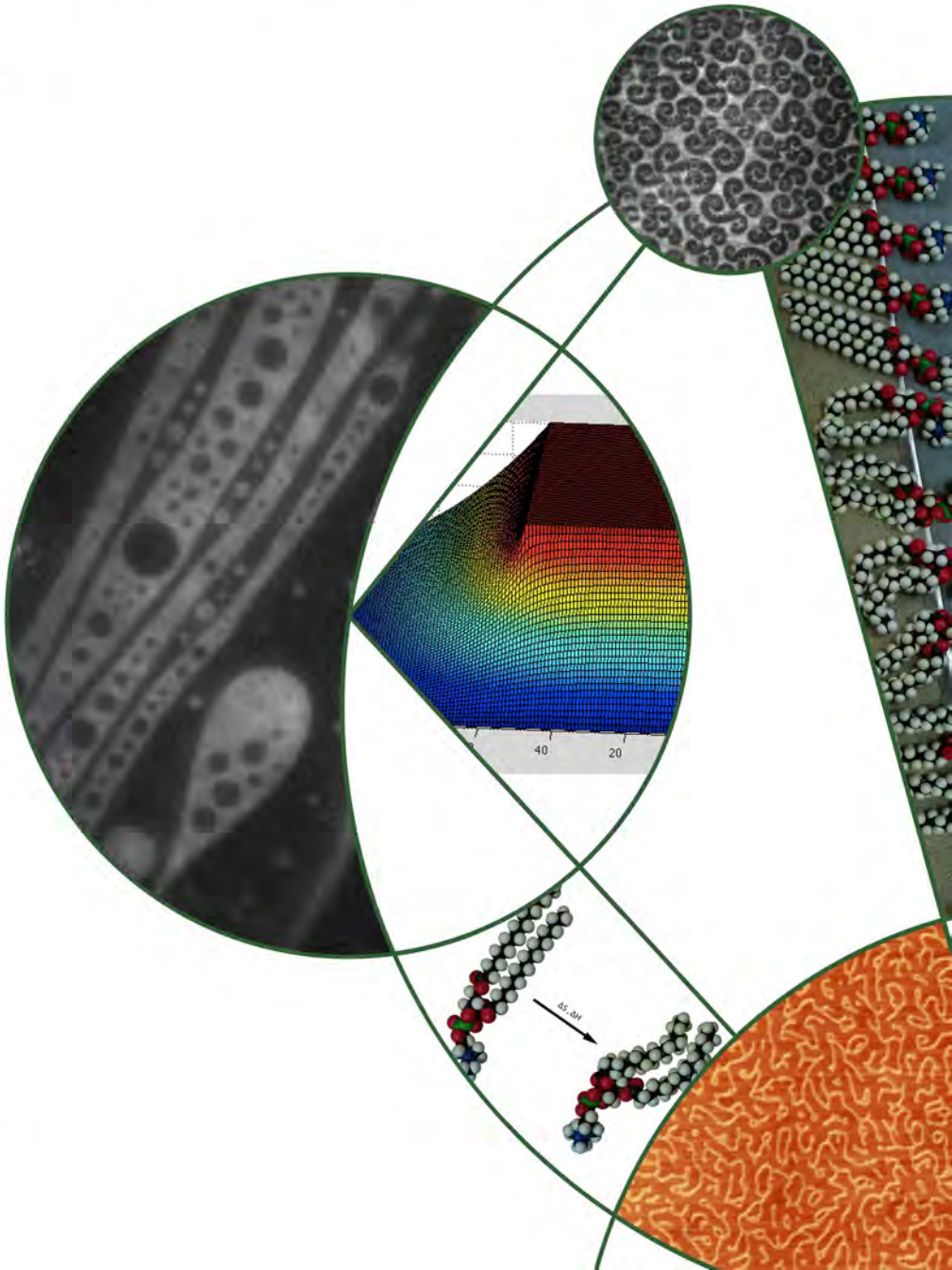

Principal supervisor:
Thomas Heimburg

Submitted march 2012

Contents

Preface

"*I am not young enough to understand everything*"

-J. M. Barrie, *The Admirable Crichton*, Act I (1903)

The present thesis describes a diverse study of the properties of the phospholipids that make up a large part of biological membranes. The majority is concerned with microscopy on Langmuir monolayers, but also bilayers is given a treatment.

The work these past three years has had its ups and downs. It is not always easy to have two advisors when their goals differ. Professor Thomas Bjørnholm got the funding for my project and therefore had a big say in the direction in which the project was taken, while the day-to-day supervision was taken care of by professor Thomas Heimburg. In 2010 Bjørnholm became prorector of the university of Copenhagen and Heimburg took over as my sole supervisor.

Structure of the thesis

The experimental part of the thesis is made up of three parts, each one concerning the thermodynamics and organization of self-assembled phospholipid structures. Most relates in some way to the controversial soliton model proposed by my advisor Thomas Heimburg.

The first chapter is a general introduction to the overarching subject, describing in broad terms the theory and motivations behind this kind of work.

The second chapter goes into detail with the general theory needed to understand multiple of the experimental chapters.

Then come the four experimental chapters, each with their own introduction, theory, materials and methods, results and conclusion subchapters. These subchapters deal with the specific theory, methods and motivations behind the part project, which is not shared by the other part projects.

The first and biggest experimental chapter deals with the morphology and organization of phospholipid Langmuir monolayers. Its theory chapter is a comprehensive review of the current understanding of such systems, especially concerning the effect that long-reaching electric fields play here.

The second experimental chapter is about the work I did at the behest of the nano-science center, which was at that time led by my second advisor Thomas Bjørnhom. It describes the attempt to qualify the organization of Gibbs monolayers consisting of protein-stabilized patches of phospholipid bilayer called nanodiscs.

The third experimental chapter moves on to true bilayers. It describes the work done during my time abroad in Cambridge, England, on giant unilamellar vesicles

The fourth experimental chapter describes the amazing regular patterns that were discovered when using atomic force microscopy to study self assembled bilayers supported on mica.

Finally comes a series of appendices describing either interesting work I've done over the years, but which is too weakly linked to the overarching subject to make it into the actual thesis; or additional technical information which would take up to much space inside a chapter, like the various Matlab® scripts which were written to analyse electronic data.

The bibliography is placed in the extreme end of the thesis, for ease of finding and since many references are used in multiple chapters, having a reference list at the end of each chapter would mean an unnecessary doubling of these references.

Acknowledgements

First of all thanks to all the people who I have reason to thank but may have forgotten or who didn't fit into these acknowledgements. Hopefully you know who you are.

My advisor Thomas Heimburgs door has always been open to seek help and advice, a fact of which I was dreadfully unaware when things in the basement got tough and experiments and equipment stopped working for months. The harshest lesson and the one that took me the longest time to understand in the process of learning how to work independently have paradoxically been when to ask for help.

I owe a great thanks to professor Andrew Jackson for his wisdom and experience, which, when I sought it, allowed him to offer me fantastic advice to get my hopes and motivations up. Without it this thesis would never have been finished.

Thanks then go to Dr. Alfredo Gonzales-Perez for his spirit and camaraderie in the lab and office for the past few months. He could always make me look on the bright side of things, and could recognize quality in my work even when I could not.

Thanks to the rest of the Biophysics of Membranes group, and to the other biophysicists of the B and C floor in the Niels Bohr Institute. It has been a privilege to be part of this friendly and spirited environment.

Thanks go to Dr. Ulysse Delabre and Professor Jochen Guck and the rest of the Guck lab at the Cavendish Laboratory in Cambridge, for welcoming me in their group, teaching me to use the optical stretcher and allowing me to use their equipment. I thoroughly enjoyed my stay abroad.

Finally I need to express my gratitude to my family and friends for their patience with me during this final time where I have been working from early morning to late night. Thanks to every one of you who read my drafts whether to offer constructive criticism or just to express interest.

Abbreviations

ACF	Auto correlation function
AFM	Atomic Force Microscopy
APD	Avalanche photo diode
BSA	Bovine serum albumin
CCD	Charge coupled device. The photosensor chip of digital cameras.
CM	Confocal microscopy
DPPC	Dipalmitoyl-phosphaditylcholine
DMPC	Dimistoryl-phosphaditylcholine
DMPG	Dimistoryl-phosphaditylglycereol
Eq.	Equation
FCS	Fluorescence correlation spectroscopy
FRAP	Fluorescence recovery after photobleaching
FRET	Förster resonant energy transfer (earlier fluorescent resonant energy transfer)
FWHM	Full width half maximum
MMA	Mean molecular area
MSD	Mean square displacement
MSP	Membrane Scaffold Protein
NA	Numerical aperture
PSI	Photosystem one.
PTFE	Poly-tetra-flour-ethylene. Commonly known by the DuPont trademark ”Teflon®”

Symbols in formulas

In general the meaning of the symbols, used in the various formulas in the thesis, are explained in the text immediately preceding or succeeding the formula itself. This is usually the case even when its usage is common standard. When the same symbols are used in the same meaning multiple times in the same chapter they are not normally explained again. Here follows, for quick reference, a list of the various meanings the symbols are used in.

a	Inner radius of glass insulated electrode
A	Area
b	Outer radius of glass insulated electrode
c	Speed of sound, speed of light.
c_P	Heat capacity (at constant pressure).
C	Concentration
d	Distance, width of domain
D	Diffusion coefficient
E	Electric field
f	
F	Helmholzt free energy, Force.
g	Gravitational acceleration
h	Dimensionless parameter of the Hodgkin-Huxley model, dispersion constant, height

H	Enthalpy, curvature.
J, J_x	Flux of chemical species
k_B	Boltzmanns constant
L	Length
n	Number of molecules, amount of substance, refractive index, Dimensionless parameter of the Hodgkin-Huxley model
m	Dimensionless parameter of the Hodgkin-Huxley model
P	Power
Q	Finite but large distance, charge.
r	Position, distance travelled
R	Universal gas constant
R_0	Radius
S	Entropy, surface area
t	Time
T, (T_m)	(Melting) temperature
v	Speed
V	Voltage
w	Width of domain
W	Work
x	First spatial dimension
y	Second spatial dimension
z	Third (vertical) spatial dimension
α	Anomalous diffusion coefficient, Gate opening rate of the Hodgkin-Huxley model
β	Gate opening rate of the Hodgkin-Huxley model, material constant as defined by Eq. 4.10
δ	Dipole moment cut-off distance
ε	Relative permittivity
ε_0	Vacuum permittivity
φ	Electrostatic potential
Φ	Area ratio of phases,
γ	Surface tension, friction coefficient.
η, (η_w)	Viscocity (of water)
κ^A	Lateral compressibility
λ	Line tension
π	$\pi \approx 3.1415$
Π	Surface pressure
θ	Angle
ρ, (ρ^A)	(Lateral) density, distance from cylindrical axis.
σ	Surface charge
τ	Lag time

1 Introduction

1.1 Membranes

The various incarnations of biological membranes play a huge role in all living organisms. Not only does every eukaryotic and prokaryotic cell have a plasma membrane which separates the interior cytosol from the surrounding medium in the form of cell membranes; but other membranes define the boundary of the various organelles such as mitochondria, chloroplasts and the endoplasmatic reticulum, they serve as anchor points for the cytoskeleton and is home for many of the important enzymes of vital biochemical pathways. There has been a tendency for the lipids that makes up the majority of many membranes to be seen as simply dumb building material. Basically lipids form a wall to separate stuff and into which to stick proteins; the proteins in turn fulfill all the important functions. This paradigm is slowly changing.

A fundamental function of membranes is to allow for a different concentration of molecules in the medium enclosed than on the outside. Despite the extreme thinness of about 5nm membranes form an especially effective barrier for ions. This is due to the hydrophobic interior. The fatty acids of phospholipids as well as the side chains of hydrophobic amino acids form an environment with a dielectric constant a factor of about 40 lower than the aqueous environments on either side. This makes the energy required to transfer charged species into the membrane prohibitively high in most cases (Paula *et al*. 1998). It is thus possible to maintain a different concentration on either side.

Phospholipids have many interesting characteristics of their own. Most lipid bilayers exhibit a main phase transition somewhere between -20 and 60 degrees C, as well as potentially several others. Evidence suggests that this phase transition is exceedingly important in biology. For example studies show that Escherichia Coli bacteria grown at a specific temperature adjust their lipid compositions so that they have the main transition at a few degrees below the growth temperature (Heimburg & Jackson 2005a).

When a membrane enters the transition, fluctuations increases drastically. Compressibility and heat capacity are greatly increased which can be proven to relate directly to fluctuations in enthalpy and area. Pores are able to form spontaneously much more easily when a membrane is in the phase transition regime, leading to permeabilities up to a factor 10^6 higher for some substances (Blicher *et al*. 2009).

1.2 History of membrane models

1.2.1 Early ideas

The earliest confirmable idea of a membrane in biological systems is from 1773 when William Hewson discovered that red blood cells are flat rather than round, therefore they could not be liquid droplets as people had previously assumed. Given they changed shape when exposed to media of different salt concentration, he supposed they were liquid surrounded by a flexible membrane. (Hewson 1773). In 1899 Overton hypothesized that the cell membrane was made primarily of lipids (Overton 1899). In 1925 Gorter and Grendel extracted lipids from red blood cells on a Langmuir trough and concluded from the area that the membrane is a bilayer (Gorter 1925).

1.2.2 Fluid Mosaic Model

In 1972 Singer and Nicholson proposed the "fluid mosaic model" (See Figure 1, A), which is still the textbook standard model and reference in literature because of its simplicity. The fluid mosaic model simply consists of a bilayer of lipids held together by hydrophobic forces and behaving like a flexible two-dimensional liquid in which membrane proteins are dissolved and can diffuse freely in the two dimensions. (Singer & Nicholson 1972)

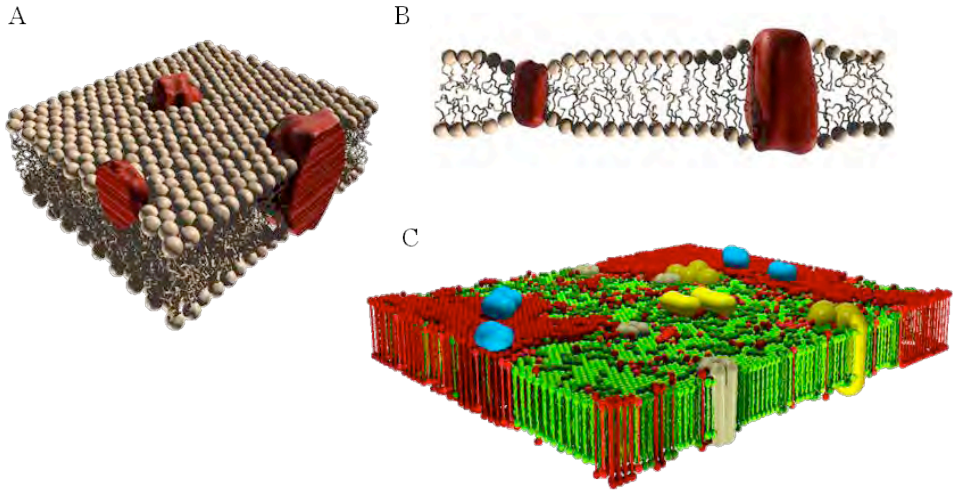

Figure 1: Various membrane models. A: The fluid mosaic model. Membrane is a flexible two-dimensional liquid with proteins dissolved. Lipids only act as a barrier for bulk solutes and as a solvent for membrane proteins. B: Mattress model taking into account variations in thickness. C: Modern picture showing complicated mesoscale organizations. Images A and B courtesy A. Blicher, image C courtesy H. M. Seeger.

1.2.3 Later developments

The most important addition to the fluid mosaic model is the idea that lipids may reorganize to accommodate membrane proteins of different sizes. In the so called mattress model proteins with a big hydrophobic domain will have less energy if the membrane is wider in their general vicinity, therefore lipids with long tail will tend to accumulate here, against their entropic tendency to mix. Vice versa around proteins whose hydrophobic domain is smaller than the native membrane thickness (
Figure 1, B). The membrane therefore acts like a spring mattress that can deform in thickness, hence the model name. This means proteins of similar size will tend to gather near each other to minimize this deformation.

The system is further complicated by things like phase transitions. Biological membranes typically exist at a temperature above their main transition in which the lipid tails changes from disordered with lots of bends to a highly ordered structure with generally straight tails. Aggregation of lipids with a higher melting point as well as local widening of the membrane as per the mattress model may cause lipids locally to enter the ordered state. A real membrane with hundreds of constituents is likely to contain several different domains of varying lipid and protein composition, and varying states of melting (
Figure 1, C). The aggregation of molecules favoring a solid state has led to the concept of the lipid raft, solid domains rich in cholesterol, floating around in the otherwise fluid membrane. Although it can be argued that “raft” might be a poor description of a formation that is likely highly dynamic and intermittent in nature, these aggregation processes are no doubt very important. Some proteins may need to be in a dimer or oligomer in order to perform their function; this may be facilitated by structuring of the lipids.

In addition to this most biological membrane are subject to a powerful electric field. Differences in concentrations of ionic solutes on either side of the membrane charge the membrane like a capacitor, producing electrical potential differences on the order of 100mV from one side to the other. Since a membrane is typically 3-4 nm thick this means that the electric field is of enormous magnitude. The effect this field has on lipids and proteins are not well understood.

1.3 Lipid nomenclature and structure

The main part of any lipid is the fatty acids. Fatty acids are long chained carboxylic acids with the general chemical structure RCOOH where the R represents a long hydrocarbon chain typically consisting of 12-20 carbon atoms. Fatty acids are rarely found alone but are most commonly linked by ester bonds to the –OH groups of a glycerol molecule. If three fatty acids are so linked the resultant

molecule is a triglyceride, which has very limited polarity, and is therefore highly insoluble in water. Triglycerides make op most of the energy storage fat of animals.

Of more interest to this thesis are the phospholipids in which only two fatty acid are linked to a glycerol, and the final hydroxyl of the glycerol connects it to a small polar group called the head group, via a phosphate ester. The phosphate is in turn linked with another ester link to the remainder head group.

Most phospholipids are commonly known under a four-letter abbreviation the first two letters refer to the fatty acids, the second two to the head group. If the two fatty acids are the same then the first letter is D for “di-“, signifying the presence of two identical parts, the second letter stands for the specific fatty acid present, for example P for “palmitoyl” or O for “oleoyl”. If the fatty acids are different both first letters signifies an acid. The most common examples for the two last letters are PC for phosphadityl choline, or PG for phosphaditylglycerol or PE for phosphadityl ethanolamine.

Since the phosphate group carries a negative charge, the entire lipid is negatively charged if the remaining head is a polar but neutral group like glycerol, and it will be neutral but switterionic if the final group is positively charged like the choline group containing a quaternary ammonium cation.

1.4 The Hodgkin-Huxley model

In 1952 Hodgkin and Huxley proposed their famous model for how the action potential of animal nerves functions (Hodgkin and Huxley 1952). It was known that potassium concentration inside cells was kept high inside cells and low outside by the protein known as the sodium-potassium pump, and vice versa for sodium. During an action potential some sodium ions move in and some potassium ions move out, relieving a bit of these concentration differences. At the same time the field across the membrane is reduced, even reversed, and subsequently restored.

Hodgkin and Huxley proposed a model for voltage sensitive protein ion channels that would open and close in such a way as to reproduce the empirically measured voltage variations during the firing of a nerve. In the popular depiction the membrane is simply regarded as a charged capacitor, connected in parallel to several batteries each corresponding to an ion species. The batteries have different voltages because each ion’s concentration gradient means it will be in equilibrium across the membrane at different voltages. Each battery is blocked be a variable resistor, representing the protein ion channels capable of opening or closing the ion current.

Each protein is postulated to have a series of voltage dependent gates stochastically opening and closing, the probability of a particular channel being open is then the

product of each individual gates probability. The opening and closing rates for each gate as a function of voltage is described by a series of functions chosen to give the best fit to the empirical data. In essence the Hodgkin-Huxley model contains some twenty independent parameters which is a priory indeterminable and must be fitted to the data. Perhaps unsurprisingly it does a very good job of matching the empirical voltage profiles, a fact Hodgkin and Huxley pointed out themselves in their original paper:

> *"The agreement must not be taken as evidence that our equations are anything more than an empirical description of the time-course of the changes in permeability to sodium and potassium. An equally satisfactory description of the voltage clamp data could no doubt have been achieved with equations of very different form, which would probably have been equally successful in predicting the electrical behaviour of the membrane.*
> *[. . .] the success of the equations is no evidence in favour of the mechanism of permeability change that we tentatively had in mind when formulating them*." (Hodgkin and Huxley 1952)

1.5 The Soliton Model

Most biological membranes have a main phase transition right below the body temperature of the organism. In the case of bacteria it has been shown that they adjust the lipid composition according to the ambient temperature to keep this true. In a phase transition several things happen. Membranes become much more permeable to solutes, heat capacity reaches a peak, fluctuations in heat, area and volume all peak, same as compressibility.

The soliton model introduced by Heimburg and Jackson in 2005 is a provocative new way to look at the nerve signal (Heimburg & Jackson 2005b). The model postulates that rather than being primarily built on the action of voltage gated channel proteins, the action potential is better described as a density pulse in the membrane of the nerve. If a membrane is compressed laterally it will cause a melting point elevation. If the temperature was only slightly above the transition to begin with it can result in parts of it changing phase. As this phase change decreases the area, it leads to a drastically nonlinear compression vs. force response curve. Combined with the natural dispersion relations of density waves in a membrane this leads to the possibility of solitons, soltitary localized waves that travel with extremely little attenuation or dispersion.

Although heavily criticized this model do offer some good points and food for thought, it may or may not be entirely correct, but this subchapter will argue that even if wrong, there is ample evidence that there is a good reason to take an extra look on the role of lipids in biological systems..

1.5.1 History of the soliton model

The soliton model was first proposed by Heimburg and Jackson in 2005 (Heimburg & Jackson 2005b). A soliton is a special kind of wave observable in many different media. It occurs whenever the effects of dispersion (wave speed depending on frequency) conspires with a nonlinear response to deformation to make a single wave that can travel the medium without spreading or changing shape, and with limited loss of energy. It was first observed by John Scott Russel when he witnessed a barge being towed on a narrow canal. When the rope broke the barge came to an abrupt stop and a wave was released traveling up the canal. He followed the wave up the canal for miles on his horseback.

As known, when a cell membrane changes state from liquid expanded to liquid condensed its area is drastically reduced. Although not strictly first order this still means than the lateral compressibility is drastically increased in the phase transition, since a little increase in pressure causes more of the bilayer to change state reducing the area much more than a corresponding pressure increase would outside of the transition.

Research shows that the main transition of biological membranes lies a few degrees below the organism's body- or growth temperature. For example bacteria grown under different environmental conditions adjust their membrane composition either in terms of carbon chain lengths or number of double bonds (Heimburg 2007a, Hazel & Williams 1990). Eukaryotes display the same kind of adaptions. Membranes in arctic seagulls and reindeer display a higher amount of double bonds near the feet or hoofs than membranes from the warmer areas closer to the main body. The effect is even seen in humans. Alcoholics are known to have higher concentrations of cholesterol and saturated fatty acids, which would compensate for the melting point depression caused by the alcohol (Benedetti *et al*. 1987 and Parmahamsa *et al*. 2004).

The fact that the adjustment happens both ways clearly indicates that it is important for biological processes that the membranes are only slightly above the melting point. If the only requirement were that the membranes stay liquid all the time then it would be a simple matter to reduce the melting point to temperatures never encountered.

All this means that biological membranes are in a regime where increased lateral pressure causes the membrane to move further into the transition and the lateral compressibility will therefore greatly increase with increasing pressure, a nonlinear response. Combined with the dispersion this makes membranes capable of hosting solitons. The theory of soliton propagation is quickly touched on in chapter 2.11 but is not the focus of this thesis.

1.5.2 *Evidence for the soliton model*

At the beginning of the twentieth century Meyer and Overton independently discovered that when plotting a molecule's potency (for example its ED_{50} value) as a general anesthetic against its olive oil/gas partition coefficient it forms a nearly perfect straight line across four or five orders of magnitude (Meyer 1901 and Overton 1901). In other words regardless of which anesthetic molecules is present the magnitude of its effect depends only on its equilibrium concentration in a fatty environment. The textbook explanation for general anesthetic is that the anesthetic

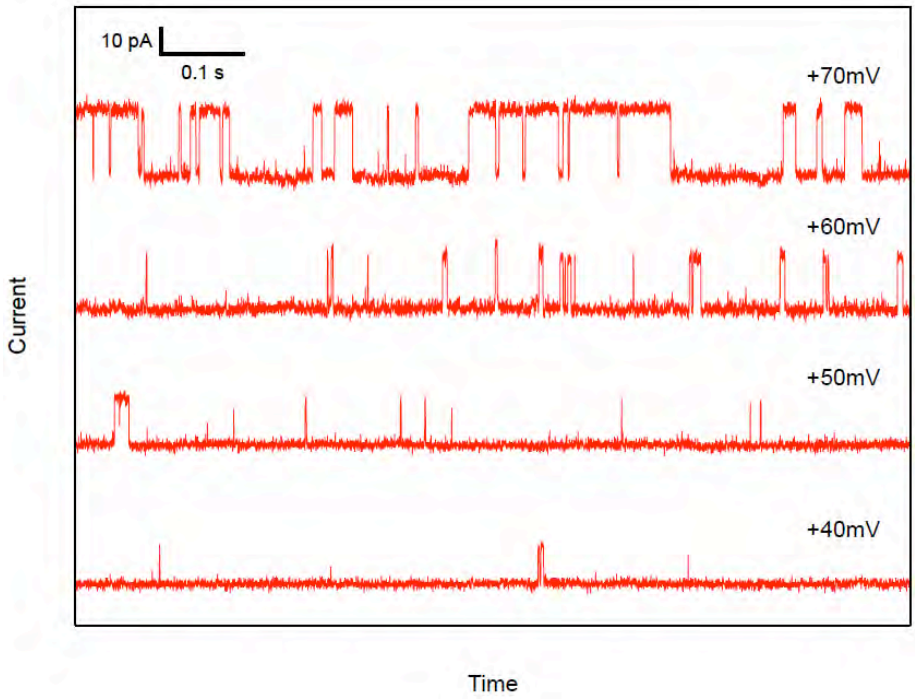

Figure 2: Figure from Blicher 2011 showing voltage gated channel formation in a pure lipid membrane. Current shifts suddenly back and forth between a high and a low state. The higher the voltage across the membrane the more prevalent is the high state.

blocks ion channel proteins or synapse receptors thereby inhibiting the nerve signal. This does not explain why molecules differing wildly in all characteristics from chemical reactivity, polarity and to physical shape and size would all follow this trend.

In the soliton model the nerve signal is dependent on the availability of the main transition of the nerve plasma membrane. A solute that dissolves preferentially in the liquid disordered phase of the membrane would lower the main transition temperature of that membrane, moving it further away from physiological temperature. This melting point depression is proportional to the concentration of

the foreign molecule; therefore the Meyer-Overton correlation would be expected from the soliton model.

It is known that other thermodynamical properties than solute concentration changes the transition temperature. The main transition of lipids is accompanied by a volume change and therefore a large hydrostatic pressure will raise the transition temperature. Experiments with tadpoles confirm that, indeed, a hydrostatic pressure will reverse the effects of general anesthetics.

A lot of the data on the properties of ion channel proteins comes from patch clamp measurements. Patch clamps are done by ripping out a part of a membrane using a glass micropipette with suction applied, so that the torn patch covers the opening of the pipette. Then the voltage/current characteristics of the membrane can be measured while varying various variables. Traditionally the membrane is here seen as simply a layer of insulator, with all interesting phenomena being ascribed to proteins. The general consensus is that many proteins form channels in their centers through which ions may flow. In a few cases such as the sodium channel such notions are backed up by crystal structure and molecular dynamics simulation, but in the majority of cases it is based on much more circumstantial evidence like patch clamps.

It is not possible to do a patch clamp experiment of a single protein; the object of the measurement is the entire patch of membrane, proteins and lipids in total. In principle it is impossible to distinguish whether a given effect is caused by the proteins or the lipids or by a synergetic effect of the whole system with such an experiment. Many might say that Occam's razor favors that the complicated proteins is responsible for the complicated behaviors seen, rather than the "dumb" lipids. However, while a patch clamp cannot be done without lipids, it *can* be done without proteins.

By covering a pipette with a pure synthetic membrane made purely of lipids one can measure the current-voltage characteristics of a piece of membrane - the background upon which the protein conduction would be assumed to be added. Such experiments show that this background is all but stable. The conduction often jumps up and down as if a channel was opening and closing. Blicher even found several to be distinctly and reversibly voltage gated (see Figure 2) (Blicher 2011).

Patch clamp measurements are notoriously unreliable. A great deal of weeding out has to be done in the data. This sets up a high risk of selection bias. If one expects to find a certain result, then it would take inhuman willpower not to preferentially select data that fitted such an expectation. This is not an accusation of scientific dishonesty, but rather a reminder of the all too human tendency to see what we want to see.

Many ion channels reported in the literature change performance drastically with temperature. As seen in chapter 2.3 sharp transitions require a large system size. In order for a change to happen across a few degrees temperature difference, the enthalphy of the change has to be on the order of 1000kJ/mol, this is comparable to the full denaturation enthalpy of an entire typical protein. For a small conformational change the associated enthalies and entropies will be much smaller and therefore not capable of explaining a proteins response to small changes like that. A big protein complex could, and a big signaling pathway with feedbacks could change state rapidly, but a single protein channel will not be able to switch from almost all open to almost all closed in response to small changes. Alternatively the proteins could be influenced by the lipids around them. Several hundred lipids cooperating can effect changes across a few degrees. There are several hypotheses to explain how general anesthesia affects the membrane system of proteins and lipids, but it remains a fact that without involving lipid thermodynamics in some way there is no explaining the effects of general anesthesia.

1.6 Objectives

1.6.1 The effects of voltage

Voltages are ubiquitous across biological membranes. Yet the effect they have on the lipids making up the majority of these membranes, are poorly understood. It is known that the nerve action potential is accompanied by changes in voltage. Large parts of this thesis is concerned with the effects of electric fields on lipids. In monolayers the far-reaching fields of the lipids dipole moments plays a huge role in the organization of phases on the meso scale. The theoretical background of this is discussed in length and illustrated with fluorescent microscope images. The organization is also greatly affected by the application of an external field as is described in chapters 2.4 and 4.1.7.

In bilayers the effects are complicated by the opposition of the two leaflets making it up, a fact which makes a theoretical treatment of the system much more difficult. Various experiments and simulations suggest wildly varying effects on the melting transition temperature by a transmembrane voltage. Not only varying by an order of magnitude or more in scale, but even in sign (Sugar 1979).

1.6.2 Monolayers

Most of the present work has been on Langmuir monolayers. That is, monolayers of amphiphiles on a water surface. Monolayers form a convenient “half membrane” with the hydrophobic tails of the phospholipids in contact with air rather than another layer of lipids. This gives control of more thermodynamic variables, in

particular surface area per molecule (mean molecular area, MMA), and the water surface is perfectly flat.

1.6.3 Nanodiscs

The controversy around ion channels and the soliton model clearly illustrates that it is important to develop ways to characterize membrane proteins in an environment as close to their natural surroundings as possible, while still keeping a degree of control allowing new things to be learned. Nanodiscs are an interesting new development in structuring lipids and proteins in a wet, warm environment, unlike the crystallized, desiccated or cryogenic methods often employed.

First published by Bayburt in 2002 (Bayburt *et al*. 2002), a nanodisc consists of a patch of lipid bilayer protected and solubilized along the hydrophobic edge by an amphifillic protein dubbed the Membrane Scaffold Protein (MSP). This protection of the edge makes the entire disc water-soluble (Denisov *et al*. 2004). The disc is in turn capable of housing a membrane protein (Raschle *et al*. 2010). Ongoing research is concerned with using electrostatic effects to crystallize such discs into a meta-lattice in which the surrounding of the individual proteins closely resemble their native membrane environment, yet they are held in well defined positions in a lattice.

2 Theory

In the following section I will show some of the key concepts and laws necessary to follow the results and discussions of this thesis.

2.1 Diffusion

2.1.1 Fick and Einstein

Here I will show the various models used to describe diffusion. Later this will be used to model the behaviour of nanodiscs adsorbed beneath a Langmuir monolayer.

In 1855 Dr. Adolph Fick (Fick 1855) postulated his first law of diffusion stating that a flux of particles goes from regions of high concentration to regions of low concentration in a rate proportional to the derivative of the concentration. In one dimension:

$$J_x = -D\frac{dC}{dx} \qquad \text{Eq. 2.1}$$

Where J_x is the flux along the x coordinate, C is the local concentration, and D is a constant depending on temperature, pressure, surrounding medium and the diffusing substance. In multiple dimensions the above can be generalized to:

$$J = -D\nabla C \qquad \text{Eq. 2.2}$$

Ficks second law, which can be rather simply derived from the first (and local conservation of particles) describes how concentration of particles changes over time:

$$\frac{\partial C}{\partial t} = D\frac{\partial^2 C}{\partial x^2} \qquad \text{Eq. 2.3}$$

Of course in multiple dimensions the double derivative in eq. 2.3 is replaced by the Laplace operator.

In 1905 Einstein re-derived Fick's laws from Brownian motion (Einstein 1905). He also derived the mean square displacement of a single particle

$$\left\langle x^2 \right\rangle = 2Dt \qquad \text{Eq. 2.4}$$

which is valid when observation time is long compared to the individual movements of the particles. In multiple dimensions the mean square displacement $\langle r^2 \rangle = \langle x^2+y^2+... \rangle$ increases by 2Dt for each extra dimension.

Figure 3 shows how the differential equation of Ficks law matches with the Brownian motion of individual particles.

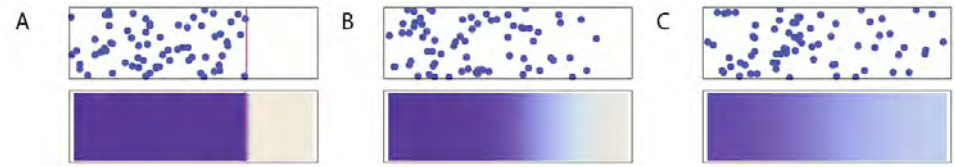

Figure 3: Macroscopic and microscopic diffusion. The top picture series shows three time snaps of a number of individual particles simulated to move randomly through Brownian motion I a box. In (A) they are confined to one part of the box by a wall, behind the wall the concentration of particles shows stochastic fluctuations around the mean value. When the barrier is removed (B) and (C) the particles spread out, but there is still a tendency towards higher concentration in the back end. In the limit of infinitely many infinitely small particles all randomness disappears and the diffusion follows Fick's laws. (Illustration copied from a puplic domain figure by an anonymous author.)

In the same 1905 paper Einstein also calculated a value of D for spheres in a liquid solution, which is often used as an approximation even for non-spherical objects. The now well-known Stokes-Einstein equation:

$$D = \frac{k_B T}{6\pi\eta r} \qquad \text{Eq. 2.5}$$

where k_B is the Boltzmann constant, T is the temperature, η is the viscosity of the liquid and r is the radius of the solute particles. The formula usually gives correct order-of-magnitude estimations for diffusion coefficients for everything from small organic molecules to proteins, or lipid nanodiscs (see chapter 4.2), even if the objects are not sperical

In the case of monolayers on a surface the same principle applies. The diffusion constant is equal to the thermal energy divided by the friction coefficient γ:

$$D = \frac{k_B T}{\gamma} \qquad \text{Eq. 2.6}$$

with γ defined by the friction F the object feels at low speeds v:

$$F = \gamma \cdot v \qquad \text{Eq. 2.7}$$

For a patch of monolayer large enough that the friction within the surrounding monolayer can be neglected compared to that arising from the viscosity of the subphase the friction coefficient becomes (Heckl *et al*. 1988):

$$\gamma = \frac{16\eta_w}{3} r \qquad \text{Eq. 2.8}$$

Where η_w is the viscosity of the subphase. This makes the diffusion coefficient

$$D_{2D} = \frac{3k_B T}{16\eta_w r} \qquad \text{Eq. 2.9}$$

2.1.2 Non Fickian diffusion

Not all diffusion follows the above laws. They assume a homogenous medium, which is rarely present in biological systems. In reality biological systems are full of inhomogeneities which forms obstacles, compartmentalizations, etc. For example a solute may diffuse easily through intercellular medium, but much slower in the crowded cytosol within a cell, crossing a plasma membrane may again take much longer time than the time scale to diffuse across a cell, all this will very much complicate an analysis of diffusion through multicellular tissue.

A special case is a medium that is locally homogenous on a small scale, on the mesoscale contains some obstacles, but is again homogenous on a large scale. In such a case the observed diffusion coefficient depends heavily on the size of the observation volume. If looking at a small observation volume between obstacles one observes the raw- or micro-diffusion coefficient and the obstacles have no effect. On a longer timescale the effects of obstacles will average out (just as the individual Brownian bumps averages out for normal diffusion) and a slower macro-diffusion is observed. In between these regimes diffusion will often appear to follow a modified power law version of Ficks first law:

$$\left\langle r^2 \right\rangle = 4Dt^{\alpha} \qquad \text{Eq. 2.10}$$

where $0 < \alpha < 1$. This is also called subdiffusion (see Figure 4).

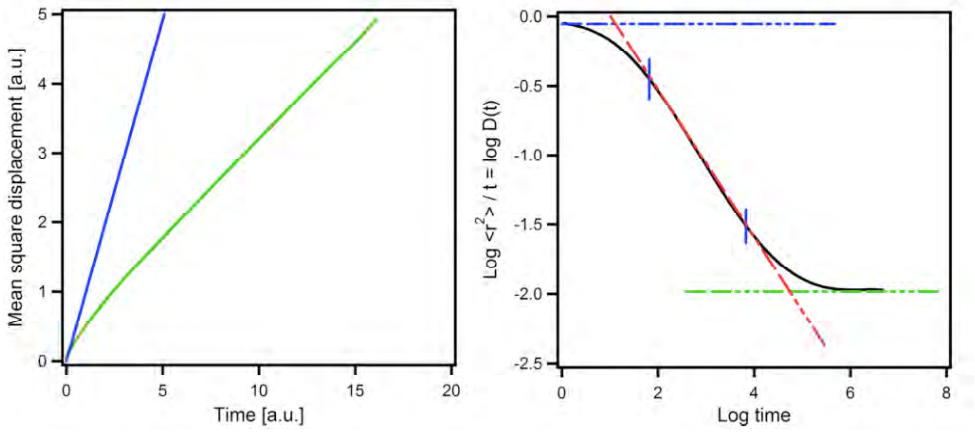

Figure 4: Different kinds of diffusion. Left: The blue line represents regular Fickian diffusion with a linear relation between mean square displacement and time; the green line shows a subdiffusion with a nonlinear dependence for small times eventually reaching a linear dependence with a smaller proportionality constant. Right: Log/log plot showing the different regimes of anomalous diffusion. On a plot like this regular diffusion makes a horizontal line. Normalized to D=1 (log(D)=0), for short timescales shown with the blue line, subdiffusion gives a line with slope α-1 highligted on intermediate timescales with the red line, at long timescales the subdiffusion ends and normal diffusion is resumed with a diffusion coefficient two orders of magnitude lower. (Plot adopted from Saxton 2007)

2.1.3 Free volume model

In 1913 Batchinsky conjectured that viscosity could be described as a function of "*relative volume of molecules per unit of free space"* (Batchinsky 1913), and in 1951 Doolittle succeded in doing this (Doolittle 1951). He found good empirical agreement with a simple formula:

$$\eta = Ae^{B/(\Delta v / v_0)} \qquad \text{Eq. 2.11}$$

where $\Delta v/v_0$ is the ratio between the volume of liquid extrapolated to zero Kelvin (without phase change) and the extra volume the liquid occupies at the actual temperature because of thermal expansion. A and B are constants depending on the specific substance. Doolittle found excellent agreement with this rule for a variety of hydrocarbons over most of their liquid range of temperatures, though diverging slightly as the temperature approached their freezing point.

Cohen and Turnbull explained this relation by modeling liquid molecules as a collection of hard spheres (Cohen & Turnbull 1959). Usually the spheres are locked in place by each other in a crystalline arrangement, although without long-range order. The extra volume present between the molecules moves around due to thermal fluctuations. Occasionally there is enough room near a molecule for it to be able to change its place. The probability of this happening in any given time period

depends exponentially on the free volume available, thus explaining Doolitles relation.

2.1.4 Free area model for monolayers

In two dimensions, such as Langmuir monolayers, the free volume model can be changed to a free area model simply by substituting all volume terms with area terms. Gudmand showed that this model is in good agreement with experiment for diffusion in DMPC monolayers (Gudmand 2008). It will later in this work be used to describe the diffusion of protein-encircled patches of lipid bilayer known as nanodiscs (see Figure 5).

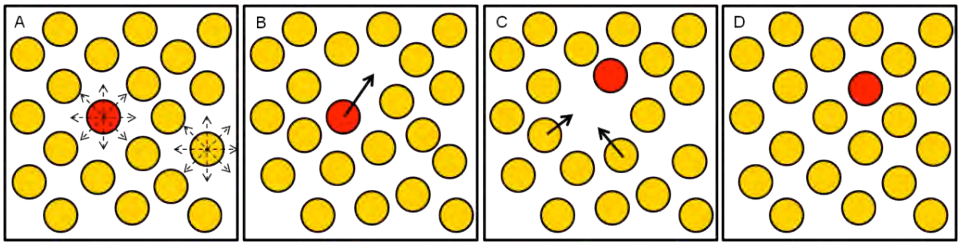

Figure 5: Free area model for nanodiscs adsorbed under a charged monolayer (see chapter 4.2). A: Initial situation. Discs are in constant Brownian motion due to being surrounded by water. They move with a microscopic diffusion coefficient expected to be similar to their bulk solution diffusion coefficient, but the crowding locks them in place. B: Ocassionally other discs move far enough to allow for a disc to change place. C: Hole closes behind moved disc. D: Original situation restored, marked disc has moved. Figure taken from Gudmand 2008, there used to describe lipids in a monolayer.

2.2 Thermodynamics and phase transitions

A phase transition is whenever a systems free energy or one of its derivatives has a discontinuity. Phase transitions occur everywhere in nature, from the familiar cases like the melting of ice to the slightly more obscure such as the transition from paramagnetism to ferromagnetism, or from normal conductivity to superconductivity. Phase transitions are usually accompanied by rapid jumps in a variety of physical variables.

The first classification of phase transitions was made by Paul Ehrenfest who labeled them according to the derivatives of the systems free energy with respect to some thermodynamic variable (Ehrenfest 1933). A first order phase transition was then a point at which the first derivative was discontinuous. In a second order transition the first derivatives are continuous but there is a discontinuity in the second. The modern definitions have changed this a bit, because there are cases where the Ehrenfest classifications do not apply; specifically when the derivatives diverge. Instead a first order phase transition is a transition involving a latent heat of transition. The classic example would be the transition between water and ice. There is no stable state midway between water and ice. Partially melted ice would

carry a large entropy penalty over liquid water because of the partial ordering, and it would have a large enthalpy penalty over ice from broken hydrogen bonds. Rather the two states represent local free energy minima in the state space one only slightly lower than the other. At the phase transition the system becomes bi-stable. Changing the temperature (or pressure etc.) an infinitesimal amount makes the other phase favorable and the system snaps to the other state instantly (instantly in phase space, the actual time required to reach the equilibrium state may approach infinity). A large amount of entropy is then exchanged for enthalpy, keeping the free energy change small.

Second order phase transitions does not involve a heat of transition, rather it has discontinuities in characteristica that are themselves derivatives such as compressibility or permeability. They may happen as one phase may become increasingly more like another as a variable is changed. Eventually it is unable to change any more and a kink happens in the graph of some properties as function of the changed parameter. An example would be the disappearance of magnetization of a ferromagnetic material as it is heated above the Curie temperature.

While second order phase transitions do not involve an enthalpy of transition, in some cases the distinction can be hard to make. A phase may change into another with an extremely much higher heat capacity, which then promptly drops off, making the distinction between a true first-order transition with a delta function spike in heat capacity and a second order transition with merely a narrow peak, hard to make in practice. For a more comprehensive review of the history and the subtleties of phase transition classification refer to (Jaeger 1997).

2.2.1 Cooperativity and width of transition

In reality the first order transition is an ideal theoretical case, only realizable in infinite systems; the so-called thermodynamic limit. A bistable system with an enthalpy of melting of ΔH and an entropy of melting of ΔS will have a melting[1] point

$$T_m = \frac{\Delta H}{\Delta S} \qquad \text{Eq. 2.12}$$

at which the probability of the system being in either state is equal. Away from the transition, the probability of either state is given by the Boltzmann distribution, so the equilibrium constant, equal to the probability of one state over the probability of the other is given by:

$$K = e^{\frac{-\Delta G}{RT}} \qquad \text{Eq. 2.13}$$

[1] Or boiling, or any other kind of transition. Melting is used here because it relates most to lipids.

where ΔG is the molar Gibbs free energy of transition, R is the universal gas constant and T is the absolute temperature. So near the phase transition the system will fluctuate from one state to the other. The smaller the system the wider this region of fluctuations will be. Only in the thermodynamical limit of infinite system size will a transition be truly first-order. If one instead considers an infinite ensemble of finite systems then the fluctuations will average out, but the transision will still have a finite width. For example heat capacity will spike but never become infinite:

$$\ln K(T) = \frac{-\Delta H}{RT} + \frac{\Delta S}{R} \Rightarrow RT^2 \frac{d \ln K}{dT} = \Delta H \qquad \text{Eq. 2.14}$$

The mean enthalpy change per mole is given by:

$$\overline{\Delta H(T)} = \Delta H \cdot \frac{K(T)}{1 + K(T)} \qquad \text{Eq. 2.15}$$

This gives a heat capacity, at constant pressure, of:

$$c_P = \left(\frac{\overline{\Delta H}}{dT} \right)_P = \frac{\exp(-\frac{\Delta G}{RT})}{(1 + \exp(-\frac{\Delta G}{RT}))^2} \cdot \frac{\Delta H^2}{RT^2} \qquad \text{Eq. 2.16}$$

The FWHM of the heat capacity spike is inversely proportional to the ΔH of transition (for sufficiently large ΔH), given that the transition temperature remains constant (Figure 6).

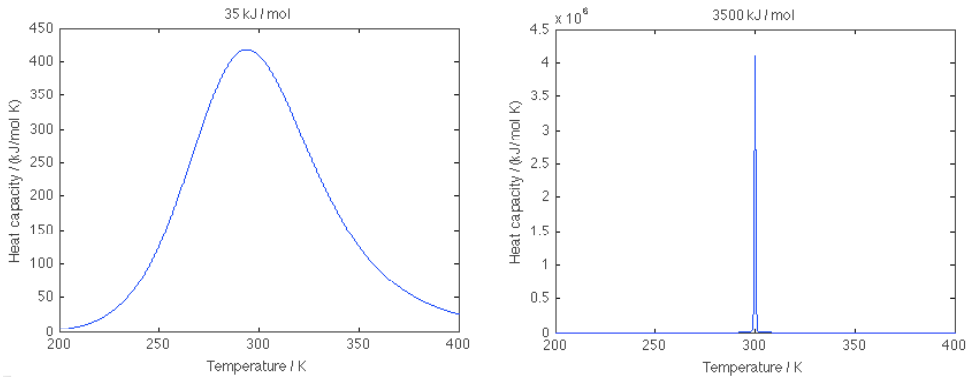

Figure 6: Effect of cooperation on transition width. Theoretical heat capacity stemming from a transition at 300K, the first in uncooperating units with a melting enthalpy of 35kJ/mol, comparable to that of a single phospholipid; the second diagram with a unit size a hundred times greater.

2.3 Transitions in lipid bilayers

Carbohydride chains have a many possible conformations. Rotation around any carbon-carbon single bond is normally called free, but the energy does vary somewhat with the angle (Figure 7). Energy is increased as the bonds are rotated so that the bond on atom one lines up with the bonds on atom two, the so-called eclipsed conformations. This leaves three minima where the bonds fall into the holes between each other, called the staggered conformations. The transition energy between these states is about 6 times the thermal energy at room temperature, meaning that transitions happen but the vast majority of molecules will be close to the staggered conformation at any given time. Because one bond on each atom is (excluding ends of chains) not a hydrogen atom, but rather the remaining chain, the three staggered conformations are not equal. Steric hindrance raises the energy of the conformation where the chains are close to each other (called the gauche conformations) by about 2.5 kJ/mol compared to the trans conformation where the chain zig-zags regularly. Instead the gauge conformations are twice degenerate raising the entropy, so as temperature is increased it is expected to see more bonds in the gauge conformations, All trans chains form neat zig-zag shapes that pack well between each other, this gives a great amount of cooperativity not just between bonds but between multiple molecules as well. A

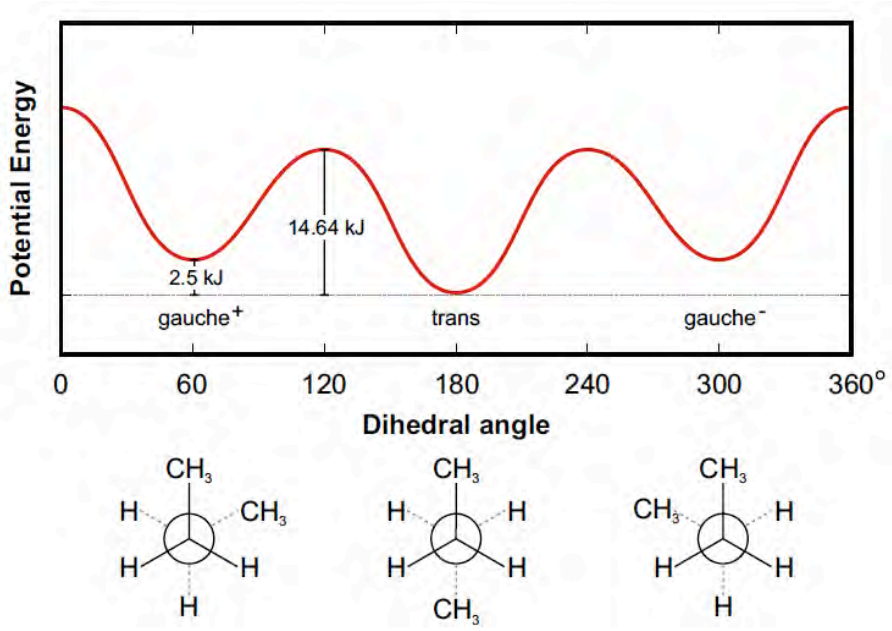

Figure 7: Top: Variation in the energy of butane as it is rotated around the central carbon-carbon bond. Longer carbohydride chains display similar variations with roation around their central bonds. Bottom: Fischer projection of the three staggered conformations, two carbon atoms cover each other in the middle and the side groups of the top atom is shown with solid lines the bottom ones with dashed lines. At 0, 120 and 240 degrees (not shown) these side groups would cover each other as well, explaining the name eclipsed for these transition conformations.

single bond switching to gauche conformation would disrupt the crystal structure in the entire area giving a large increase in entropy, but allowing the others around to randomize as well at a lower cost (Figure 8).

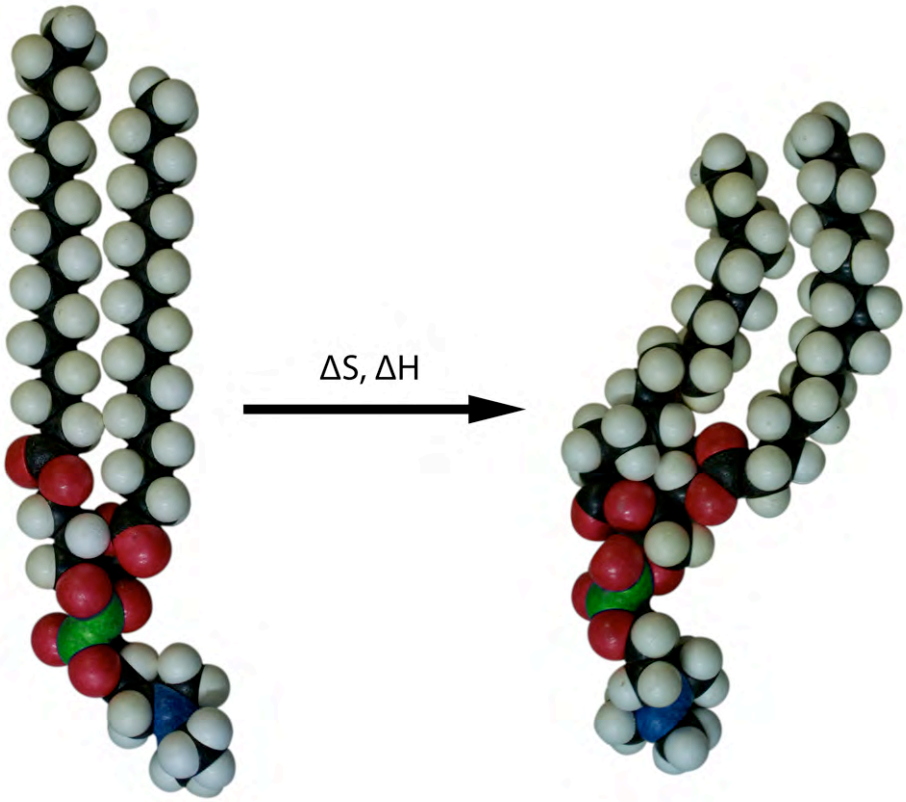

Figure 8: Molecular model of DPPC illustrating the transition from an ordered all-trans configuration to a disordered random state. This transition in accompanied by an increase in both entropy and enthalpy.

2.3.1 Fluctuations

Moving to a more general case with not necessarily just a single phase transition, the average enthalpy of an ensemble of systems will be the sum of the enthalpy of each possible state times its Boltzmann probability:

$$\overline{H} = \sum_i H_i P_i = \frac{\sum_i H_i \exp(-H_i / RT)}{\sum_i \exp(-H_i / RT)} \qquad \text{Eq. 2.17}$$

Differentiating this with respect to temperature gives an expression for the heat capacity at constant pressure:

$$c_p = \frac{d\langle H \rangle}{dT} \Leftrightarrow \qquad \text{Eq. 2.18}$$

$$c_p = \frac{\sum_i \frac{H_i}{RT^2} H_i \exp(-H_i/RT) \sum_i \exp(-H_i/RT) - \sum_i \frac{H_i}{RT^2} H_i \exp(-H_i/RT) \sum_i H_i \exp(-H_i/RT)}{\left(\sum_i \exp(-H_i/RT)\right)^2} \Leftrightarrow \qquad \text{Eq. 2.19}$$

$$c_p = \frac{\langle H^2 \rangle - \langle H \rangle^2}{RT^2} \qquad \text{Eq. 2.20}$$

The average of the enthalpy squared minus the average of the enthalpy, squared; is of course the fluctuations in enthalpy. This relation means that heat capacity is proportional to the fluctuations of the system. Heat capacity is given by the mean square deviation from the most likely enthalpy.

Similar relations exist for other variables. For example compressibility is proportional to fluctuations in volume, and area compressibility is proportional to fluctuations in area (Figure 9).

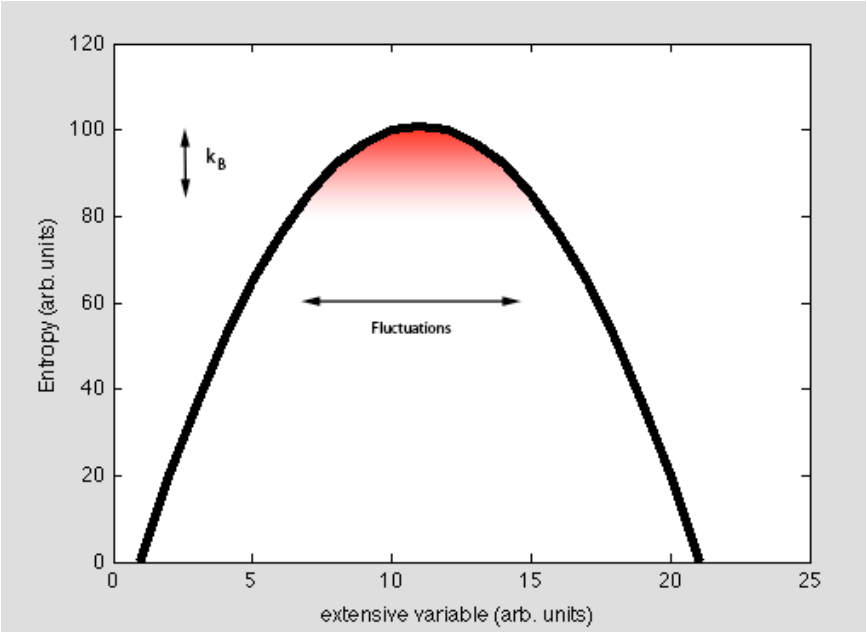

Figure 9: Any extensive variable will fluctuate around the value producing the maximal entropy for the system. The less sharp this dependence is the larger the fluctuations.

This plays a large role in the permeability dependence of a membrane with temperature. Lipid membranes are capable of spontaneously forming pores. In order to form a pore a certain area has to be evacuated of lipids. This happens much more often when the compressibility and area fluctuations are high, in fact permeability has been found to be perfectly proportional to the excess heat capacity due to phase change in lipid bilayers (Blicher 2011).

2.4 Monolayers

2.4.1 Surface tension

Pure water has a surface tension of 72.8 mN/m or equivalently 72.8 mJ/m^2 at room temperature. This is the free energy cost of producing new water surface. This cost comes about because water on the surface is unable to fully interact with neighboring molecules, like it would in the bulk. A certain ordering near the surface can reduce energy, but this instead entails a reduced entropy. The end result is a minimum cost of free energy for new surface called the surface tension.

$$\gamma = \left(\frac{\partial F}{\partial A} \right)_{T,V,n} \qquad \text{Eq. 2.21}$$

Where T is the temperature, V is volume and n is the amount of substance of the liquid. Surface tension of liquids depend heavily on temperature, generally decreasing quickly with increasing temperature, reaching zero at the critical point were gas and liquid phases becomes one (Holmberg 2006).

2.4.2 Surfactants

The surface tension of water is much larger than that of most other liquids owing to the powerful hydrogen bonds in liquid water. Nonpolar substances interact much weaker with each other and therefore the energy cost of exposing surface of a nonpolar substance tends to be much lower.

Many chemical compounds are therefore *surface active* on the surfaces of water. A molecule that contains large non-polar parts will tend to be very little soluble in water as doing so would expose water molecules to atoms they are not able to interact fully with, once again costing energy in the form of lost hydrogen bonds (the hydrophobic effect). If, however, said molecule contains a small polar or ionic part then there is a lot of energy to be gained by allowing this part to interact with water by forming hydrogen bonds and reducing electrostatic energy due to waters high polarizability. Molecules like this will therefore tend to spread along any water

surface that is already present. Such molecules are called surfactants – short for SURFace ACTive AgeNTS (Holmberg 2006).

2.4.3 Langmuir technique

Surfactants can be spread on a water surface in a controlled way by dissolving them in a volatile organic solvent and applying this solution in small droplets to the surface of water in a specially designed trough. The solvent will evaporate and leave a monolayer of surfactant behind. If the surfactant is sufficiently insoluble in water the MMA can be controlled by moving a barrier across the surface while letting the water move freely underneath. As surfactants lower the free energy of water surface, they lower the surface tension. Surface tension can be measured by suspending an object from a sensitive balance and letting it hang into the water (Petty 1996).

Over a wide range of parameters such monolayers acts like a completely two-dimensional system. The intensive variable Π, surface pressure, is defined as the reduction of surface tension γ beneath the normal level γ_0 at the given temperature.

$$\Pi = \gamma_0 - \gamma \qquad \text{Eq. 2.22}$$

Thus pure water corresponds to a two dimensional vacuum, with a surface pressure of zero, and any addition of substance to the surface will lead to an increase in pressure (for brevity I use pressure for both surface pressure and regular three dimensional pressure, p, since it is usually clear from context which one is referred to, where this is not the case I will qualify with either surface or 3D). By varying the MMA with the barriers while measuring Π and keeping the temperature constant one obtains a Π-A isotherm which can tell a lot about the organization of molecules at the surface. Figure 11 shows the qualitative behaviour of the surface pressure of a typical phospholipid (drawn to match the ideal behaviour of DPPC closely), Figure 10 shows an actual recorded isotherm for DPPC along with its compressibility defined as:

$$\kappa = \frac{1}{A}\frac{\partial A}{\partial \Pi} \qquad \text{Eq. 2.23}$$

Some very often-studied surfactants include fatty acids (carboxylic acids with long alkyl chains, typically from ten to more than twenty) and phospholipids. Phospholipids are the main constituent of most biological membranes, and fatty acids are some of the simplest molecules that form stable monolayers. Both lipid and fatty acid Langmuir monolayers typically go through several phase transitions as the MMA is reduced (Petty 1996).

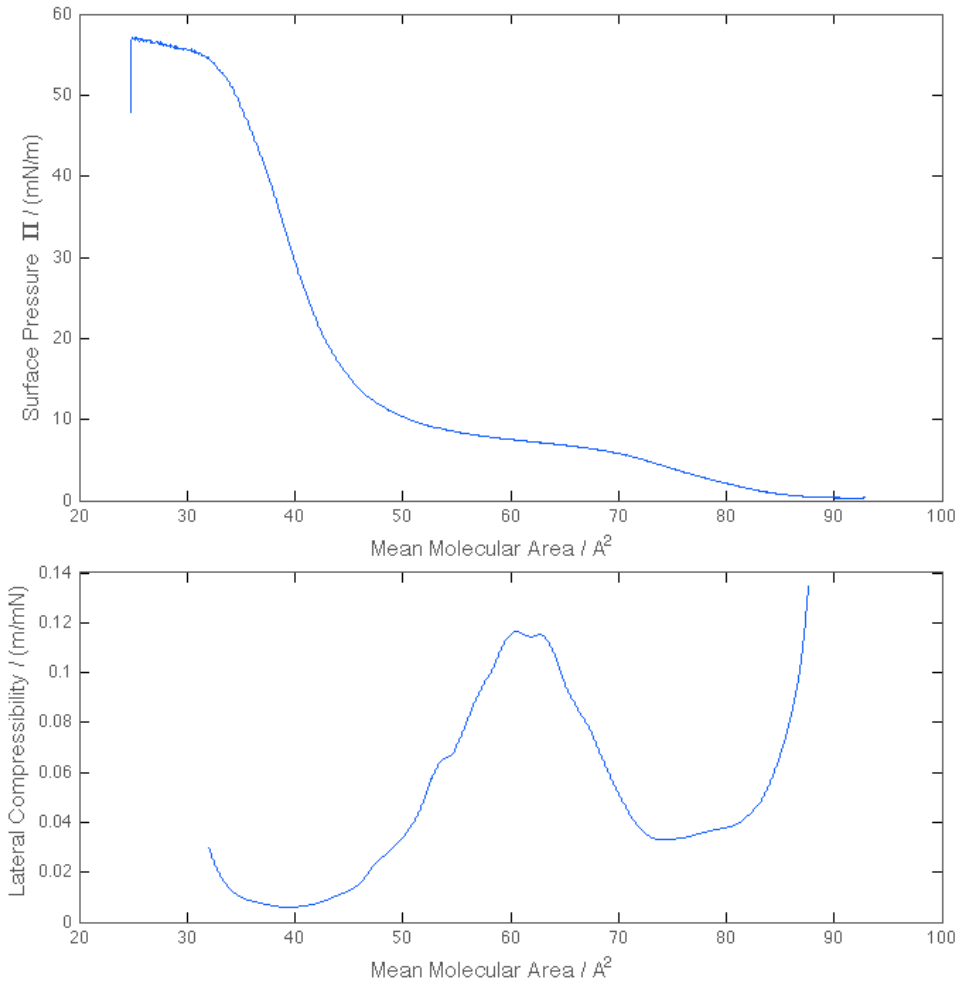

Figure 10: Top: Surface pressure versus mean molecular area isotherm for DPPC at 21 degrees C. Starting from just outside the regime of pure LE phase and ending with collapse of the monolayer beginning around 40mN/m. Bottom: Lateral compressibility calculated from the data above.

Just like the three-dimensional counterpart, at sufficiently high MMA the area taken up by the molecules themselves will be negligible and any surfactant will behave like an ideal two-dimensional gas, with no interaction happening. In this case the system will follow a 2D version of the ideal gas law with Π and A replacing p and V:

$$\Pi A = nRT \qquad \text{Eq. 2.24}$$

It may be counter-intuitive that the surface pressure does not at all depend on the nature of the molecule on the surface, since some molecules would give a much higher energy gain on the surface than others. Here it is necessary to keep in mind that the definition of surface tension (and by extension pressure) depends on the

derivative of energy with respect to area for constant amount of surfactant, not on the actual energy per surfactant.

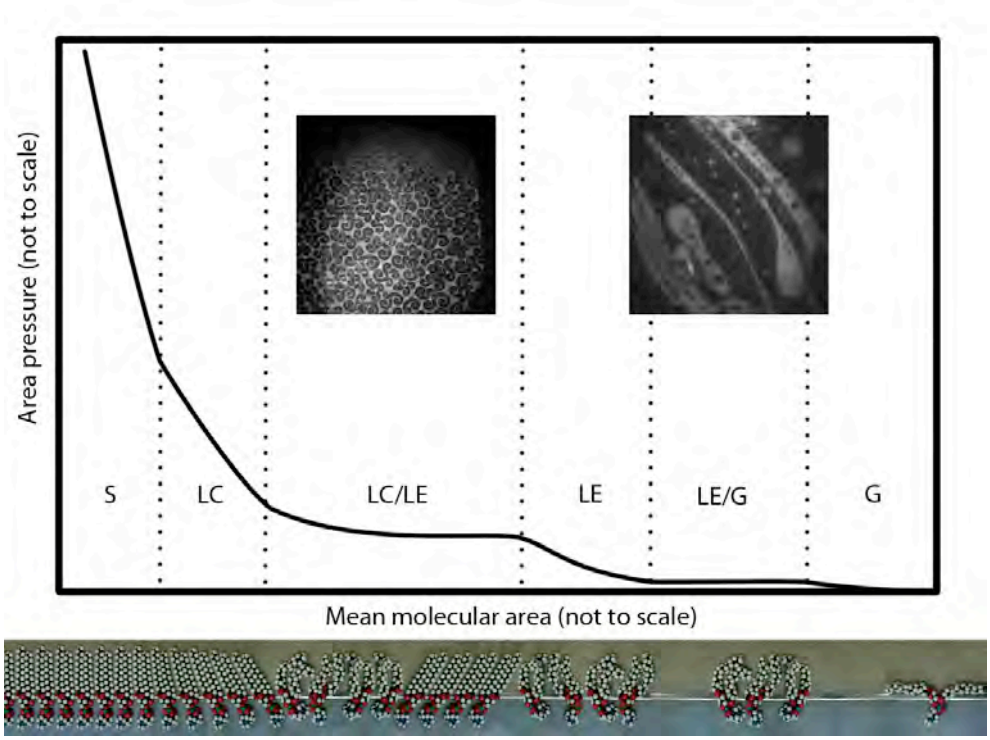

Figure 11: Qualitative description of a typical lipid monolayer isotherm. Showing how the isotherm develops across the various phases. The shape is qualitatively correct and approximately quantitative too, except that the LC/LE coexistence region is extremely contracted and the pressure drop in the gas phase is exaggerated. Inset is examples of (far from equilibrium) pictures of the two coexistence regions that give good contrast in fluorescence microscopy. In both cases the fluid or LE phase shows up as light. When approaching equilibrium both coexistence regions tend toward a plain hexagonal "dotted" appearance, and can be very difficult to tell apart from a picture. The lower bar illustrates how the molecule conformations change with the reduced MMA. This is for rough illustration only and not intended to be an accurate representation.

Just like for real gasses, as the density increases, attractive interactions generally lead to non-ideal behavior and eventually a phase transition is reached. With all but the smallest surfactants this first transition happens at a surface pressure that is still too small to be measured. However, the coexistence region of these phases can be examined with fluorescence or Brewster angle microscopy. The condensed phase produced has historically been called liquid expanded. It is very analogous to a two dimensional liquid. A difference is that the pseudo two-dimensional nature allows electrical dipole moments perpendicular to the layer, giving rise to long-range repulsive interactions changing phase transitions away from being purely first order. Complicated morphologies both in equilibrium and especially in non-equilibrium arise from the competition between minimizing these repulsive

interactions and minimizing line tension – the two-dimensional pendant to surface tension.

Upon further compression eventually the LE phase closes up and covers the entire surface. All evidence suggests that in this phase monolayers are completely isotropic and homogenous. At this point surface pressure begins to rise measurably with decreasing MMA. Next most surfactant monolayers typically enters a phase historically called liquid condensed, though it is actually a solid in that the molecules arrange themselves in a hexagonal crystalline order. Because the phospholipid heads including hydration spheres take up more space than their tails the tails adopt a tilted orientation in order to close the gaps between them. A more fitting name might be solid tilted, here I shall stick with convention and refer to it as the liquid condensed (LC) phase or simply the gel phase. The phase transition is accompanied by an increased compressibility, though rarely the infinite compressibility expected from a first-order transition.

The next phase transition is usually distinctly second order. As the LC phase is compressed more and more, the headgroups are moved closer and forced to gradually give up their hydration sphere, at the same time the tails enters a more and more upright position. Eventually the tails stand perpendicular to the surface and since they can no longer adjust their tilt this marks the entrance to a domain of very low compressibility where the surfactants cannot be packed closer and compression predominantly comes from pressing them further into each others repulsive Wan der Waals spheres. Finally a collapse of the monolayer occurs and various 3D phases results. The layer folds into multilayers or full 3D crystals, or it enters the subphase as micelles or bilayer vesicles.

Supposedly surface monolayers are really only metastable with respect to the 3D crystalline phase across a wide range of surface pressures. However, own data saw surface pressure of a monolayer increase beyond 40mN/m upon addition of some solid DPPC crystals.

2.4.4 Dipole moments of lipid monolayers

Most Langmuir monolayers posses a dipole moment perpendicular to the water surface. These can be measured with a vibrating plate capacitor also known as a Kelvin probe. A small metallic plate (typically a few millimeters in radius) is positioned close to the surface and vibrated so that the distance to the surface varies periodically (typically by a few hundre microns). The voltage drop across the surface can be inferred from the current resulting from the changing capacitance. For a detailed theoretical description refer to (Porter 1937). The measured voltage V depends directly on the dipole moment density μ.

$$V = \frac{\mu}{\varepsilon\varepsilon_0} \qquad \text{Eq. 2.25}$$

where ε_0 is the vacuum permittivity and ε is the relative permittivity of the surrounding material. This presents a problem in that the relative permittivity of water is about 80 and this drops across the monolayer to 2-4 in the organic region and only very slightly above one in the air above. This makes it very hard to make any quantitative predictions from dipole moments and surface potential measurements.

For example, it is natural to assume that the dipole moment of a lipid like DPPC would be mostly due to the switterionic headgroup. However from the measured surface potentials of hundreds of millivolts one estimates a dipole moment per lipid of about 1 Debye if disregarding ε, whereas the dipole moment of the head groups would be on the order of 15 Debye (Möhwald 1990). (One Debye per 100 square Ångstrøms corresponds to $3.34 \cdot 10^{-12}$ C/m giving a field of 377mV.)

Moreover the measured dipole moment has the wrong sign. Evidently the dipole of the switterion is well screened by the subphase, and something else is the cause of the surface potential. A likely candidate is the carbonyl group of the esters. A glycerol diester will contain two carbonyl groups and it is likely that the oxygen will on average be positioned slightly lower in the monolayer. The carbonyl groups would carry a dipole moment of about 3.6 Debye, therefore they would only need a tilt of about 20 degrees. Another easily overlooked part that might contribute is the methyl termination of the aliphatic tails. Vogel and Möbius found a contribution of 0.35 Debye from these (Vogel & Möbius 1988).

Another potential contributor is the possibility of reordering of water molecules. Pure water posses a surface potential due to structuring of water at the surface. This potential depends on the purity of the water and to some extend on the author reporting it. Often the potential of a monolayer is reported as relative to the pure water surface rather than absolute value, but this is again dependent on the author. It is likely that a distortion of this structuring contributes to a monolayer's potential, without being directly attributable to any specific polar groups of the lipid itself.

2.4.5 Line active agents

In the same way as monolayers of surfactant shows two-dimensional analogies to usually three-dimensional phenomena like pressure and surface tension, there is the possibility of a lower dimensional analog to surfactants themselves. Namely line active agents (linactants?). Just as surfactants lower the surface tension of liquids or other interface energies of three-dimensional phases, line active agents would lower the line tension between two phases in a Langmuir monolayer.

The possibility of line active impurities has the potential to greatly affect the phase behavior of a monolayer. Because of the low dimensionality extremely low amounts of agent would be required. Langmuir monolayers already contain very little material. For an order-of-magnitiude estimate: At a thickness of 10nm and a density of 1g/cm^3 a Langmuir layer requires only 10mg of material per square meter. Assuming a line thickness also equal to 10nm it takes only 100ng per kilometer of domain edges. With a characteristic domain size of only 10µm it would take only on the order of 10µg of material per square meter to cover all domain edges, i.e. one per mille of impurity in the layer. Getting a water surface clean enough to measure the pure surface tension takes some work, getting it so clean that line tensions are unaltered is unlikely to be easy.

2.4.6 Morphologies

With lipids like DPPC, which have large headgroups, the headgroups is the limiting factor in how small the MMA can get. At low pressures the ions have large hydration spheres and the tail chains therefore curl up in a disordered liquid in order to fill out the space.

In the coexistence regions where two distinct phases are present very complex morphologies can arise. These are shaped by a competition between short-range attractive forces like the line tension seeking to minimize the interface between the different domains, and the long-range repulsive forces of the dipole moments, which limits the size of individual domains.

McConnell. (McConnell 1989) and Heinig & Fischer. (Heinig & Fischer 2003) have simulated the domain size and shape assuming two fluid phases with a fixed relative area, a certain difference in dipole moment density and a certain line tension, in equilibrium. All such cases with a given area ratio are equivalent except for a scaling. Domain size is determined by the ratio of dipole moment density and line tension (line tension obviously making bigger domains and high dipole moment density smaller). The shape and form of domains are determined by the relative areas of the phases. By the superposition principle (see Figure 12) the absolute value of the dipole moment density will not matter, only the relative difference between the phases. Even if one phase has a dipole moment of zero it will still repel itself since it can be thought of as being domains of the opposite dipole moment density superimposed on a continuous surface which will exert no forces on objects embedded in it.

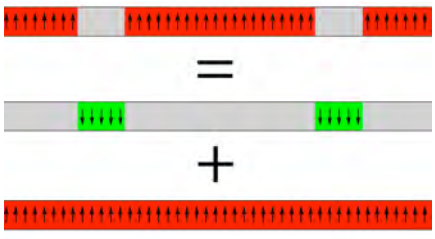

Figure 12. The superposition principle. Holes in a layer of otherwise uniform dipole moment density can be thought of as domains of opposite dipole moment superimposed on a continuous background layer.

The energy to be minimized when analyzing the problem theoretically can therefore be reduced to:

$$E = \oint_{\substack{Phase \\ boundaries}} \lambda ds + \frac{1}{4\pi\varepsilon\varepsilon_0} \int\int \mu(r) v(r-r') \mu(r') \cdot d^2r \cdot d^2r' \qquad \text{Eq. 2.26}$$

Where v is some function proportional to (r-r') for large argument, but leveling of to some finite value at small arguments to keep the integral from diverging. The physical justification for this is that the dipole-dipole energy has no physical meaning for distances less than the size of the individual physical dipoles making up the monolayer. In order for theoretical calculations on systems like this to have any sort of predictive power it is important to use a consistent choice of v. Since the expression is symmetric with respect to the two phases it follows that whichever phase is stable at area fraction Φ the inverted phase will be stable at area fraction 1-Φ.

That domains cannot grow to infinite size can easily be seen by considering the electrostatic energy of an infinite domain boundary. Consider two semi-infinite phases. The field at any given point a distance d into one phase, due to the dipole density of the other, can be calculated by a double integration:

$$\int_d^\infty \int_{-\infty}^\infty \frac{p}{\varepsilon_0} \left(x^2 + y^2\right)^{\frac{-3}{2}} dxdy \qquad \text{Eq. 2.27}$$

where x is the distance along the domain edge and y the distance perpendicular to it. Because $(x^2+r^2)^{1/2}$ is the distance to the point and the field depends on this to the power of minus third. This goes as r^{-2} which make sense. The amount you "see" goes up as r, but its effect drops as R^{-3} leading to the inverse square law. Integrating from r to infinity gives the field at distance r from the edge. The field due to the other phase is thus inversely proportional to the distance to that phase. This breaks down at a distance comparable to the size of the dipoles, as obviously the field does not go to infinity at the boundary. While the field is finite everywhere, the interface energy due to the field is infinite since the field reaches infinitely far into the other phase dropping off only as r^{-1} which integrates to infinity. Thus no matter how high the line tension, there is a domain size at which it is favorable to create more interface.

Since domains of a given phase does not grow to infinite size, even if theoretically allowed to perfectly equilibrate, it is actually somewhat wrong to denote them "phases". Real phases are the various structures formed by the domains. As an analogy a water molecule is not a "phase", given that it has a definite finite size consisting of two hydrogen atoms and an oxygen atom, rather "ice" is a phase, and it made up of many water molecules. However, on the size of individual molecules,

too small for the long-range dipole forces to build op significantly, phases like LE and LC certainly behaves like true phases (in a way that a single water molecule does not). I therefore propose using the words “microphase” and “macrophase” to distinguish between the two cases.

Two general morphologies have been subject of some theoretical analysis: The stripe phase and the hexagonal phase. The hexagonal macrophase is characterized by a hexagonal array of domains of one microphase embedded in the other. The stripe phase is in the perfect incarnation consisting of perfect infinite length straight stripes of alternating microphases, each phase having the same width in each stripe, with the relation between the two widths equal to the relative area. Both of these macrophases is of course likely to show up in real experiments as full of defects and only close to equilibrium. The hexagonal phase is likely to show dislocations in the array, and the stripe phase is likely to have stripes wave and curl over large distances, and occasionally end. To my knowledge these are the only macroscopic phases that has been given serious consideration as equilibrium phases given the circumstances described above. I am unaware of any proof that these would be the only candidates, but it is hard to imagine anything else could compete for minimization of free energy. For domains of finite size it is natural to assume that they would all be of equal size, and hexagonal packing is the natural pacing of objects in the plane. For infinite domains any deviation from straight strips would also seem to lead to higher energies. This is not a definite proof that no other stable morphologies can exist, but intuitively it seems sound.

The free energy per unit area of a stripe phase is calculated to be:

$$F_S = \frac{\mu^2 \phi}{2\pi\varepsilon\varepsilon_0 w}\left\{\frac{4\pi\varepsilon\varepsilon_0\lambda}{\mu^2} - \ln\left[\frac{w}{2\delta}\frac{\sin\pi\phi}{\pi\phi}\right]\right\} \qquad \text{Eq. 2.28}$$

where μ is the difference in dipole density, φ is the area fraction of one microphase, λ is the line tension w is the width of the strips of the same microphase, and δ is the spacing between individual dipoles. Without the δ as a cutoff for very small interaction distances the integrals of the free energy diverges. Minimizing the above equation with respect to w gives:

$$\frac{dF_S}{dw} = -2\frac{\phi\lambda}{w^2} + \frac{\mu^2\phi}{2\pi\varepsilon\varepsilon_0 w^2}\ln\left[\frac{w}{2\delta}\frac{\sin\pi\phi}{\pi\phi}\right] - \frac{\mu^2\phi}{2\pi\varepsilon\varepsilon_0 w^2} = 0 \Leftrightarrow \qquad \text{Eq. 2.29}$$

$$-\phi\lambda + \frac{\mu^2\phi}{4\pi\varepsilon\varepsilon_0}\ln\left[\frac{w}{2\delta}\frac{\sin\pi\phi}{\pi\phi}\right] - \frac{\mu^2\phi}{4\pi\varepsilon\varepsilon_0} = 0 \Leftrightarrow \qquad \text{Eq. 2.30}$$

$$\ln\left[\frac{w}{2\delta}\frac{\sin\pi\phi}{\pi\phi}\right] = \frac{\mu^2 + 4\pi\varepsilon\varepsilon_0\lambda}{\mu^2} = 1 + \frac{4\pi\varepsilon\varepsilon_0\lambda}{\mu^2} \Leftrightarrow \quad \text{Eq. 2.31}$$

$$\frac{w}{2\delta}\frac{\sin\pi\phi}{\pi\phi} = \exp\left(1 + \frac{4\pi\varepsilon\varepsilon_0\lambda}{\mu^2}\right) = e\cdot\exp\left(\frac{4\pi\varepsilon\varepsilon_0\lambda}{\mu^2}\right) \Leftrightarrow \quad \text{Eq. 2.32}$$

$$w = \frac{2e\delta\pi\phi}{\sin\pi\phi}\exp\left(\frac{4\pi\varepsilon\varepsilon_0\lambda}{\mu^2}\right) = \frac{\pi\phi}{\sin\pi\phi}w_0 \quad , \quad w_0 = 2e\delta\exp\left(\frac{4\pi\varepsilon\varepsilon_0\lambda}{\mu^2}\right) \quad \text{Eq. 2.33}$$

w_o is the width one would get for a completely isolated stripe (ϕ equal to 0). The free energy of hexagonal phase cannot be calculated analytically, especially given the complicated shape of equilibrium domains. However, it is relatively simple to integrate over a hexagonal array of circular domains out to a point where sufficient accuracy is obtained. The exact equilibrium shape of the domains is unknown, although it can be numerically simulated to great accuracy. The consensus is that the contribution to energy from domain deformation is negligible at all area fractions.

The calculated energies are remarkably similar across most of the possible area fractions, but they do cross over each other. At low area fractions (isolated domains) circular domains are slightly more favorable than stripes. At an area fraction of 0.286 stripe phase overtakes the hexagonal phase and remains the thermodynamically most stable phase up until 0.714 where inverted hexagonal takes over, as by the symmetry argument noted above. The system is not forced to remain purely one phase or the other, if free energy can be lowered by having the phases coexist, each having a different area fraction of microphases than the overall. Such a system can be constructed by plotting a straight line connecting one point from each curve on the free energy diagram. The most favorable of such systems will be along the cotangents of the curves. The respective areas of the two macrophases will be determined by the lever rule.

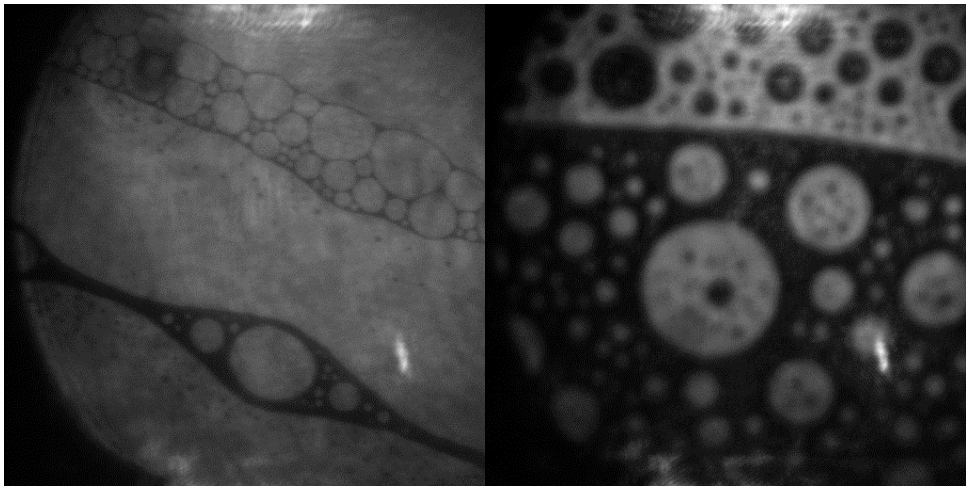

Figure 13: Two examples of far from equilibrium morphologies. The first picture has a strip of inverted foam spanning across a piece of almost pure fluid phase, and another thick strip of gas phase below it. Structures like this are incredibly stable because of the repulsion between like phases. The second picture shows not only a macrophase boundary, but a nested hierarchy of bubbles within drops and drops within bubbles. Fusion of bubbles/drops are rare and equilibration via evaporation/condensation takes a long time. Field of view is 205μm in both pictures. Own data.

2.4.7 Meta-morphologies

Two coexisting macrophases means an the existence of an interface were the symmetry of one phase has to change to the other. This necessarily means an increase in electrostatic energy and linetension energy. In other words the two macrophases will have an interface energy between them, a macro-line-tension. Naively one might think that this does not lead to extra complications as these are real phases and will just separate macroscopically. However, since the two macrophases have different microphase area ratios, they will also have a slightly different dipole moment density. There will therefore come a point when it will be unfavorable for a macrophase to grow any further. All the previous argumentation then holds for these macrophases, this time of course Δ would be something on the order of the domain size. The macrophases would therefore be expected to assume either a meta-stripe phase or a meta-hexagonal phase. Or in the case where their respective areas are right you'd get a coexistence phase. It is easy to extend this argument and argue that by induction a fractal phase should be theoretically possible, as the area fraction of the microphases approach a critical value higher and higher order macrophases will form. A complication is that the macrophases are not fluid and therefore not isotropic, the hexagonal phase has a six-fold rotation symmetry and the stripe phase a two-fold rotation symmetry. This means that the macro-line-tension would depend on direction and would likely change the morphologies of the subsequent higher phases, possibly even prevent them from occurring, but to determine that would take a theoretical work beyond the scope of

this thesis. Of course thermal fluctuations are likely to hide the fractal structure in any real systems given the way such fluctuations grow in 2D systems at nonzero temperatures, and even if they don't the activation energies to reach equilibrium on this scale will be truly monstrous. Therefore real systems are unlikely to ever reach anything resembling this fractal phase for more than one or two levels, but it is an interesting theoretical possibility nonetheless.

2.4.8 Non equilibrium

While the possible morphologies of a perfect equilibrium two-fluid system are limited (although still diverse and interesting compared to the infinite homogenous phases of 3D equilibriums of course), many monolayers will often be far from equilibrium. Since equilibrium entails structures of micron-size and more, there are likely to be very high barriers for transition between structures. High enough that many morphologies are likely to be meta-stable on any reasonable timescale. For example while domain size and shape may equilibrate to uniform size and circular shape over the course of hours, the number of domains might not change as easily. If there are too few domains for strict equilibrium it is likely that the existing ones will grow much larger than they are "supposed to", rather than new ones nucleating and the whole structure displacing to accommodate the new domains. Figure 13 and Figure 14 illustrate some of the strange shapes monolayers can form.

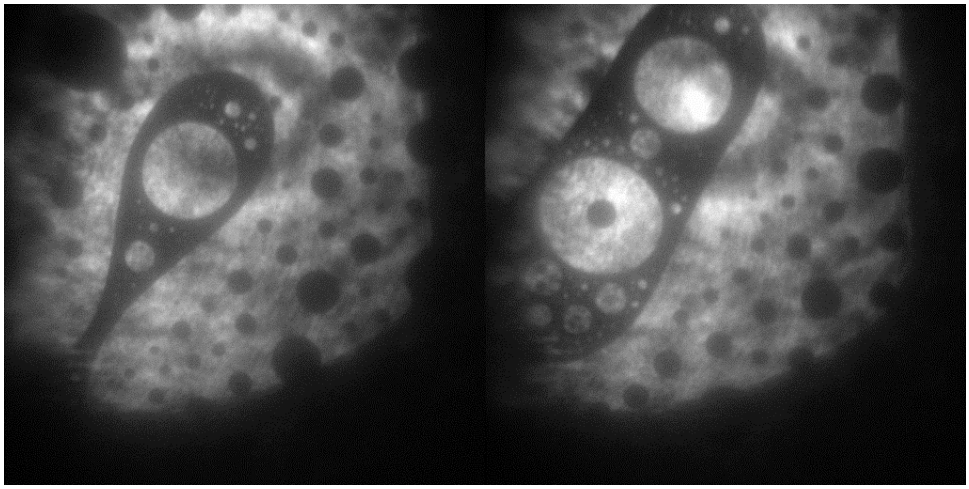

Figure 14: Two consequtive images of a monolayer in the gas-fluid coexistence regime, but far from equilbrium. The images are dominated by a big gas domain containing several smaller fluid domains. The linetension of the domain perimeter works to circularize the domain. Field-of-view is 205μm in each picture. Own data.

If a monolayer is stretched relatively quickly from a continuous liquid expanded phase and into the coexistence regime, then initially the bubbles formed will

arrange into a hexagonal lattice (with defects), a situation that is pretty close to the equilibrium state. As the bubbles grow eventually they start approaching each other enough to deform and begin to take on a hexagonal shape. In the end the liquid phase is reduced to a thin web of lines around polygonal bubbles. In this very rarified state it would be advantageous to form small droplets rather than long lines, but the kinetic barrier is usually too large.

2.5 Effect of voltages on bilayers

The effect of a voltage across a bilayer must be expected to differ a bit from the effect on monolayers. An obvious difference is that the two layers making up a bilayer is oriented opposite to each other. That means an effect on the dipole moment of one layer will tend to have the opposite effect on the other. A large field would favor fluid state in one leaflet and gel state in the other, a state which would have trouble being realized unless lipids are readily able to flip sides to accommodate the resulting discrepancy in mean molecular area.

2.5.1 Electrostriction

Another difference between monolayers and bilayers is that bilayers have a conductive medium on both sides. This means that while an applied field on a monolayer will tend to thicken it in order to replace low dielectric constant air with the higher dielectric constant lipid, the voltage across a bilayer will tend to compress it. Since a membrane is thinner in the fluid state this state will be favored.

The work required to change the capacitance of a capacitor under constant voltage V, by and amount ΔC is:

$$W = -\frac{1}{2}V^2\Delta C \qquad \text{Eq. 2.34}$$

Assuming an area increase of 25% and thickness decrease of 16% when changing phase, a capacitance before the change of 1μF/cm², and a voltage of 100mV, the energy change can be calculated as follows:

$$\Delta C \approx C \cdot \frac{\frac{\Delta A}{A}}{1+\frac{\Delta d}{d}} = C \cdot \frac{0.25}{0.84} \approx 300\frac{nF}{cm^2} \Rightarrow \qquad \text{Eq. 2.35}$$

$$W = \tfrac{1}{2}(100mV)^2 \cdot 300\frac{nF}{cm^2} = 1.5\frac{nJ}{cm^2} \qquad \text{Eq. 2.36}$$

at 30Å^2 of bilayer per molecule this is equivalent to a change of melting enthalpy of

$$\Delta\Delta H_m = 1.5\frac{nJ}{cm^2}\cdot 30\mathring{A}^2\cdot 6.02\cdot 10^{23} mol^{-1} = 2.7\frac{J}{mol} \quad \text{Eq. 2.37}$$

this should be compared to the usual melting enthalpy of lipids which is in the range of 10-40kJ/mol (Mabrey & Sturtevant 1976) so the effect of this enthalpy shift on the transition temperature will be very small.

2.6 Fluorescence.

When a molecule absorbs a photon and enters an exited electronic state, that state will typically be vibrationally exited as well, since the equilibrium position of the nuclei will be different with the different electronic structure. Decay of this vibrational state is typically very rapid and the molecule will therefore lose some energy to the environment before returning to the ground electronic state. Time scale for loss of vibrational energy is typically picoseconds, while emission of fluorescence tend to take nanoseconds. This means that it will emit light at a longer wavelength. This process is called fluorescence. As fluorescence leaves the molecule in the same state as it started the process could in principle repeat indefinitely. However, multiple side reactions can occur. The most common side reaction is called an intersystem crossing. Interaction with the environment allows the molecule to enter a triplet electronic state with lower energy than the exited singlet state. This state is more stable since return to the ground state requires another interaction with the environment to bring the molecule back to a singlet, as direct conversion is quantum mechanically forbidden. The molecule can therefore remain exited usually for microseconds but in some cases for minutes. When it does return, again light is given of at a longer wavelength than the one exiting it. This process is called phosphorescence. Long-lived phosphorescence is known from glow-in-the-dark toys. In studies utilizing fluorescence, phosphorescence is a minor annoyance. Since the molecule is incapable of fluorescing while trapped in the triplet state fluorescent molecules tend to blink when illuminated, rather than giving of continual light. In fluorescence studies blinking is generally undesired. The effect can be reduced by using low intensity of excitation light, as well as making sure the sample contains triplet state molecules to help quickly revert the metastable state. Molecular oxygen is excellent at this. it can therefore be a good idea to make sure that the sample is well aired before an experiment, for example by bubling oxygen gas through it (Widengren et al. 1995). The various transitions are summarized in the traditional Jablonski diagram of Figure 15.

From the Jablonski diagram it is apparent that the emitted light will almost always have a lower energy than the absorbed light. Rare exceptions can happen by statistical flukes, but in general there will be a conversion of some of the energy into heat. This is further reinforced by the fact that excitations to some high

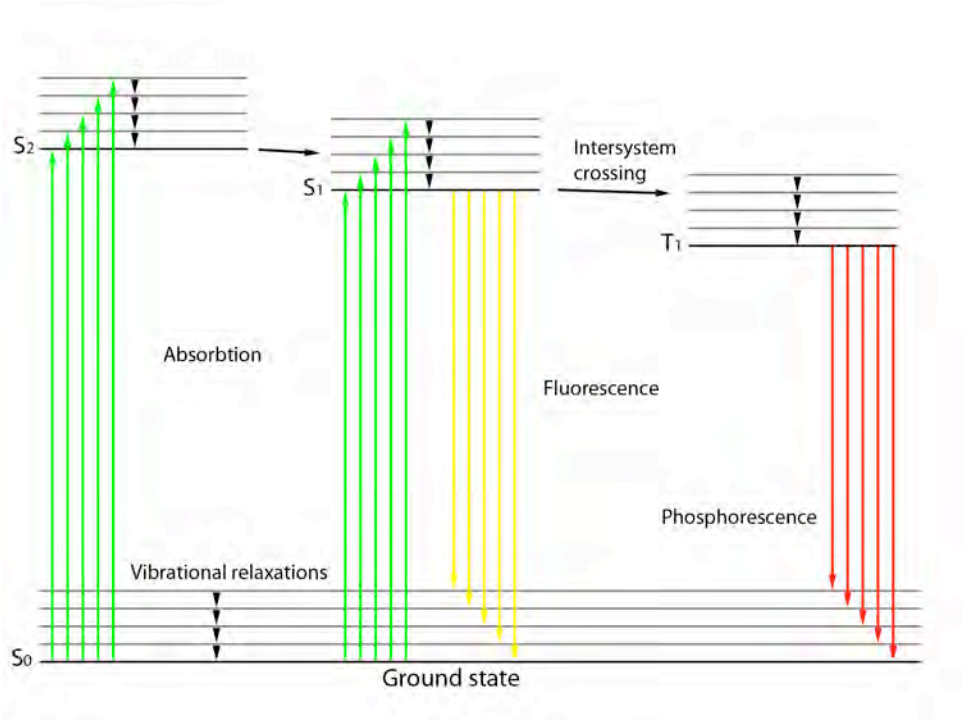

Figure 15: Jablonski diagram describing the process of fluorescence. Processes that change the fluorophores energy are shown as arrows going between horizontal lines representing the various possible states. Green: Abosrption of excitation light. Yellow: Emmision of fluorescence. Small downwards black arrows: Loss of vibrational energy. Horizontal black arrows: Radiationless changes of electronic state.

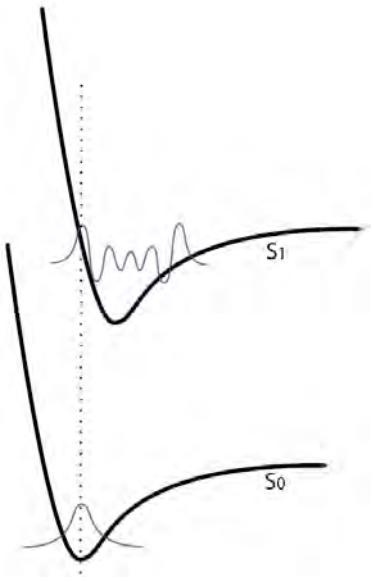

Figure 16: Schematic representation of the optical excitation of a molecule. The black curves represent the inter-nucleus potential defined by the electronic structure. The blue curves are examples of nuclear vibrational states, the bottom one being the ground state. Electronic excitation changes the bond lengths of a molecule. After excitation the molecule is more likely to be found in an exited vibrational state, since this maximizes the overlap of the nuclear wavefunction. The overlap is higher between the two drawn states than it would be between the ground state and the vibrational ground state in S_1 (not drawn). Therefore fluorophores always tend to lose a good amount of energy to vibrations, leading to Stokes shifts being significant.

vibrational states are more likely than exitation to a vibrational ground state (see Figure 16). The distance from the wavelength at which the fluorophore is most likely to be excited to the wavelength of maximal emission is called the Stokes shift.

Also evident from the Jablonski diagram is that the fluorescence will be independent of the light used to excite it. Some light is more likely to be absorbed than other due to a better match of available vibrational states to the energy, but once a photon is absorbed the fluorescence is indistinguishable. With a factor of 1000 difference in timescales vibrational states will be completely thermalized before emission occurs.

Exitation of a fluorophore does not always lead to emission of fluorescence. The relaxation can be non-radiative by losing the energy to heat either directly or by some pathway catalyzed by transfer of the energy to another molecule (quenching). The quantum yield of a fluorophore is defined as the ratio of the number of emitted photons to the number of aboserbed photons. Quantum yield is one of the most important characteristics of a good fluorophore, both because it means a bright fluorescence since much light will be emitted, but also because it correlates heavily with good photostability (see below).

2.6.1 Bleaching

Rarer than phosphorescence, but much worse, is processes that lead to a complete irreversible change to the fluorescent molecule. When this happens the molecule stops fluorescing completely and is lost. This is called bleaching. One of the main important qualities of a good fluorophore is resistance to photobleaching. Resitance to bleaching is known as photostability. Good photostable fluorophores are able to go through on average about a million fluorescence cycles before irreversibly bleaching. Because most bleaching pathways occur via the triplet state, good quantum yield often correlates with good photostability.

Bleaching is undesirable in almost all fluorescent applications because it limits the time at which a particular fluorophore can be used. For applications like microscopic imaging the problem can be somewhat mitigated by using a higher concentration and a lower excitation intensity in order to increase lifetime, but retain fluorescence intensity, although usually the fluorophores are a disturbance of the system studied and the concentration can therefore not be increased forever without additional problems. For studies utilizing single molecules such as single particle tracking, and fluorescence correlation spectroscopy photostability is even more important. As single molecules are studied increasing concentration is no use, and every molecule has to last for the duration of the time it is measured. Hence it is important not only to use fluorophores with good photostability and quantum yield, but also that as much of the emitted light as possible reaches the detector and that the detector is as sensitive as possible.

It is also a well-known fact that lifetime for some reason depends more than linearly on excitation power. That means that you can get more photons from a given fluorophore if the intensity is low. The reason for this is not entirely known, but it presents yet another reason to minimize the intensity used.

Strictly speaking bleaching does have its uses, for example in the technique "fluorescence recovery after photobleaching" (FRAP) which is used to study diffusion. In FRAP part of a sample containing fluorophores is exposed to powerful radiation, bleaching all fluorophores in the given an area (or volume), by subsequently monitoring how the fluorescence recovers as fluorophores diffuse in from the surrounding region information about the diffusive properties of the sample is gained. However a photostable dye is still desirable for good signal to noise ratio, so bleaching is more likely to be achieved by using a higher bleaching intensity than by deliberately using an unstable dye.

2.6.2 Extinction coefficient

Another important characteristic of good fluorophores is a high molar extinction coefficient. That is how efficiently they absorb the excitation light. Extinction coefficients are of course a function of wavelength, what really matters if the value at the wavelength of available excitation light. A high value will mean that a lower intensity of light can be used, therefore reducing problems such as heating of the sample as well as safety issues with intense light. Molar extinction coefficients are expressed in units of inverse length per concentration (how far an average photon will travel into a given solution), or equivalently an area either per mole or per molecule (the interaction cross section, how much space the molecule takes up in the eyes of a photon).

2.6.3 Common fluorophores

Most used fluorophores are conjugated organic molecules. The regular covalent bonds in organic molecules have too high an energy gap to enable fluorescence or any other photochemical effects in the visual wavelengths. Conjugation of double bonds leads to a lower gap between the lowest unoccupied molecular orbital (LUMO) and the highest occupied molecular orbital (HOMO). This is important because although using ultraviolet radiation (matching the energies of unconjugated bonds) would in theory allow greater resolutions to be achieved, ultraviolet optics are notoriously hard to build. Also the fact that many bonds work together in the excitation of a conjugated system means that the excitation is delocalized and only lead to a small reduction in bond strengths. This makes conjugated fluorophores more photostable. Exiting an electron from a single covalent bond with ultraviolet light would reduce that bonds bond order to zero and break it. A third point is specificity. Hard UV would be absorbed by and damage a lot of organic molecules, rather than only the molecules designed for it.

Only alternatives to conjugated organic fluorophores would be transition metal complexes, whose d-orbital electrons often have transitions in the visible regime; or quantum dots, nanoparticles of metal or semiconductor, which due their small size have their usually very small band gap between their delocalized orbitals increased to specific visible energies. Quantum dots are extremely photostable, but their size is orders of magnitude bigger than lipids, which means their use would perturb the system too much.

The fluorophores used in this study are both of the π-conjugated kind. One is rhodamine 6G an old classic used extensively because of its great photocharacteristics and also extremely low price. It is so commonly used that it is pretty much the reference fluorophore for fluorescence studies. It absorbs the preferentially in the green area of the spectrum and exhibits a very small Stokes shift. Most of the emission lies above 600nm. The other fluorophore used is a newer commercially designed fluorophore of the Alexa series, Alexa 633. The Alexa dyes are named by their peak absorption, Alexa 633 thus absorbs in the red part of the spectrum, around 633nm. The emission is deep red to near infrared.

2.7 Lasers

Excitation in this work is done by laser light. Although the details of laser operation are hardly relevant for the present work, a short description is in its place. Although now a word adopted into language, laser is an acronym for “light amplification by stimulated emission of radiation”. Lasers utilize a population inversion to amplify light. A photon interacting with a molecule in an exited state is as likely to cause molecule to return to the lower energy state, as a photon interacting with a molecule in the lower energy state is to excite it. Returning to the lower state by stimulation in this way increases the number of photons in the mode in question by one. At conditions close to thermal equilibrium at room temperature states corresponding to visual photons will be very close to empty so only absorption is usually considered. If a population of atoms in which a higher energy state is more populated than a lower energy state is produced, then light corresponding to the energy gap between these two states will stimulate emission more often than it will be absorbed, thereby amplifying the light. Setting up a resonant cavity between two mirrors will greatly amplify the modes of light, which resonates with the cavity. In the best quality lasers this is only a single mode. The amplified single mode light is allowed to gradually leak out by having one of the mirrors be less than hundred percent reflective. The emerging beam will appear to all originate from a single point. This provides light with exceptional spatial and temporal coherence. Because the light behaves like a point source it can be focused very precisely, a definite requirement for the FCS technique (Kelsal 2005).

2.8 Microscope theory

2.8.1 Diffraction

Even light emitted from a point source cannot be focused perfectly into a point on a detector because the light has a finite wavelength. Instead it will, under perfect conditions, form a so-called airy disc with a diameter determined by the wavelength of the light and the properties of the lenses used (see next chapter). The resolution of an optical microscope is generally defined by the Rayleigh criterion, introduced by lord Rayleigh: The airy disc is a circular symmetric function of two variables with a central maximum dropping of to a ring of zero value followed by an infinity of alternating rings of zeros and increasingly low maxima. The Rayleigh defines the resolution of an optical imaging system as the distance from the maximum to the first zero of the airy discs formed.

2.8.2 Objective

The most important part of any optical microscope is the lens or set of lenses initially gathering light from the object being observed, these are called the objective. Objectives performances are foremost characterized by two parameters, the numerical aperture and the magnification.

Numerical aperture

The main parameter describing the performance of an objective is the numerical aperture. The numerical aperture (NA) is defined as

$$NA = n\sin(\theta) \qquad \text{Eq. 2.38}$$

Where n is the refractive index of the immersion fluid and theta is the half angle of the maximal cone of light that can enter the objective. High numerical apertures are desired because resolution depends on the NA (see chapter 2.8.1). A wide incident angle is also desired because it means a larger percentage of the light emitted from the focus enters the objective, as the cone it samples covers a larger part of the unit sphere. A wide angle also means a shallower depth of field, in other words objects viewed through the objective will get blurry quicker as they move towards or away from the objective. In FCS this is an advantage as the desire is to have as small a focal point as possible (see chapter 2.9), when doing microscopy it means that the z-position has to be controlled more accurately for the picture to be sharp.

High NA means that the angle of the cone of light entering the objective has to be high, as shown on Figure 17 that means that the focal length is small compared to the lens aperture. Since the light path can only begin to be bend after it enters the

objective actual physical width of high-NA objectives tend to be much bigger than the width of its “eye opening”. Hence high-NA objectives tend to have very short working distances when compared to their physical dimensions and to objectives of lower NA.

The two objectives usually used for this work is a NA=1.2 water immersion objective with a working distance of 250µm, and a NA=0.6 air objective with a working distance of 2500µm.

Magnification

For optimal performance, the magnification of an objective should be chosen to fit with the detector used to view the sample. If a low magnification (under-sampling) is used then the resolution of the resulting image will depend on the pixel size of the detector (whether pixels on a CCD chip, or cells in the retina), rather than the diffraction limit. This is of course fine if a rather large field of view is more important than absolute maximal resolution. If the magnification is too large (over-sampling) then the resolution is limited by diffraction and the microscope fails to make full use of the detector. Contrast will drop as the received photons from a minimally resolved area are spread across multiple pixels. This could to some extend be remedied by binning pixels together, but it counteracts the point of having many pixels to begin with and the field of view suffers. According to the sampling theorem, optimal digital sampling is achieved when sampling 2 points per resolution size.

The magnification of a microscope depends on the ratio of the focal length of the objective and the condenser. Objective magnifications are calculated based on a standard focal length of 180mm. This microscope is build as an infinity-corrected microscope, meaning that the objective focuses the image at infinity, and a subsequent lens (the condenser) focuses the image back down on the detector. If the condenser has a focus length different from the standard then it is said to have a magnification as well. The total microscope magnification is the two

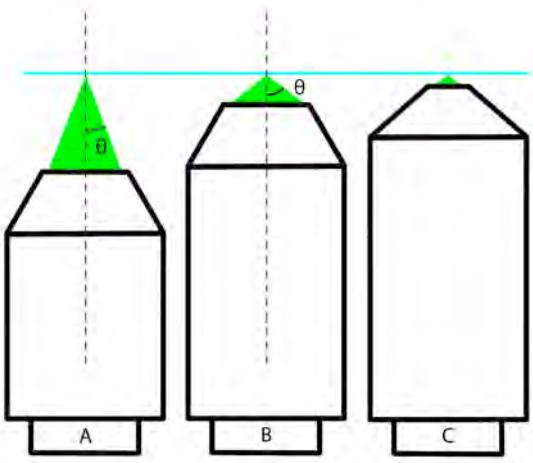

Figure 17. Schematic drawing of microscope objectives, the blue line represents the focal plane, the green triangles show the cone of light picked up by the respective objectives or alternatively the light coming out from the objective when a collimated laser beam enters from below. Objective A has a small half angle, **θ**, of light picked up (low NA), and therefore a larger working distance than B which otherwise have the same dimensions. C is a more likely representation of a high NA objective, since their light opening tends to be smaller the working distance is reduced even further.

magnifications multiplied together.

The advantage of an infinity microscope is that all image cleanup filters can be put in the infinity zone. Here every part of the image is spread out over a vide area meaning that a scratch or dust on the filters will affect all parts of the image equally. Additionally the light rays forming the image is all parallel in this domain, this means that any additional refraction will not change the focus when put there.

2.9 Flourescence Corelation Spectroscopy

Fluorescence Correlation Spectroscopy (FCS) is a powerful technique for determining the diffusive behaviour of of a sample. It uses the confocal method to record time trace of the fluorescence intensity of a small sample volume. It was first realized experimentally in 1974 by Douglas Magde who used it for the measurement of translational diffusion coefficients (Magde et al. 1974).

The sample volume is probed by a laser which is focused into a diffraction-limited spot through an objective. Fluorescent light is sampled through the same objective, separated from the laser by a dichroic mirror and focused through a pinhole to remove light not originating from the focal point. This is called confocal illumination – the illumination is concentrated at the exact same spot as the sampling. The remaining fluorescent light is then recorded by an avalanche photodiode.

By blocking out-of-focus signal twice (once for illumination and once for sampling) the result is that the recorded intensity depends only on the flurophore concentration in a very limited space. Had the pinhole not been there then the out of focus signal would still integrate to much more than the signal from the focal point, although the illumination intensity is lower out of focus, since the volume is correspondingly larger (green area in Figure 18).

Same thing is the case if a pinhole is used but with uniform illumination. The heavy restriction of the focal volume is important to maximize the fluctuations, which forms the basis of the FCS technique (see below).

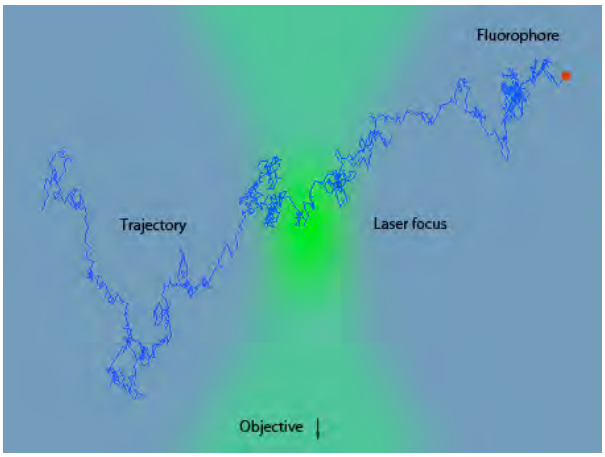

Figure 18: Illustration of the laser focus. Fluorophores diffuse in a random walk, and light up when crossing the diffraction limited focus point of maximal intensity.

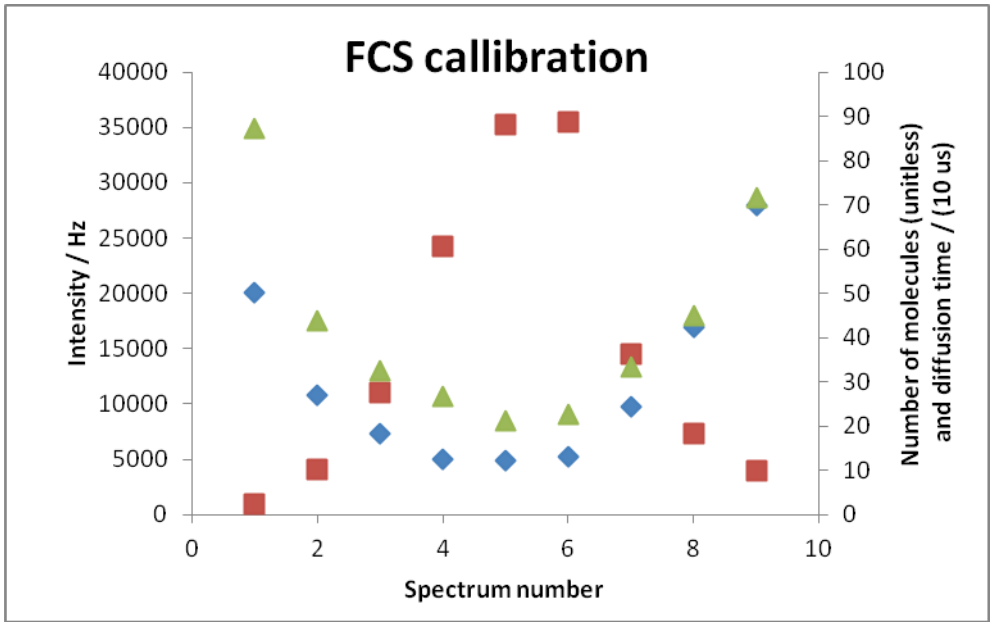

Figure 19: Finding the optimal focus on the water surface for FCS by making multiple consecutive measurements while the water slowly evaporates. Diffusion times (green triangles) decreases to a minimum along with the average number of molecules in focus (blue diamonds) while the intensity received per molecule increases to a maximum (red squares).

Using both pinhole and focused illumination the out of focus signal is properly suppressed. A focal volume will never be a hard well-defined volume, rather it is characterized by a response function. A fluorophore at a given point in space will lead to a certain average intensity recorded, which defines the response function for this point in space. Generally the response function is approximated at an ellipsoid with a Gaussian fall-off away from the center. The validity of this approximation is contested (Rigler et al. 1993, Hess & Webb 2002, Blom 2003) but becomes more accurate the smaller pinhole is used (Hess & Webb 2002, Kastrup et al. 2005).

The recorded intensity time trace is used to calculate the time auto-correlation function G(t), that is the degree of self-similarity between the result at time t and the result at time t+τ.

$$G(\tau) \equiv \int \frac{I(t) \cdot I(t+\tau)}{\langle I^2 \rangle} dt \qquad \text{Eq. 2.39}$$

Since the focus point is small there will be a very limited amount of fluorophores present in the focus at any given time, and the number will therefore fluctuate stochastically as the fluorophores diffuse in and out. At small τ the intensity will be essentially unchanged and the self-similarity is therefore high, at big τ there will be

no correlation between the number of fluorophores present at the two times and the self similarity is low. The characteristic diffusion time is defined as the full width at half maximum of the correlation function.

If the fluorophore concentration in the sample is low then the amount of fluorophores in the sample volume at any one time will exhibit a stochastic distribution. Some times the fluorescensce intensity will be above average and sometimes below. At short timescales the intensity will correlate well with itself since few fluorophores have had time to move. At long timescales it will be completely uncorrelated. In between there will be a drop-off dependent on the diffusion of the sample molecule.

For homogenous diffusion in three dimensions the exact theoretical shape of the autocorrelation function can be determined if the Gaussian approximation is valid (Aragón & Pecora 1976):

$$G_G^{3D}(\tau) = 1 + \frac{1}{\langle N \rangle}\left(1 + \frac{\tau}{\tau_D}\right)^{-1}\left(1 + \frac{r_0^2 \cdot \tau}{z_0^2 \cdot \tau_D}\right)^{-1/2} \qquad \text{Eq. 2.40}$$

where <N> is the mean number of molecules in the focus, τ_D is the diffusion time through the observation volume and r_0 and z_0 are the dimensions of the observation volume in the x,y plane and the z direction , respectively, at which the response intensity is reduced by a factor of e^{-2}.

In monolayers, since the fluorophores are restricted to the water surface, the focal volume has to cross the surface of the water when doing FCS studies on them. If the point of maximal laser intensity does not coincide with the surface, then the fluorphores will experience a broader but less intense spot of excitation. This will lead to a smaller recorded per-molecule intensity, more molecules on average, and a slower diffusion time. By allowing the subphase to slowly evaporate the surface will move relative to the focus in a much more steady way than can be done by the micrometer screws. Recording a correlation spectrum at regular intervals, and then determining the extrema of previously noted parameters allows determination of the point when the focus is optimal.

If the fluorophores used are insoluble the measurement can in theory be done without the pinhole, since all fluorescent signal would come from the surface anyway so there would be no need to remove out of focus signal.

In practice the entire time trace is rarely obtained, saved and then analyzed later. The shortest timesteps are usually sub-microsecond, and in order to get a good signal to noise ratio recording is often kept up for many seconds, leading to prohibitively large data sizes and rates. Rather the short-term correlation is

calculated by specialized hardware, then the data is binned together and kept like that for calculating of the middle-term correlation and so on.

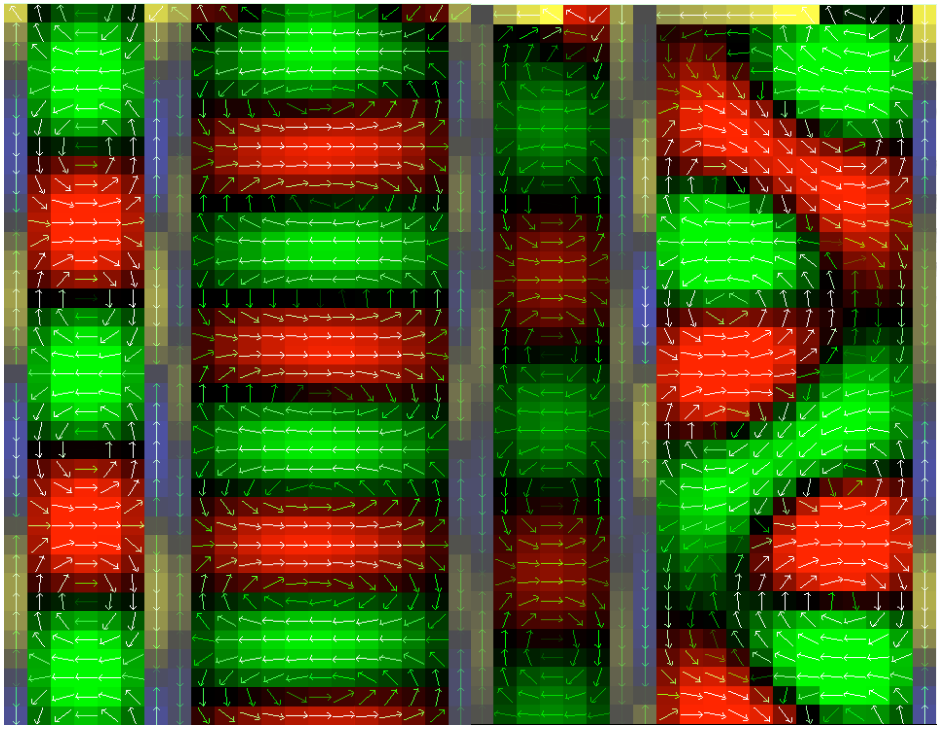

Figure 20: Screenshot from a simulation of electromagnetic radiation in 2D. Green represents electric field out of the plane, red into the plane, arrows show magnetic fields. The picture shows two waveguides hit by a plane wave. In A the wave enters perfectly and the wave travels down as a single mode. In B 60% of the opening is blocked, in the narrow guide this merely leads to a lower intensity in the single mode propagatable at this frequency, in the broad guide it leads to exitation of multiple modes, and a complicated pattern of fields. Simulation done on an applet programmed by Paul Falstad, used with permission.

2.9.1 Single mode fiber

An optical fiber guides light by having a core with a higher refractive index than the surrounding glass. Because the phase velocity is higher in the outside layer electromagnetic waves with a wave vector sufficiently parallel to the fiber gets confined. This is most easily understood as total internal reflection of photons bouncing back and forth down the fiber. This picture is not entirely correct, however, since most optical fiber cores have a diameter comparable to the propagated lights wavelength. The wavenumber perpendicular to the fiber axis will be quantized, and if the core is sufficiently small only one mode of light will be propagated. The second mode will be angled enough to exit the regime of total

internal reflection and will therefore leak out. As shown in Figure 20 this means one can avoid interference by light that is not suitably aligned by sending it trough a single mode fiber.

2.10 Nerve theories

Electricity has been associated with nerves ever since Galvani observed frog's legs twitching when subjected to an electric impulse back in 1791 (Galvani 1791).

2.10.1 Hodgkin-Huxley model

In 1952 Hodgkin and Huxley proposed a mathematical model for how the action potential of nerves work (Hodgkin and Huxley 1952). It was originally just meant as a simple example of how the action potential might come about, but it has since gained wide recognition and is established as the textbook model of how nerves work.

The basis of the Hodgkin-Huxley model is that the cytosol of nerves (and indeed most cells) contains a much higher concentration of potassium kations than the surrounding medium, and conversely the surrounding medium contains much more sodium. This means that the depolarization of the membrane observed in the action potential could be due to an influx of sodium ions and the subsequent re- and hyper polarization could be caused by an outflux of potassium, both ions moving along their concentration gradient.

This Hodgkin and Huxley proposed could be explained by a series of voltage gated protein ion channels in the membrane. In particular it was proposed that the potassium channel has four independent equivalent gates which open and close with voltage dependent rates. The variable n(t) was used to describe the probability of any one gate being open at time t. Since there are four gates in series the probability of a given channel being open is therefore equal to n^4. Correspondingly the sodium channels supposedly have four gates, of which only three are equivalent and described by the parameter m(t) while the fourth is described by it own parameter h(t), the probability of this channel being open is thus m^3h. These three parameters are in turn governed by the gates' opening and closing rates, which are voltage dependent:

$$\frac{dn}{dt} = \alpha(1-n) - \beta n \qquad \text{Eq. 2.41}$$

where α and β are the opening an closing rates respectively. α and β are then functions of the transmembrane voltage, similar equations govern m and h.

By making the rates of m about an order of magnitude faster than those of n and h, and choosing parameters so that m tends to open with decreasing voltage while n and h tends to close then they could produce the effect that a depolarization of the membrane will cause a run-away influx of sodium ions. In a longer time frame the depolarization would kill the sodium current again due to the slow closing of the h gates, at the same time a potassium current would pick up and bring the voltage across the membrane back.

At this point both kinds of channels would closed due to low n and h. The membrane is unable to enter another action potential as long as h remains low. As h slowly increased this is counteracted by the rapidly falling m, thereby keeping the nerve from firing another action potential until stimulated again. The localized depolarization in turn reduces the potential at nearby areas inducing them to fire as well, the end result being a wave like motion across a cell.

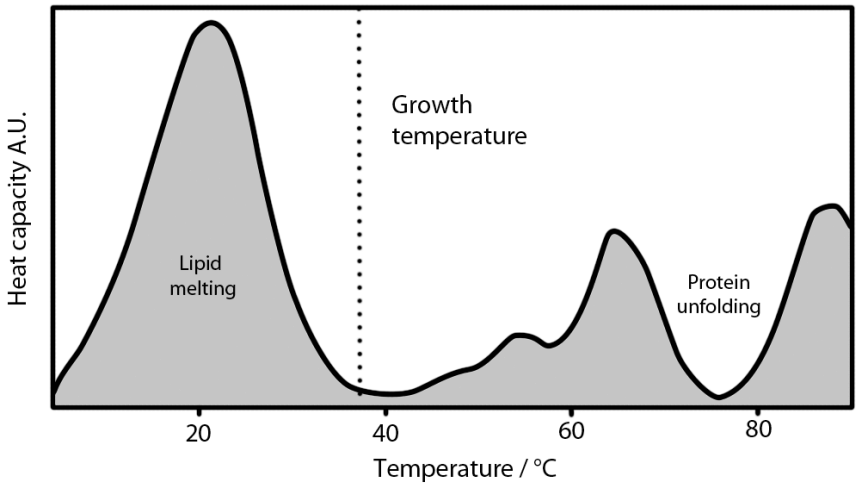

Figure 21: Calorimetric scan of intact E. Coli bacterial membrane grown at 37°C. The peak below the growth temperature is the melting transition of the lipids, the peaks at higher temperature is due to protein denaturation. Figure adapted from Heimburg & Jackson 2007b.

2.11 The Soliton model

The basis of the soliton model - also known as the Heimburg-Jackson model after it proposers Thomas Heimburg and Andrew Jackson – is the simple one-dimensional wave equation. A nerve is modeled as a long and narrow cylinder, when the length is much greater than the width sound propagation along the cylinder can be viewed

as a simple one-dimensional wave, in the absence of dispersion this would be governed by the simple wave equation:

$$\frac{\partial^2}{\partial t^2}\rho^A = c^2 \frac{\partial^2}{\partial x^2}\rho^A \qquad \text{Eq. 2.42}$$

where ρ^A is the lateral density as a function of time t, and place x, and c is the speed of sound in the membrane medium.

As earlier described when the area compressibility of a membrane varies greatly close to a phase transition, this will make sound velocity a function of density:

$$c^2 = \frac{1}{\kappa^A(\rho^A)\cdot \rho^A} \qquad \text{Eq. 2.43}$$

where the area compressibility κ^A is a function of ρ^A, when combined with a dispersive term, for example $-h\partial^4\rho^A/\partial x^4$, where h is a constant determining the strength of the dispersion, then will allow for the existence of soliton solutions. Putting all the above together and changing to a moving coordinate system, z=x-vt, yields the following expression which can be solved analytically:

$$v^2 \frac{\partial^2}{\partial z^2}\rho^A = \frac{\partial}{\partial z}\left(\frac{1}{\kappa_S^A \cdot \rho^A}\left(\frac{\partial}{\partial z}\rho^A\right)\right) - h\frac{\partial^4}{\partial z^4}\rho^A \qquad \text{Eq. 2.44}$$

The solutions to this equation matches pretty well with experimentally determined data from real nerves (Heimburg & Jackson 2005b). Lautrup et al showed that the solutions are stable with respect to small perturbations. This means that these solitary waves might survive in real nerves. Moreover they can be started by arbitrary localized perturbations, even if these are not solitons (Lautrup et al. 2005).

3 Materials and methods

3.1 Description of microscope

3.1.1 Previously existing equipment

The equipment used in the majority of this work is a custom-build combined FCS and wide field microscope. It was originally constructed as an FSC instrument by former phd-student A. Hac, including a 5mW 532nm green laser running in TEM_{00} mode, attenuation filters dichroic mirror cleanup filters from AHF, two avalanche photo diodes, and a real time hardware correlator box. The details of this can be read in her phd thesis (Hac 2003) Later this setup was rebuild by Martin Gudmand to be capable of both FCS studies and microscopy. For this purpose Gudmand added a 200mW 532nm green Torus laser and an Andor EMCCD camera as described in his phd thesis (Gudmand 2008).

3.1.2 Building of the two-colour FCS

In order to upgrade the existing FCS setup to accommodate two-colour cross correlation, a red 5mW 635nm laser, several filters a dichroic mirror as well as a custom build fiber optics combiner was added. The old 532nm FCS laser and the new 635nm were coupled into single mode fibers from free space beams through six-axis aligners and a collimator lens. The light was then combined into a single fiber by a specially produced fiber combiner from MV Photonics, USA. The co-propagating beams were then coupled back into free space, expanded and collimated. The coupling into a single mode fiber ensures the best possible overlap of the two beams. Any misaligned component of light will simply not enter the core of the single mode fiber and will therefore not be propagated to interfere and distort the focal point. This way the only difference in the focal volumes size and position will be that arising from dichromatisms in the fiber and lenses.

This was used to ensure a near perfect overlap of the two lasers. Any component of light entering the fiber, not matching the propagation mode is going to be lost, and therefore won't interfere with the remaining light. The overlap is not perfect because the two lasers have different wavelengths. They will have slightly different divergence angles when exiting the fiber, and the subsequent lenses have slight achromatisms. However it gives a much more reliable result than trying to overlap the lasers with dicroic mirrors in free air would.

A drawback of the fiber solution is the loss of laser intensity. Optimal alignment of the lasers and fiber ends should allow most of the light to enter the fiber, but this is

very hard to achieve. Fortunately FCS does not require a very high excitation intensity owing to the small sample volume. Before the instrument was rebuild for using two colors an attenuation filter of OD3 or even OD3.6 was typically used in front of the 5mV green laser.

The setup originally had two avalanche photo diodes with a beamsplitter in between, so that the signal from the two could be cross-correlated. This gave a better resolution in the nanosecond time scale, but cost half of the intensity, reducing the signal to noise ratio. Martin Gudmand therefore removed the beamsplitter and used only one of the APDs. In upgrading to two-colour FCS a dichroic mirror (cutoff 640nm) was put in instead of the beamsplitter, to separate the emission from the two fluorophores. A new cleanup filter was added in front of each APD (band pass 663nm-738nm and 541nm-623nm, respectively. AHF, Germany), and the entire light path after the pinhole was protected from stray light by metal tubes.

3.1.3 Magnification

In a microscope with eyepieces the magnification is simply the size of the image at which one is looking. The image projected in the eyepiece really has those physical dimension. A digital microscope is ill defined by a magnification factor since a digital image can be reproduced in any size. Rather the pixel size, resolution and field of view are important. Instead of being projected in free air to be viewed through an eyepiece the picture is projected onto the CCD chip of the camera. In the camera used the CCD chip has a pixel size of 16 micrometer. In front of it there is a choise of lenses with magnification 2.5x or 1x. By using an objective with magnification 60x the total magnification becomes 150x. This means that the width of sample being projected onto each pixel is

$$\frac{16 image \mu m / pixel}{150 image / object} = 107 object nm / pixel \qquad \text{Eq. 3.1}$$

in other words: A slight oversampling. Since the chip has 512 by 512 pixels the field of view becomes

$$107 nm / pixel \cdot 512 pixels = 55 \mu m \qquad \text{Eq. 3.2}$$

Two other objectives were often used. A 40x air immersion objective with a working distance of 2.5 milimeters were used when not attempting to do single molecule detection. For big overview pictures occasionally a 10x air immersion objective was used. The possible magnifications are summed up in Table 1.

	60x water imersion	40x air immersion	10x air immersion
1x condenser	267nm/px 137µm FOV	400nm/px 205µm FOV	1.6µm/px 819µm FOV
2.5x condenser	107nm/px 55µm FOV	160nm/px 82µm FOV	640nm/px 328µm FOV

Table 1: Overview of possible pixel sizes and field-of-view sizes possible in the wide field fluorescent microscope used.

3.2 Monolayer trough for single molecule studies

As was described in detail in his PhD-thesis, former PhD student Martin Gudmand upgraded the preexisting FCS apparatus, into a combined microscope and fluorescence correlation spectrometer capable of doing single molecule studies on lipid monolayers. Since getting single molecule resolution requires a high numerical aperture objective, and such objectives require a working fluid the microscope had to be made of the inverted kind.

High numerical aperture objectives have a short working distance. The one used in the setup, a 60x Olympus water immersion objective with a numerical aperture of 1.2, has a working distance of 0.25mm. In this quarter millimeter has to be the immersion water between the objective and the coverglass, the coverglass itself, plus the entire depth of water beneath the monolayer studied.

It is obvious that doing monolayer studies on a trough with only 100µm of water in it is not practical. Instead of this a trough with a hole in the bottom is used, into which a metal coverglass holder can be inserted. This creates a raised “window” in the bottom of the trough. The water level can therefore be extremely low in a limited area above the microscope objective and allow it to get close to the surface, while still retaining a few millimeters of water in the majority of the trough. Of course the water level needs to be adjusted very precisely in order to get it to only just barely cover the glass, but not run off. To achieve this precision in water level in the trough takes some skill, as will be described below.

3.3 Cleaning of trough and coverglass.

Before every monolayer experiment the trough and barriers was rinsed thoroughly with ethanol and then water. It was then blown dry by a stream of nitrogen and immediately placed under a hood to protect from dust. For experiments with air objective the same was done for the coverglass and metal holder. For experiments with the water objective, coverglass and holder was placed in a deconex® detergent

solution and sonicated for several minutes, it was then rinsed with ethanol and replaced in the sonicator under ethanol for several minutes, then finally the same was done with water. Thorough cleaning of the glass ensures that the bare hydrophilic surface is exposed, minimizing the risk of dewetting when the water layer covering the glass is thin.

In intervals of a few weeks trough and barriers were also soaked in dilute deconex® over night and then rubbed exhaustively with ethanol to remove residual detergent, finally it was rinsed with water and dried as usual.

3.4 Cleaning of water surface for monolayer experiments

The trough was filled to the brim with ultrapure water. Then suction was applied to a pipette tip, which was used to siphon up the surface water along with possible impurities. Special care was taken to vacuum along the edges of the trough since the Cheerios Effect makes impurities tend to gather here (Stamou & Dushl 2000). As a test of the cleanness of the surface the pressure sensor was zeroed and the barriers moved in. If the pressure rose no more than 0.1mN/m when moving the barriers from their one extreme position to the other, the trough was deemed clean.

When using the water objective the water level needs to be adjusted very accurately. A trick to help with this adjustment was discovered: When the layer of water over the coverglass gets thin it takes considerable time to run off when water is siphoned out in the side of the trough. This can be used to see when the water level gets close to the coverglass, by watching for a reflection in the surface of the water right above the coverglass while slowly siphoning water. When the reflection gets visibly distorted, it is a sign that the water level is higher above the glass because the friction in the thin layer delaying runoff (Figure 22). This happens when the thickness is close to the desired 100 µm.

Figure 22. Visually assessing the level of water above the coverglass. Water drains slowly from the thin layer above the glass (arrows) this distorts the water surface. The thinner the layer and the faster the trough is drained the bigger the distortion. Experience with the specific trough and siphon allows a rather accurate and fast assessment. Dimensions of drawing are not to scale.

3.5 Procedure for preparation of stripe patterns of DPPC on mica

Solutions were prepared by dissolving ~0.8mg/ml of DPPC in a mixture of 90% hexane and 10% absolute ethanol. The solutions were sonicated for a few minutes to ensure complete dissolution.

A ~50mm^2 piece of mica were cleaved and immediately after a 10µl drop of DPPC solution were applied, rapidly as one drop, and allowed to evaporate without running off the edge of the mica.

AFM images were recorded using silicon VistaProbes™ for non-contact mode and high frequency from NanoScience Instruments, with the following charactaristics:

Spring constant 40 N/m
Resonant frequency 300 kHz
Length 125 µm Width 40 µm
Tip height 14 µm radius < 10 nm

The images were recorded in contact mode in air, which is possible even though the probes were designed for tapping mode.

4 Morphology of monolayers

4.1.1 Onset of gas phase

Part of the PhD work of Martin Gudmand, was a study of the phase behaviour of DPPC monolayers at large mean molecular areas. It was found that when a monolayer is slowly expanded from the LE phase, “holes” are created in the monolayer. Because of the resemblance to a boiling liquid these were named “bubbles”[2]. As part of his thesis Gudmand presented a virial expansion from the area-pressure relationship in the LE phase in order to establish the point at which the monolayer would exit the coexistence and become entirely gas phase. However the accuracy of the fit was questionable, given the far extrapolation from datapoints within a narrow range. It would have benefitted greatly from datapoints in the Gas-LE coexistence phase. However the pressure in the coexistence phase was below the resolution of the pressure balance. In order to improve upon Gudmands work it was attempted to find the relation between expansion speed and MMA of first appearance of bubbles. Certain speeds might facilitate a “super heating” (rather super expansion) of the monolayer, allowing it to remain in pure LE phase, when, by equilibrium thermodynamics, it should enter the coexistence region.

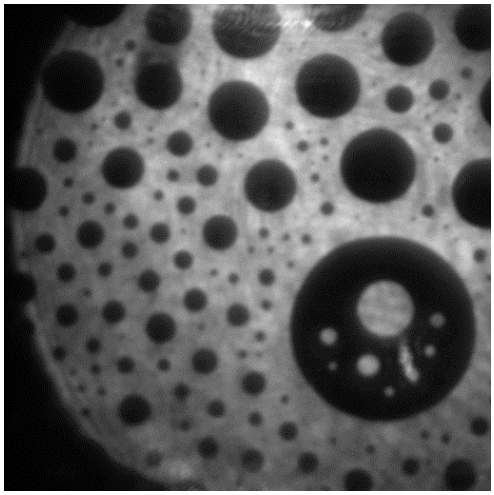

Figure 23: An example of the “bubble phase”, the gas-fluid coexistence regime as it appears in the wide field microscope. The gas phase shows as dark. Field of view is 205µm.

Several experiments were therefore performed. Monolayers were prepared in the LE phase and then slowly expanded while closely monitoring the appearance in the fluorescent microscope. The first time a gas phase domain was observed, the exact mean molecular area was recorded, along with the expansion speed used in that experiment. The results are summed up in Figure 24.

[2] Apparently it was thought that this was a new discovery and therefore quite basic phenomenology was investigated, a process I continued until my own literature search revealed that there is nothing new about the gas-phase bubbles.

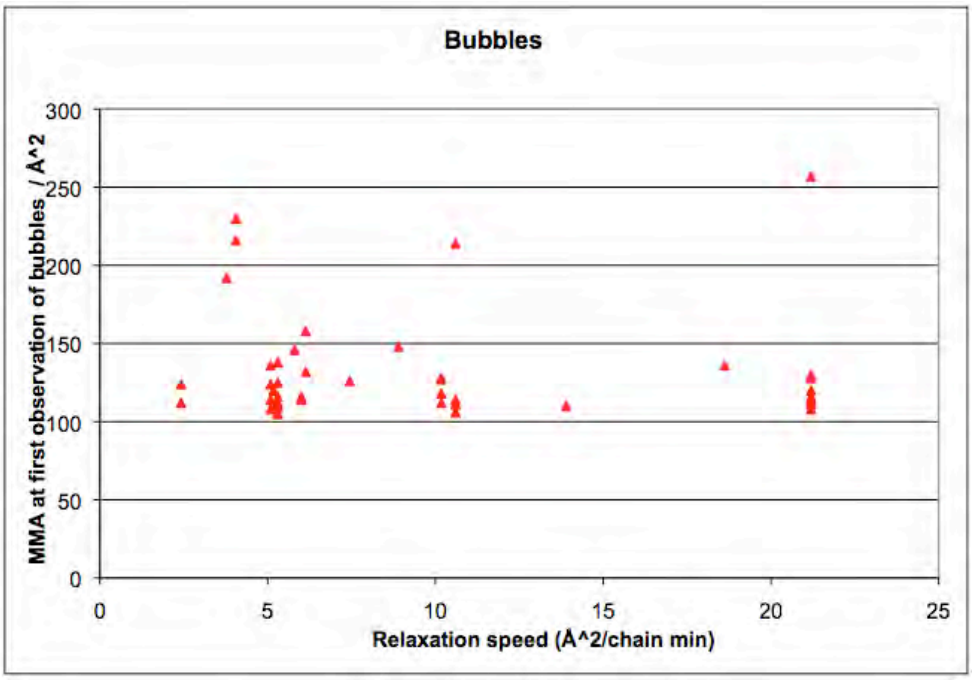

Figure 24: Plot of mean molecular area at first observation of gas phase as a function of the relaxation speed in that experiment. No correlation is evident.

No correlation between expansion speed and mean molecular area was found. However, several interesting observations were made. Across many experiments the mean molecular area of first appearance of bubbles varied widely, but when the same monolayer was compressed and then expanded again, the area of first appearance tended to remain mostly the same. By translating the monolayer across the objective it was found that the monolayer is highly inhomogeneous on the millimeter length scale in this phase. So some areas might show bubbles while others remain in the LE phase. Strangely the patterns seemed to be somewhat reproducible upon compression (even to pressures of 15mN/m, where most of the layer has entered the LC phase) and re-expansion of the same monolayer. It is hypothesized that the monolayer in this phase is highly sensitive to impurities and that an inhomogeneous distribution of impurities from the air is responsible for facilitating the production of bubbles.

It seems amazing that the areas that appear dark in the microscope at high mean molecular areas supposedly almost void of lipids, are able to support the complex morphologies one observes in the gas-fluid coexistence regime. The line tension between the phases is significant as will be shown later

The edge between light and dark phase shows a significant line tension, as can be seen when to parts of the same phase recombine. Big blobs of surface can be drawn

across the surface at speeds of tens to hundreds of microns per second. Yet the dark phase, supposedly almost void of lipids, appears to exert a significant pressure against this tension. One might wonder whether the “gas phase” is really a two dimensional gas, or rather a more expanded liquid phase in which the fluorophores happen not to participate.

The number of molecules in a gas domain can be estimated by using Gudmands figure 0f MMA≈13000Å^2 for the mean molecular area of pure gas phase (Gudmand 2008). For a circular domain of 20µm radius one calculate the number of gas molecules as:

$$n = \frac{A}{MMA} = \frac{\pi \cdot (20\mu m)^2}{13000 Å^2} \approx 10^7 \qquad \text{Eq. 4.1}$$

Where A is the area of the domain in question. So even though gas phase has a large mean molecular area there are still a lot of molecules present.

A line tension the of 1pN would give an overpressure inside of only 50nN/m inside such a domain. This is an extremely low pressure difference. If the inside of such a domain is really an ideal two-dimensional gas, then this pressure difference corresponds to an extra

$$\Delta n = \frac{\Delta \Pi \cdot A}{k_B T} \approx 10^4 \qquad \text{Eq. 4.2}$$

molecules inside the domain due to the overpressure. This number, while still large, is only one thousandth of the total number of molecules in the domain, this helps explain why it takes so long time for domains to equilibrate in size trough two dimensional condensation and evaporation: About 999 in 1000 molecules getting absorbed or lost from a domain edge is going to be cancelled by one going the other way.

4.1.2 Tracking of diffusing domains.

Small LE droplets diffuse with visible Brownian motion as seen in the microscope (Figure 25 shows a snapshot). In order to quantify this they were tracked and the trajectories analyzed applying the techniques of single particle tracking commonly used to probe the diffusion of proteins. For this purpose a matlab script was written to automatically track domains, this script is shown in appendix A. The location of a droplet was specified by hand and then the script followed the particle in subsequent frames by searching for the local center of intensity. Occasionally if two particles made a close approach to each other the tracking could switch from one to

the other. Therefore the tracking was monitored in real time and was interrupted if such a switch happened.

The procedure yielded the positions of several particles in each of 600 frames. Large scale wave motion in the trough was superimposed on the diffusion of the droplets, therefore the average position of all the tracked droplets in the same video clip were subtracted from each individual position in order to get the pure diffusion. This data was then analyzed according to the method proposed by Saxton of summing every possible pair of data points for each particle in order to obtain an expression for the mean square displacement $\langle r^2(n) \rangle$ as function of n, stepsize expressed as a number of timesteps (Saxton 1997):

$$\left\langle r^2(n) \right\rangle = \frac{1}{N-n} \sum_{i=0}^{N-n} \left[\vec{r}(i+n) - \vec{r}(i) \right]^2 \qquad \text{Eq. 4.3}$$

Here N is the total number of datapoints, n is an integer between 1 and N, and r is the position as function of datapoint number.

As shown in Figure 26 there are fewer pairs of a given separation the longer this separating is, and they get less and less independent of each other. While there are N-1 steps of size one and they are all independent, there will only be two steps of size N-1, and these will be nearly identical. It is therefore obvious that the statistics will only be good for small step sizes. Figure 27 shows a plot $\langle r^2(t) \rangle$ (with n converted to the real time t) for one of the domains tracked, it is evident that it starts out approximately linear, and then deviated randomly when the statistics become bad.

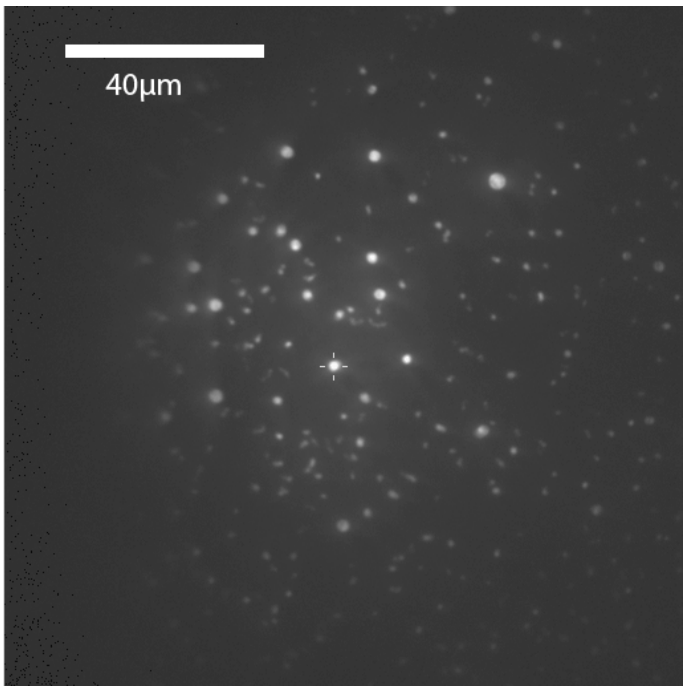

Figure 25: Snapshot of a video showing small droplets of fluorescently marked lipid diffusing. Tracking of individual droplets and estimating their size confirms the theoretical value of the friction due to water viscosity. The "thread cross" in the middle of the picture indicates that the image recognition software is tracking this droplet.

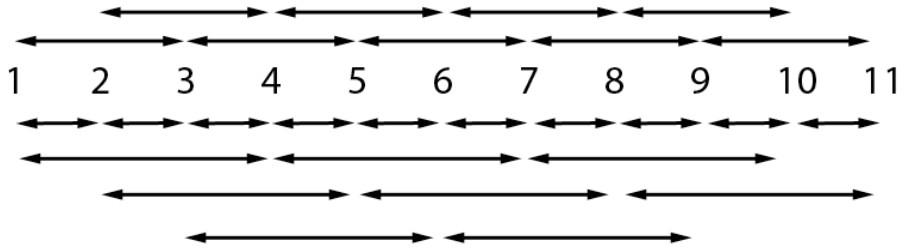

Figure 26: Illustration of the Saxton method of using all pairs. Above is represented a sequence of eleven datapoints of time and position (the numbers), with a total of ten time steps between them (the arrows immediately below). There are a total of nine possible pairs of data points separated by two time steps (the arrow on top), and eight pairs of points separated by three time steps (the three rows of arrows on the bottom).

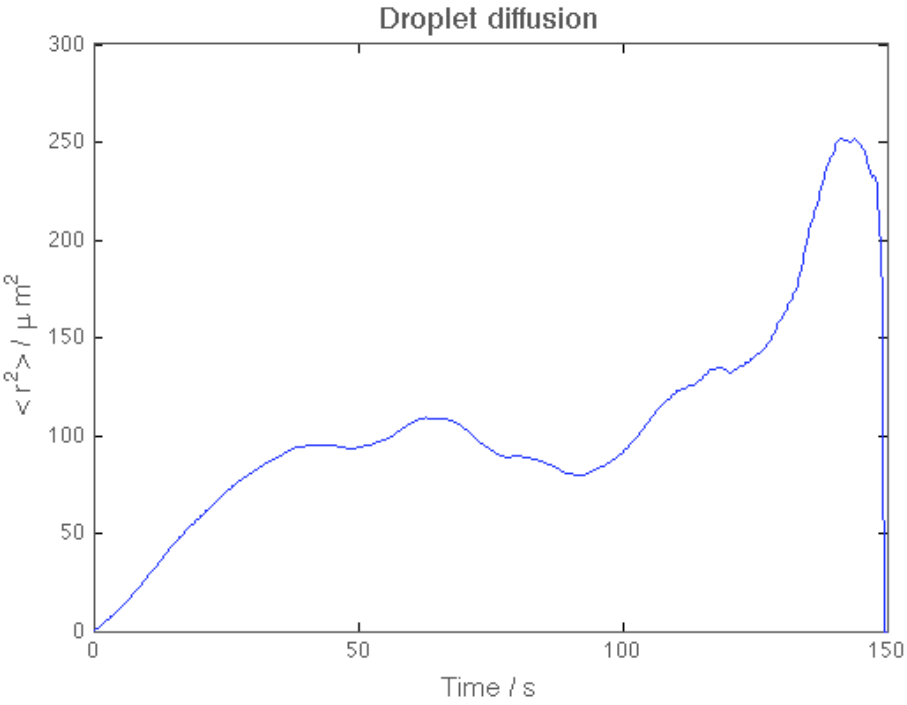

Figure 27: Representative example of mean square distance travelled by a lipid droplet as function of time. The graph is approximately linear in the first part; thereafter it deviates as the number of independent steps in the mean becomes low.

The slope of the linear part of Figure 27 is about 3µm²/s. This gives a diffusion constant of ~0.75µm²/s, from this one can calculate the radius R using Eq. 2.9:

$$\left\langle r^2 \right\rangle = 4Dt = \frac{3k_B T}{4\eta_w R} t \Leftrightarrow \qquad \text{Eq. 4.4}$$

$$R = \frac{3k_B T}{16\eta_w D} \approx 1\mu m \qquad \text{Eq. 4.5}$$

which agrees well with its observed radius. Because the radii of these small domains are hard to determine accurately these data was not examined further. Instead tracking was also done on a series of gas domains embedded in fluid phase. Due to their larger size compared the liquid domains discussed above they were tracked using a modification of the script used in the vesicle stretching analysis (chapter 6), this also made their radii much better determined than the above liquid domains. The function $\langle r(n)^2 \rangle$ was calculated for each tracked domain according to eq. 4.3.

The diffusion constant of each domain was calculated as the average of $\langle r(n)^2 \rangle / 4t(n)$ for each value of n from 11 to 50. Only these intermediate values of n were used because of the large uncertainty in the value determined at large n with data series of limited length, and because the uncertainty in the determined position of a domain leads to an overestimation of the diffusion coefficient at low n (Martin *et al* 2002). Figure 28 shows the reciprocal of the diffusion constant determined this way as a function of domain radius for 35 domains:

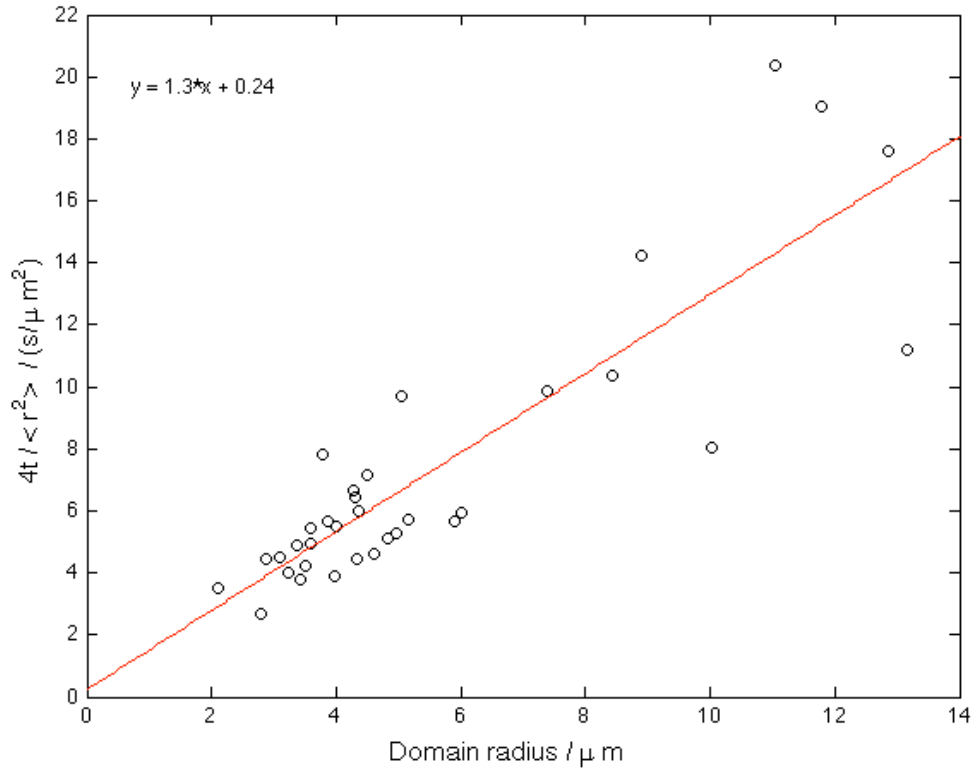

Figure 28: Inverse diffusion constant for gas bubbles, as function of their radius.

The linear regression in Figure 28 gives a slope of 1.3s/μm² in excellent agreement with the theoretically predicted constant of proportionality equal to:

$$\frac{1}{D\cdot R} = \frac{16\eta_w}{3k_BT} = 1.32\frac{s}{\mu m^3} \qquad \text{Eq. 4.6}$$

4.1.3 Bubble size distribution

In a recent paper Lee *et al* describes a new method to get both the line tension between two phases of a monolayer as well as the difference in dipole moment between them, by looking at the size distribution of domains (Lee *et al* 2011). The basis of this method is that domains should fluctuate in size rather than all having the same size. Smaller domains will be favored due to having a higher mixing entropy with the surrounding phase. Lee *et al* derives the following expression for the distribution of domain sizes:

$$C_N = \left(C_M \exp\left[-\beta \left(\frac{R_0}{R} - 1 \right)^2 \right] \right)^{\frac{R^2}{R_0^2}} \qquad \text{Eq. 4.7}$$

where C_N is the frequency of domains with radius R. C_M, β and R_0 are free parameters that can be fitted. Both R_0 and β have physical significance in that R_0 is the equilibrium domain radius as expected from a purely energetic consideration:

$$R_0 = \frac{e^3\delta}{4}\exp\left(\frac{4\pi\varepsilon\varepsilon_0\lambda}{\mu^2}\right) \qquad \text{Eq. 4.8}$$

and β is given by:

$$\beta = \frac{\mu^2 R_0}{4\varepsilon\varepsilon_0 k_B T} \qquad \text{Eq. 4.9}$$

The full derivation is described in (Lee 2011). By determining R_0 and β one can get λ and μ. Figure 29 shows a histogram over the distribution of sizes of 70 gas bubbles as well as a fit of eq. 4.7 to this data with the parameters C_N=0.1473, β=1.78 and R_0=7.53μm. From this one calculates:

$$\lambda = \frac{k_B T\beta}{\pi R_0}\ln\left(\frac{4R_0}{e^3\delta}\right) = 2.4\,fN \qquad \text{Eq. 4.10}$$

and

$$\mu = \sqrt{\frac{4\varepsilon\varepsilon_0 k_B T\beta}{R_0}} = 1.2\frac{pC}{m} \qquad \text{Eq. 4.11}$$

2.4 fN very low compared to the line tensions estimated by the other methods. 1.2pC/m certainly hits the right order of magnitude, but a precise estimation is made difficult by the fact that ε is not well known.

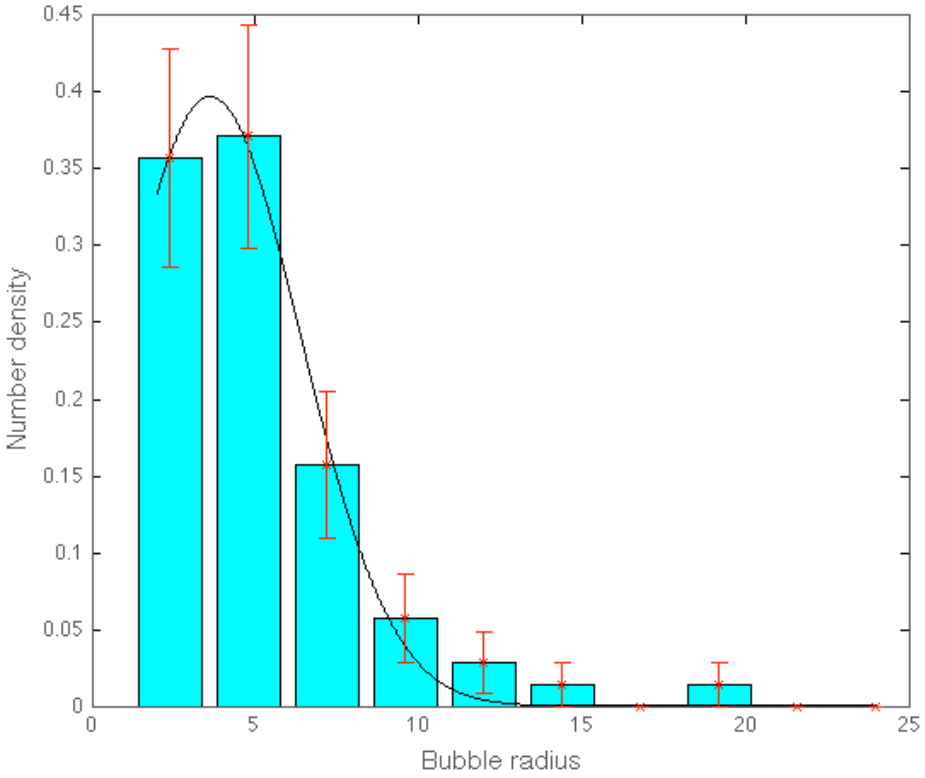

Figure 29: Histogram of experimentally determined number of domains of a given radius, as function of radius. The black curve is a theoretical distribution fitted to the histogram.

While the plot of Figure 29 looks reasonably convincing it is not likely to represent a true result. First of all this all presupposes that the monolayer is in equilibrium. As I have argued multiple times the morphology of monolayers tend to take a very long time to reach equilibrium.

The fitting of eq. 4.7 seems to be extremely dependent on the number of small domains. Whether the distribution keeps rising or falls as the radius goes towards zero plays a very large role in determining the optimum fit. Also the theoretical fit seems to consistently underestimate the number of domains at large radii. Incidentally the same is the case in (Lee 2011). I am not going to rush into critzizing

a PNAS paper with Jacob Israelachvili on the author list. Nevertheless I have my doubts about the reliability of this method.

4.1.4 Estimation of dipole moment and line tension from width of taut strings

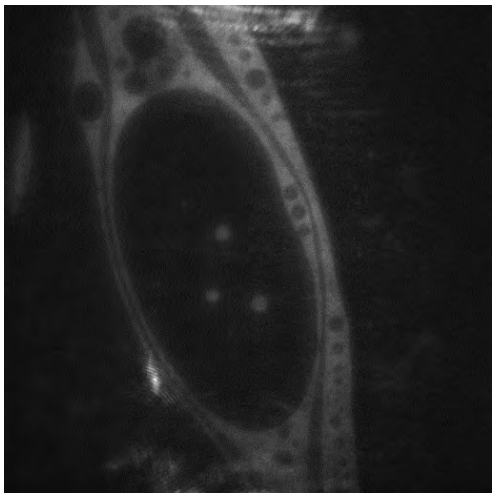

Figure 30: A big bubble in the middle of a string of fluid phase. The bubble is pushed flat by the line tension of two adjacent strings. This pressure also makes the strings visibly thinner where they are stretched across the bubble, compared to the area around. The top and rightmost ones has been kept widened by included bubbles which are not yet finished moving away from the strained region, but the lower and leftmost ones appear to have reached an equilibrium thickness which lends itself to analysis.

Figure 30 shows an interesting non-equilibrium structure. A large gas bubble sits in the middle of a fluid string. On either side of it is two other strings. Because the amount of gas phase between the strings is limited, and equilibration is slow, these extra strings are forced to bend around the bubble. The line tension of the bubble edge works to make it round, but both the outer edge of the string, as well as the two other strings exerts a pressure on it from the sides, forcing it to adopt a non-circular shape.

On the right side the strings are full of smaller bubbles making analysis difficult, but on the left side both strings are clean and stretched thin. If we assume that these strings have reached a metastable equilibrium in which electrostatic repulsion between the phases prevents further thinning, then these can be made subject to a quantitative analysis allowing the calculation of a ratio between the dipole moment density difference (squared) and the line tension. The advantage is that this analysis will be independent of the molecular cut-off distance δ, which usually enters these calculations.

The curvature of the strings is low enough, and their aspect ratio high enough that we can approximate them as infinite straight strips of finite width for the purpose of calculation of electrostatic energy. I will further assume that there exists a reservoir of both fluid and gas phase at the end of the strings which allows their thickness to equilibrate (i.e. that the lines are thick enough in the places where they are not stretched across the bubble that the electrostatic energy means much less here and the thickness is simple defined by the overall amount of gas/fluid in the strip). The electrostatics work to broaden the strips (both gas and fluid) in theory ad infinitum, but in practice only until the thickness would become comparable to

the thickness of the rest of the strip and the reservoir assumption breaks down, after this the thickness would be defined by the overall amount of material in a strip. It may seem counter-intuitive that the electrostatic force would work to broaden a domain strip, after all it is a repulsion between like phases which normally work to limit domain size. Again it is necessary to remember that this is a non-equilibrium situation and is dependent on the assumption of a wider strip above and below. Thinning a strip in one place means moving material away and broadening it somewhere else. This means that the two adjacent domains will move closer to each other in this place and further apart somewhere else. Without the bubble the metastable equilibrium would be equal width along the entire length of each strip. In the following calculation the width of each strip is calculated by setting the dipole moment of the phase in question, and thereby also its electrostatic energy, to zero (allowed by the superposition principle); and considering its equilibrium shape from the point of view of the adjacent phase. The reservoir assumption basically means that away from the bubble the distance between the adjacent phases is large enough that their repulsion can be ignored when compared to the larger force across the narrow strips at the bubble. This may not strictly be the case for the outermost fluid string, which does seem a bit thinner than the innermost, but it shouldn't affect the result of the calculation much.

As mentioned earlier the field at a given point due to an infinite line of dipole moment density μ and thickness dy passing a distance y from a point is:

$$dE = \frac{\mu}{\varepsilon\varepsilon_0} \cdot \frac{2}{y^2} dy \qquad \text{Eq. 4.12}$$

For a strip of finite width, extending from distance a to distance b, the field therefore becomes:

$$E = \frac{2\mu}{\varepsilon\varepsilon_0}\left(\frac{1}{a} - \frac{1}{b}\right) \qquad \text{Eq. 4.13}$$

For strips of constant width w the electrostatic energy for two strips of length L, as function of the distance d between them will therefore be:

$$U(d) = \frac{-2\mu^2 L}{\varepsilon\varepsilon_0} \int_0^w \left(\frac{1}{d+w-x} - \frac{1}{d+2w-x}\right) dx \qquad \text{Eq. 4.14}$$

$$U(d) = \frac{-2\mu^2 L}{\varepsilon\varepsilon_0} \ln\left(\frac{d^2+2wd}{(d+w)^2}\right) \qquad \text{Eq. 4.15}$$

Competing with the electrostatic repulsion is the pressure inside the bubble, which is defined by the line tension of the system and the radius of curvature of the lines.

The strips are pushed together by the difference in surface pressure $\Delta\Pi=4\lambda/R$ giving a contribution of $\Delta\Pi \cdot d \cdot L$ to U(d). These contributions are added; the expression is differentiated with respect to d and set equal to zero, in order to find the stable distance at which the energy is minimal:

$$\Delta\Pi(2w^3d + w^2d^2 + 2wd^3 + d^4) = \frac{4\mu^2}{\varepsilon\varepsilon_0}(w^3 + w^2d - wd^2) \qquad \text{Eq. 4.16}$$

Due to the superposition principle the energy of the gas strip in the middle can be evaluated as function of the strip widths in the same way:

$$U(w) = \frac{-4\mu^2 L}{\varepsilon\varepsilon_0}\left(\int_0^d\left(\frac{1}{w+x}\right)dx + \int_0^\infty\left(\frac{1}{2w+d+x}\right)dx\right) \qquad \text{Eq. 4.17}$$

the factor of four rather than two comes from the fact that there is two large gas areas on either side of the strip, which contribute the same. There is only one term in the first integration because the other edges of these gas areas are deemed to be so far away that they contribute nothing. With the second integration (the interaction of the two infinite gas phases) we get a problem. The integration does not converge. As we already know the energy between two infinite phases of a monolayer is infinite. Fortunately we are not interested in the energy between them, but in the force, which does remain finite, it just has to be evaluated in another way. Setting the limit large, but finite, instead solves the problem.

$$U(w) = \frac{-4\mu^2 L}{\varepsilon\varepsilon_0}\left(\int_0^d\left(\frac{1}{w+x}\right)dx + \int_0^Q\left(\frac{1}{2w+d+x}\right)dx\right) \quad , \quad Q >> w,d \qquad \text{Eq. 4.18}$$

$$U(w) = \frac{-4\mu^2 L}{\varepsilon\varepsilon_0}\left(\ln\left(\frac{d+w}{w}\right) + \ln\left(\frac{2w+d+Q}{2w+d}\right)\right) \qquad \text{Eq. 4.19}$$

adding $2 \cdot \Delta\Pi \cdot w \cdot L$ to U(w) since there are two strips of width w, differentiating with respect to w and setting equal to zero, yields:

$$2\Delta\Pi = \frac{4\mu^2}{\varepsilon\varepsilon_0}\left(\frac{d}{dw+w^2} + \frac{2Q}{(d+2w)(d+Q+2w)}\right) \qquad \text{Eq. 4.20}$$

Using Q>>w,d then simplifies it to:

$$2\Delta\Pi = \frac{4\mu^2}{\varepsilon\varepsilon_0}\left(\frac{d}{dw+w^2} + \frac{2}{(d+2w)}\right) \qquad \text{Eq. 4.21}$$

$$2\Delta\Pi = \frac{4\mu^2}{\varepsilon\varepsilon_0}\left(\frac{d^2+4dw+2w^2}{(dw+w^2)(d+2w)}\right) \qquad \text{Eq. 4.22}$$

$$2\Delta\Pi = \frac{4\mu^2}{\varepsilon\varepsilon_0}\left(\frac{d^2+4dw+2w^2}{d^2w+3dw^2+2w^3}\right) \qquad \text{Eq. 4.23}$$

$$2\Delta\Pi(d^2w+3dw^2+2w^3) = \frac{4\mu^2}{\varepsilon\varepsilon_0}(d^2+4dw+2w^2) \qquad \text{Eq. 4.24}$$

Eq. 4.16 and eq. 4.24 can be combined to form a seventh order equation in w and d, which when solved numerically gives just one set of positive real solutions:

$$w \approx 1.91d \qquad \text{Eq. 4.25}$$

which agrees well with what is seen on Figure 30. The distance involving d and w most easily determined on Figure 30 is the peak to peak distance of the two lines, this is equal to w+d and is found to be 2.4µm (see Figure 31). w is therefore estimated to be 1.58µm and d=0.83µm. Inserting thesse values in eq. 4.19 or eq. 4.27 one obtains:

$$\Delta\Pi = 1.44\mu m^{-1}\cdot\frac{\mu^2}{\varepsilon\varepsilon_0} \qquad \text{Eq. 4.26}$$

The radius of curvature is measured to be about 100µm and we can therefore get the ratio between the squared dipole moment density and the line tension:

$$\Delta\Pi = \frac{4\lambda}{R} = \frac{4\lambda}{100\mu m} = 1.44\mu m^{-1}\cdot\frac{\mu^2}{\varepsilon\varepsilon_0} \Leftrightarrow \lambda = 36\frac{\mu^2}{\varepsilon\varepsilon_0} \qquad \text{Eq. 4.27}$$

If we assume a dipole moment density 3.34 pC/m (agreeing with the measurement in Figure 35) and a relative permittivity of the interface layer of 36 then we get a line tension of 1.26pN. This is a rather large value, but consistent with other line tensions reported for pure systems (Wurlitzer et al. 2000).

Because equilibrium domain sizes depend exponentially on the line tension a line tension this large means that the equilibrium domain size will be huge. Inserting eq. 4.33 into the expression for equilibrium radius from (Lee 2011) we get:

$$R_0 = e^3\delta/4\cdot\exp(4\pi\cdot 36) \qquad \text{Eq. 4.28}$$

This means that equilibrium domain size is much bigger than the size of the observable universe (almost 200 orders of magnitude greater than δ), making the gas-LE transition for all practical purposes a first order transition.

A second advantage of this method, in addition to not depending on the exact value of δ, is that the effects are linear in the ratio between line tension and dipole moment density, rather than exponential. That means that it is applicable over a wide range of values of this ratio. The domain size distribution method described in chapter 4.1.3 is obviously not applicable when the equilibrium domain size is larger than the universe.

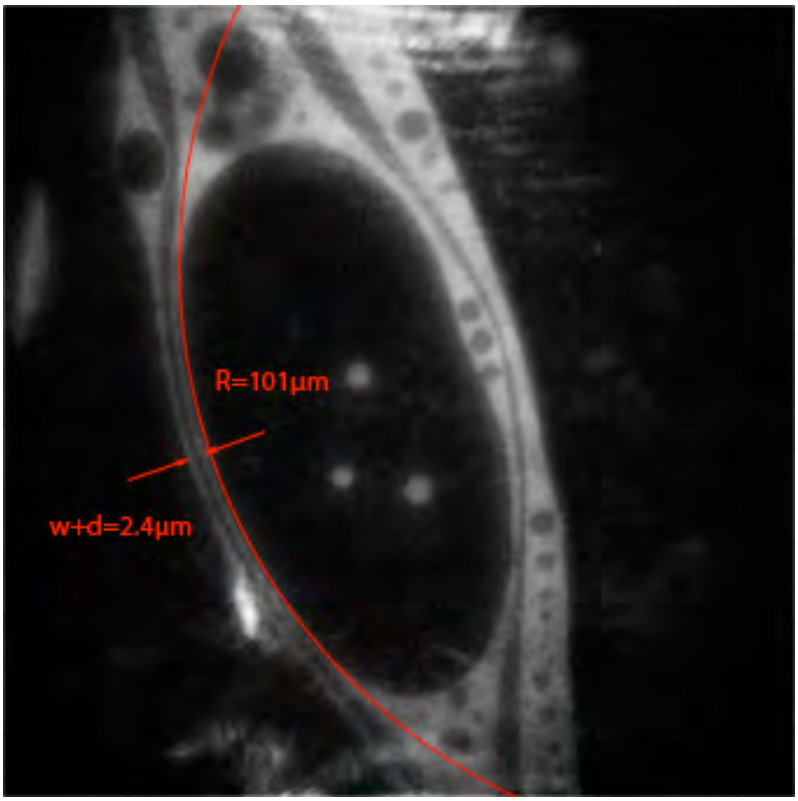

Figure 31: The peak-to-peak distance between the two lines is approximately 2.4µm and their radius of curvature is 101µm.

If indeed the reservoir assumption was not applicable to the outer string then it means that the pressure in it is slightly lowered and it is thinned which does seem to be the case. This thinning in turn reduces the repulsion between the two strips and allows the middle dark strip to thin slightly compared to the calculated value. However the inner strips width is dominated by the repulsion of the large dark areas and is therefore almost unaffected, and it clearly is connected to the wide central strip. Since the difference in width between the two wide strips is not very

large we conclude that the reservoir assumption does not perturb the result by very much.

This method does require a suitable bubble to be found, and that it has reached the metastable equilibrium. The much wider strings on the right side of the bubble seems to indicate that this method is not particularly trustworthy.

4.1.5 Linetension dragging gas domain

Linetension can also be measured by dynamic methods. A video were recorded, which showing a gas domain being dragged along by linetension after a long gas string had broken. Four consecutive frames were analyzed to find speed of movement as shown in Figure 32. The length of the string were plotted as a function of the timing of the frame, and a linear regression gave a speed of 4.1µm/s (see Figure 33). Using this the line tension is calculated as:

$$F = 2\lambda = \frac{16\eta_w r}{3} v = \frac{16 \cdot 10^{-3} pa \cdot s \cdot 7.6\mu m \cdot 4.1\mu m/s}{3} = 0.17 pN \qquad \text{Eq. 4.29}$$

This is a somewhat lower line tension than measured by the other methods. One must assume that there has been some contamination by line active agents in this case. For example (Courty et al. 2003) measured 2.4pN in pentadecanoic acid by a similar method.

In eq. 529 it is assumed that the domain is always moving at terminal speed, and that inertial effect can be ignored. This assumption can be verified by estimating the Reynolds number of the accompanying flow in the subphase. With a domain speed 4µm/s one gets a Reynolds number of:

$$\mathrm{Re} = \frac{\rho v L}{\eta_w} = \frac{1000 \frac{kg}{m^3} \cdot 10\mu m \cdot 4\mu m/s}{0.001 pa \cdot s} = 4 \cdot 10^{-5} \qquad \text{Eq. 4.30}$$

this is so low that it should be safe to neglect inertial effects in all cases.

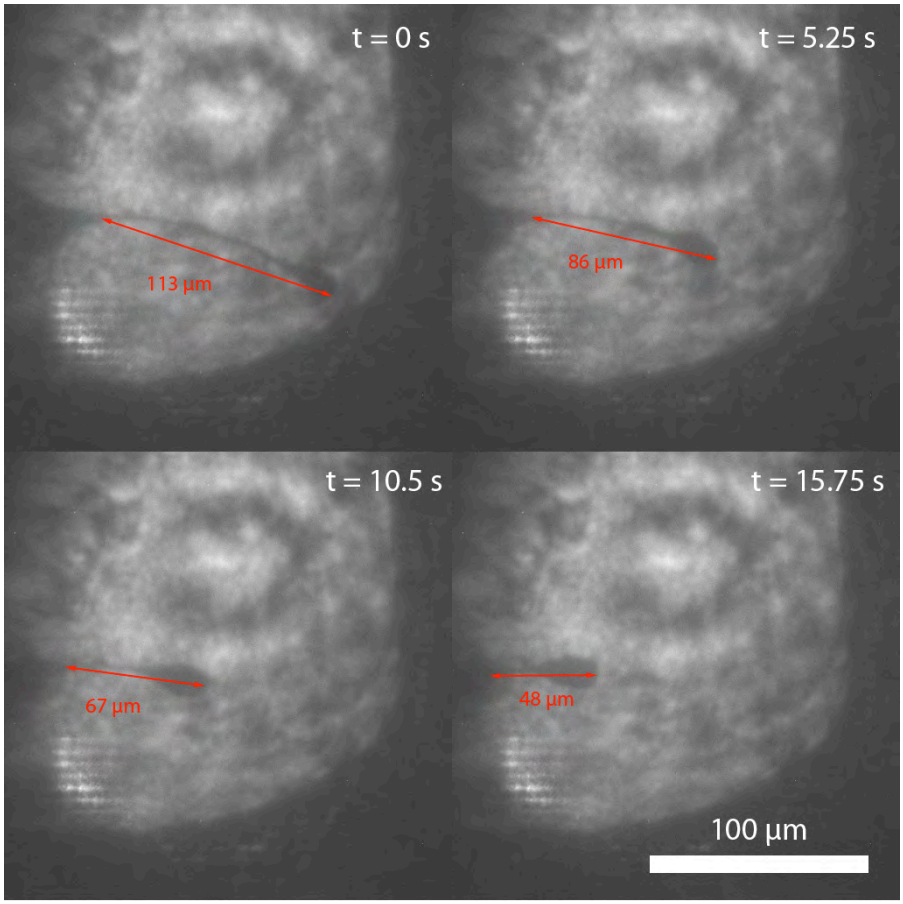

Figure 32: Small gas domain being dragged across a monolayer by the line tension after a string of gas phase has recently broken. Analyzing the speed at which the domain is being dragged gives allows an estimate of the linetension.

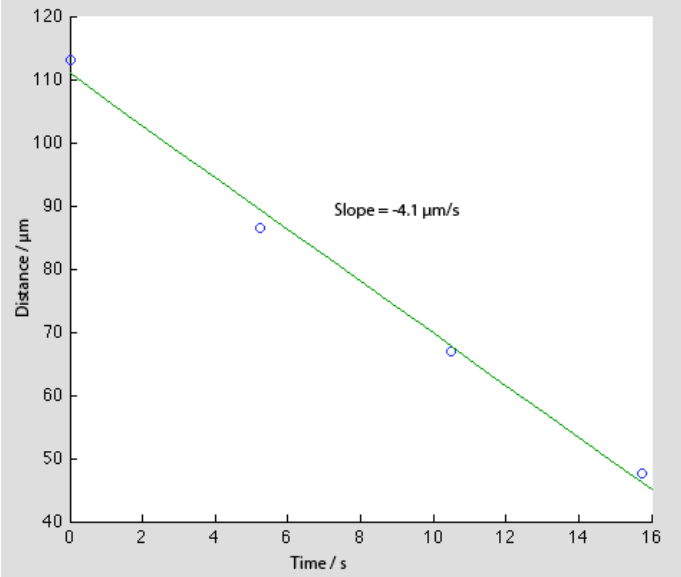

Figure 33: Plot of the data from Figure 32, showing the domain moving at an average speed of 4.1µm/s. The speed is actually falling gradually since the diameter of the domain increases as more of the string is absorbed into it.

4.1.6 Photosystem one in a monolayer

In order to test the new two-color capability of the instrument a small sample of photosystem one (PSI) in aqueous solution was reacted with Alexa635® reactive dye and added to a DPPC monolayer. PSI is very stable for a membrane protein; it is one of the few membrane proteins, which has been crystallized and is known to be stable in Langmuir films as well.

A series of movies were made, alternatingly recording the organization of PSI using the red fluorescence of the Alexa® dye and the green fluorescence of rhodamine labeled lipids. Figure 34 shows an example image from such a movie. It is clearly visible that the protein goes to the the domain boundaries.

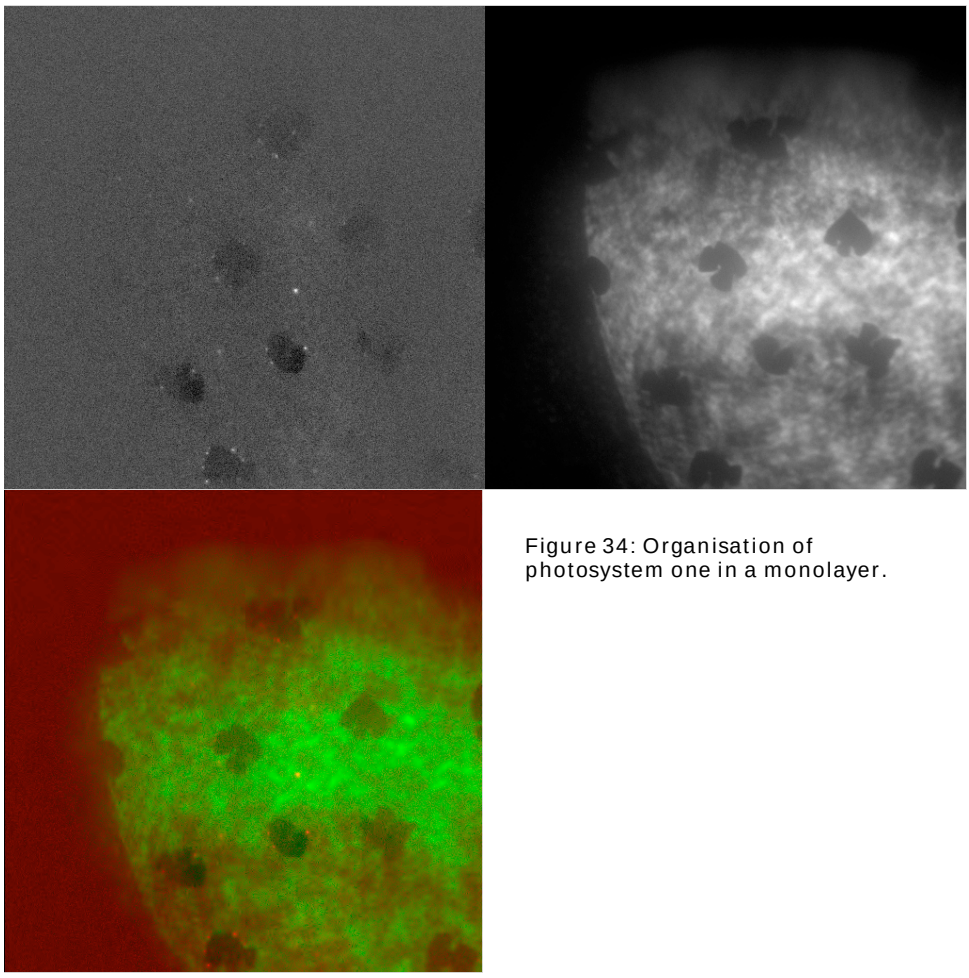

Figure 34: Organisation of photosystem one in a monolayer.

4.1.7 Voltage effects

In biological cell membranes large voltages are present. Typically membranes are subject to a voltage drop on the order of a hundred millivolts. When taken into consideration that a membrane is only about 5 nanometers thick this amount to electric fields of up to 20MV/m. Such fields readily causes electrical breakdown in air. The effect of the transmembrane voltage on proteins is the core in the Hodgkin-Huxley model of the action potential, but fields of this magnitude would also be expected to have a rather profound effect on the thermodynamics of a membrane. Yet it is quite sparsely studied.

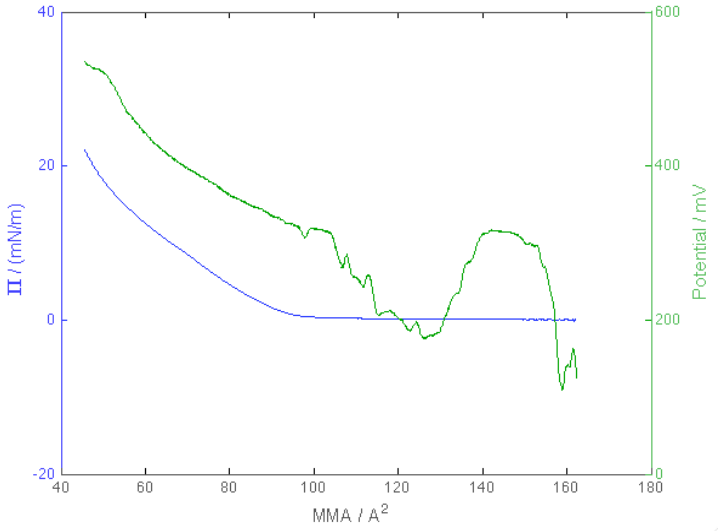

Figure 35: Surface potential (green line) of a DPPC monolayer recorded with a Kelvin probe as function of MMA. Plotted along with the pressure isotherm of the same layer. In the gas/LE phase the potential is seen to be highly unstable, indicating that the layer is very inhomogenous at scales even larger than the ca. 10mm² area probed. At the onset of pure LE the potential becomes stable at about 370mV and then gradually increases as the layer is further compressed.

It has been known for some time that applying a potential to an electrode above the surface can electrophorese monolayer domains. (For example: Miller & Mohwald 1986, Heckl et al. 1988, Flörsheimer & Möhwald 1989). It has been used to manipulate solid domains into fusing with each other (Flörsheimer & Möhwald 1990).

In order to get a better understanding of the effects of voltages on monolayers an electrode was made by mounting a wire on a translational micrometer stage on a piece of plastic straddling the Langmuir trough. The position of the wire above the surface could then be controlled with micrometer precision. The wire was connected to a variable DC voltage supply. For counter electrode a metal ring was

produced that would fit into the metal holder for the coverglass. Figure 36 show a photograph of the setup with electrode, while Figure 37 shows it in schematic form.

It was considered whether salt needed to be added to the subphase to make it conducting, since the subphase is considered the counterelectrode rather than the coverglass holder. However, a quick calculation using conservative estimates for dimensions rather than taking the complicated shape of the problem into account shows that even ultrapure water is more than conductive enough. If we look at the

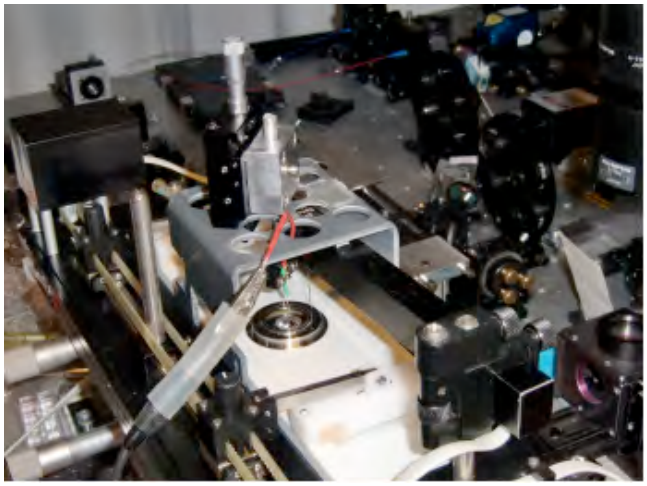

Figure 36: Photograph of the PTFE through (white) straddled by the electrode holder in grey plastic.

water-electrode gap as a capacitor, the very tip will hold most of the charge required to set up the field. Using one millimeter squared as the area of the contributing part of the tip and 30µm as the distance we get a capacitance of around 300fF. Considering the water between the glass holder and the surface under the tip as a wire with dimensions 1mm*1mm*1cm, gives a resistance of 1.8GΩ when using the Millipore water conductivity of 0.055µS/cm. This in total gives a charging time of the capacitor in this RC-circuit of circa 500µs. Every assumption in this calculation has been to overestimate the charging time. In reality the current will not be restricted to a narrow wire through the water, and it will be shorter than a centimeter making the resistance, and thereby the time, an overestimation. This shows that the field will reach equilibrium quickly and that salt is not necessary to enhance the conductivity.

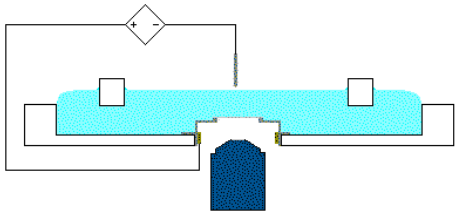

Figure 37: Schematic cross section drawing of the trough with water (light blue), barriers (white squares), objective (dark blue) and a voltage applied between the metal coverglass holder and an electrode suspended above the water surface.

With this setup it was possible to move domains around on the surface. This was tried on the LE-gas coexistence phase. It was found that a positive potential on the electrode in the air

repels the bubbles/attracts the fluid, and vice versa for a negative. This is consistent with the dark phase being more sparsely populated with lipids than the light phase.

In very high fields a problem arises in the fact the water surface becomes unstable. Water, as a dielectric (and even conductor) is strongly attracted to regions of high electric field. When the fields get too strong, the surface is deformed and attracted to the electrode, shorting out the setup. If the water is taken to be a conductor, as has been previously argued is a good approximation, then the surface will, in equilibrium, satisfy the following equation:

$$0 = \sigma E + 2\gamma H - \rho g h \qquad \text{Eq. 4.31}$$

Where σ is the surface charge, E is magnitude of the electric field at the surface, γ is the surface tension, H is the mean curvature, ρ is the density of the water, g is the gravitational acceleration and h is the surface height. Since the field inside the conductive water must be zero, by Gauss law E and σ are related through

$$E = \frac{\sigma}{\varepsilon_0} \qquad \text{Eq. 4.32}$$

and eq. 4.34 can be written as:

$$0 = E^2 \varepsilon_0 + 2\gamma H - \rho g h \qquad \text{Eq. 4.33}$$

Therefore, a local high field needs to be balanced by either a large negative curvature or a large height local height of the surface. A quick order-of-magnitude calculation shows that the last term in equation 4.36 is almost negligible in most practical cases, h would need to be on the order of several centimeters. The optimal *would* still be to use a hydrostatic pressure to counteract the pull of the field, but it would tend to be very unstable since a raising height will mean that surface and electrode gets closer together making the field stronger at constant voltage. Electrode and surface therefore would need to be far from each other compared to h in order to minimize this instability. As h is already large, and the used voltage will increase with surface-electrode distance, using height to balance the electrostatic force is very impractical.

The curvature of the surface (middle term of eq. 4.36) on the other hand will have to be at least on the scale of the separation of the electrode and the surface. This means that in this case higher fields can be reached by using a sharper electrode, closer to the surface. This also means that the curvature will be higher, which may influence the surface in other ways than purely through the field.

A hope was that a strong enough field could force a monolayer into the main transition locally. By doing this it would be possible to activate the activity of the enzyme phospholipase A_2 (PLA_2), which just like photosystem one have been shown to aggregate at domain boundaries, although this protein adsorbs below monolayers rather than incorporate it self into them (Gudmand 2002). PLA_2 hydrolyses one of the ester bonds of phospholipids, but it is dependent on the large fluctuations of a domain boundary in order to be active. Once it starts the hydrolysis products lowers increases disorder in the local area and accelerates hydrolysis, therefore it should be possible to initiate a large burst in activity by applying an electric field in case said field could force a phase transition. Figure 38 shows domains being hydrolysed at about 6mN/m where LC phases is present all over the layer.

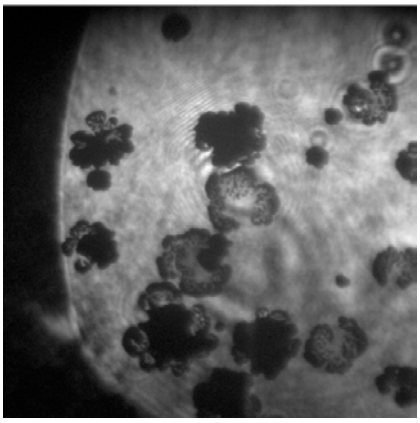

Figure 38: Appearance of a DPPC monolayer in the microscope when domains are being hydrolysed by PLA_2. (Subphase pH 8.9 Tris buffer with 150mM NaCl and 5mM$CaCl_2$)

In order to circumvent the problems with using high field strenghts it was attempted to fashion an electrode insulated by a glass pipette (Figure 39). A similar approach is described in literature (Yee et al. 1995). Yee et al managed to push a monolayer through its phase transition with a glass insulated electrode protruding through the monolayer. The attempt to reproduce this was unsuccessful.

A reason that the reproduction attempt failed could be that the field attracted the water to form a thin layer around the electrode, shielding the field. This would make the remaining field on the part of the surface in the focal plane negligible.

An insulated wire covered by a layer of conductive water can be treated like a coaxial cylinder capacitor. It has a capacitance per unit length of

$$\frac{C}{L} = \frac{2\pi\varepsilon_r\varepsilon_0}{\ln\left(\frac{b}{a}\right)} \qquad \text{Eq. 4.34}$$

Where ε is the relative permittivity of the insulating dielectric, in this case the glass pipette, and ε_0 is the vacuum permittivity. A charged capacitor contains an energy of

$$U = \tfrac{1}{2}CV^2 = \frac{Q^2}{2C} \qquad \text{Eq. 4.35}$$

In order to find the force acting on the sheath of water this energy is differentiated with respect to the length of the covered part[3].

$$F_{el} = -\frac{dU}{dL} = \frac{Q^2}{2C^2}\frac{dC}{dL} = \frac{Q^2 \ln\left(\frac{b}{a}\right)}{4\pi\varepsilon_r\varepsilon_0 L^2} = \frac{\sigma^2\pi\ln\left(\frac{b}{a}\right)b^2}{\varepsilon_r\varepsilon_0} = E^2\pi\ln\left(\frac{b}{a}\right)b^2\varepsilon_r\varepsilon_0 \quad \text{Eq. 4.36}$$

Water will creep up around the electrode when this force exceeds the force generated by the surface tension of the water (and as L grows, gravity). Even if the glass insulation were completely hydrophobic with a contact angle of 180 degrees, the force generated is only:

$$F_\gamma = 4\pi\gamma b \quad \text{Eq. 4.37}$$

By equating eq. 4.39 and eq. 4.40 we get

$$4\pi\gamma b = E^2\pi\ln\left(\frac{b}{a}\right)b^2\varepsilon_r\varepsilon_0 \Leftrightarrow E = \sqrt{\frac{4\gamma}{\ln\left(\frac{b}{a}\right)b\varepsilon_r\varepsilon_0}} \quad \text{Eq. 4.38}$$

If the field exceeds this value the water will start creeping up around the electrode. The glass being hydrophilic or the surface tension being reduced by lipids only makes it worse. The appearance of b in the denominator once again means that the electrode should be small in order to be able to use strong fields.

Using a diameter of the electrode of 15µm and 50µm for the glass insulation, one calculates a field strength of about 10MV/m, about half the typical physiological field. This limit will be reached at an applied voltage of 500-600V.

If stronger fields were used then electrical breakdown of the glass insulation were observed. The current emitted from the electrode in such cases tended to change the monolayer and often destroyed the fluorescence in the area, occasionally producing images similar to the ones of Yee *et al*. This behavior was initially misinterpreted as a success in the reproduction of the results of (Yee *et al* 1995).

[3] Differentiation is of course done with charge held constant rather than voltage even though a voltage source would likely be employed to keep the voltage constant. This is important to obtain the correct force felt by the water. In reality the energy stored in the capacitor will increase as water creeps up and enhances the capacitance but this energy is supplied by the voltage source. At the top of the proposed water sheet the field will have complicated fringes, but as long as the length of the bare and water parts of the electrode are long compared the diameters, this method should yield the correct behavior.

Free energy is a state function. Therefore the fact that LC domains are attracted to a positive electrode should also mean that they would preferably form under the electrode. The lipids are closer packed, this mean they have a higher dipole moment, which accounts for the attraction, that they are closer packed also accounts for the fact that they form at higher surface pressures, in the end this is the same thing.

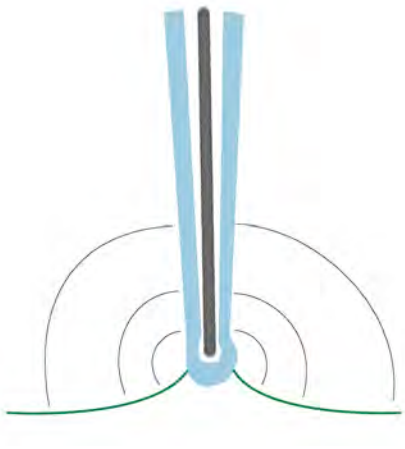

Figure 39: Schematic drawing of glass-insulated electrode (gray and blue) touching water surface (green) allowing for investigation of the effect of high electric fields (visualized as curved lines) in the area around it

Since the monolayer, regardless of phase, is attracted to the area under a positive electrode, the surface pressure will increase here. With a monolayer dipole density of 1 Debye / 50Å^2 a field of 10MV/m the increase in pressure will be:

$$\frac{3\cdot 10^{-30} Cm}{5\cdot 10^{-19} m^2}\cdot 10^7 \frac{V}{m} = 6\cdot 10^{-5} \frac{N}{m} \qquad \text{Eq. 4.39}$$

This is a very small difference, comparable to the overpressure inside a bubble of several micrometers dimension. With this small difference it is understandable why it is so hard to make domains spontaneously form. Domains might be marginally more stable under the electrode but the difference in growth rate under the electrode and away from it is likely to be minimal, as evidenced by the fact that domains which have grown quickly take hours to equilibrate in size and shape under the pressure of line tension; which is, as shown, on the same order of magnitude.

Still the clumpings of domains under an electrode are very tight (see Figure 40 and Figure 41) leaving very little LE phase between them, reminiscent of how the monolayer looks at much higher pressures. Evidently overcoming the domains mutual repulsion is not the main barrier to reach a state where the monolayer is mostly LC. This means that something else is forcing the pressure higher in an almost-all-LC monolayer. An obvious possibility is impurities in the LE phase, among which is of course the fluorescent dye. When domains collect under the electrode the dye stays in the LE phase in the rest of the trough, whereas when the entire film is compressed the dye is concentrated in the remaining strips of LE phase lowering the chemical potential of the fluid phase and therefore increasing the required pressure. That the pressure corresponding to the field required to condense domains so closely when impurities can escape, is so low indicates that the transition of a pure film would really be very close to first order.

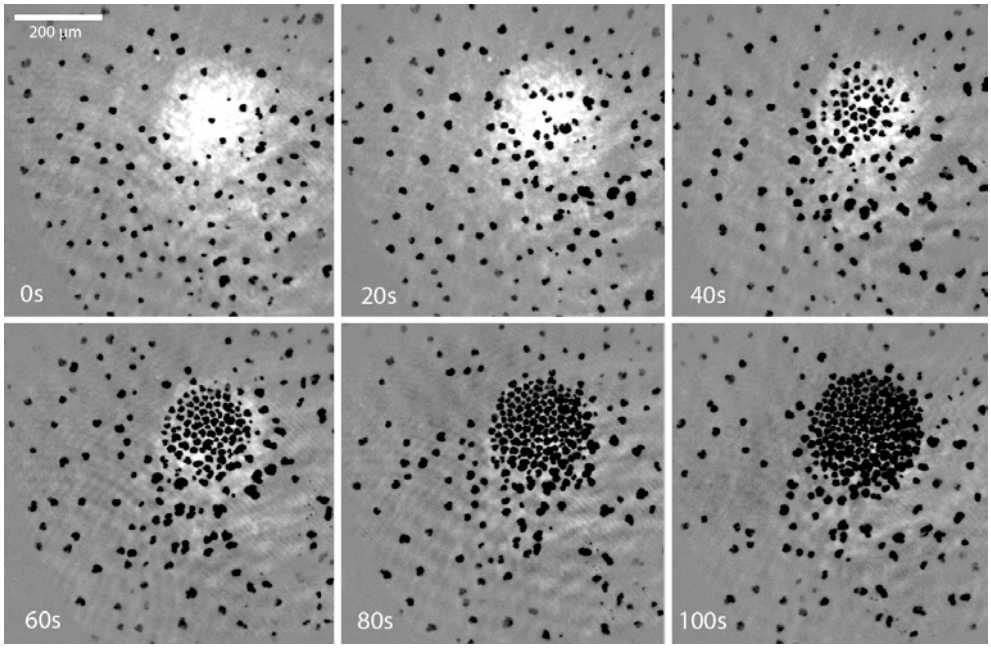

Figure 40: Image series of domains being attracted to the area beneath an electrode. Enhanced as described in appendix B.

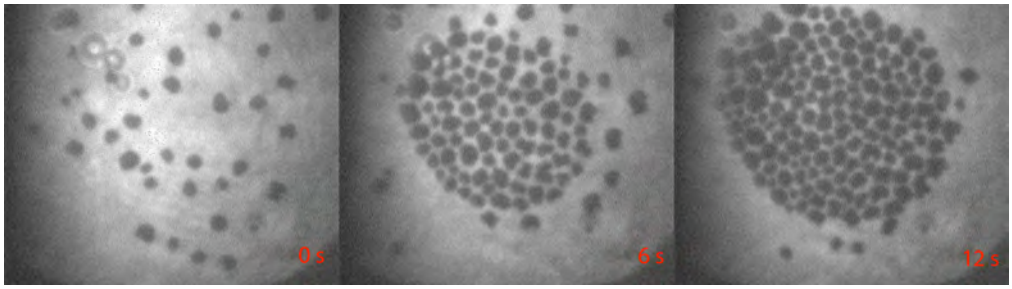

Figure 41: Another image series of attraction of gel phase domains to an electrode

4.1.8 Tracking of domains under influence of voltage

Domains under influence of an electrode 75 µm above the surface with a voltage of 100V applied, was tracked manually so that their trajectories could be compared to theory.

Speed was compared to domain size (determined by marking several points along their perimeter and using the shoelace formula for calculating polygon area).

A dipole moment of p under an electric field gradient of E' is subject to a force of:

$$F = p \cdot E' \qquad \text{Eq. 4.40}$$

p is equal to area A time dipole moment density μ. This is inserted and F is put equal to the expression for friction:

$$\frac{16\eta_w r}{3} v = A\mu E' = \pi r^2 \mu E' \Leftrightarrow \qquad \text{Eq. 4.41}$$

$$\frac{v}{r} = \frac{3}{16\eta_w} \pi \mu E' \qquad \text{Eq. 4.42}$$

v/r for the tracked domains were plotted as function of distance ρ from the center of the electrode along with the theoretical prediction (described in appendic C) assuming a dipole moment density of 1pC/m in Figure 42. The result seems to agree with theory although this does not appear to be a method to draw quantitative conclusions from.

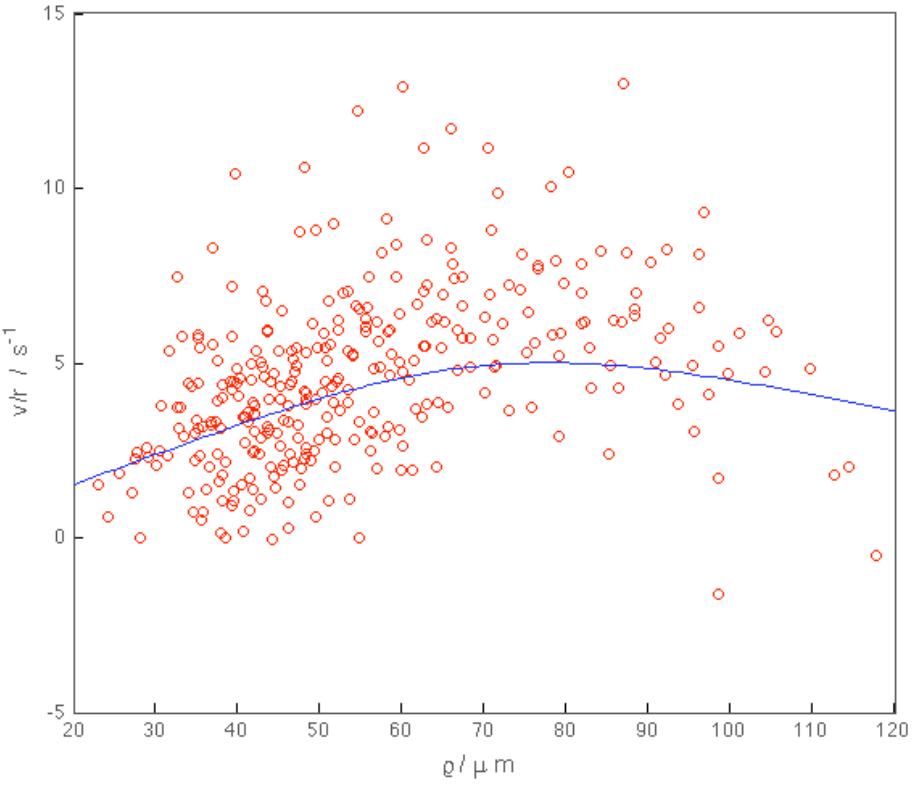

Figure 42: Movement of domains under influence of a charged electrode. Red circles: Instantaneous (frame to frame) radial velocity of domains, divided by domain radius, as function of their distance to the axis of the electrode. Blue line: Theoretical prediction assuming a dipole moment density between phases of 1pC/m, based on numerical simulation of the field surrounding the electrode. (See appendix C)

4.2 Summary

Many different techniques for evaluating the line tension, and dipole moment of lipid monolayers have been tested and discussed, including:

- The width of domain strips in balance between line tension and electrostatic repulsion (both).
- Domain size distribution (both).
- Dynamic dragging of domain by line tension (line tension).
- Electrostatic attraction of domains (dipole moment).
- Kelvin probe (dipole moment).

Further the assumptions of the frictious forces in the subphase used in the line tension dragging and the electrostatic dragging experiments were tested by examining the diffusion of small domains by individual tracking.

The recorded pictures show the extremely complicated morphology that can arise due to the high line tension and dipole moment density differences of pure lipid monolayers in the fluid-gas coexistence regime. Photosystem one was incorporated into a monolayer, and found to preferentially position itself on the domain boundaries, illustrating the effect that the phase behavior of lipids can have on membrane organization.

5 Nanodiscs

5.1 Introduction

Nanodiscs are small self-assembled patches of lipid bilayer enclosed in a membrane scaffold protein (MSP) ring. The MSP is made up of amphifillic alpha helices with a hydrophobic part on the inside against the fatty acids of the lipids, and a hydrophobic side on the outside of the ring exposed to the surrounding aqueous solution. In this way they protect the hydrophobic interior of the lipid bilayer from exposure to water, the entire surface of the disc is hydrophilic and the disc is water-soluble.

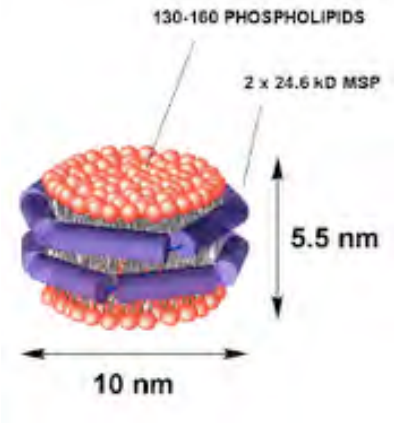

Figure 43. Schematic representation of a nanodisc. Phospholipid heads are red and the MSP proteins purple. Picture taken from www.mcntc.illinois.edu/

Nanodiscs have a well-defined shape and size due to the controlling nature of the monodisperse MSP.

They have been offered as a possible way to study membrane proteins in a much less disruptive manner than other techniques. Only a minute minority of the proteins, which have been structurally solved, are membrane proteins. Because of membrane proteins natural environment being made up of both the very hydrophobic membrane core and the aqueous solutions bordering the membrane, they tend to denature both in organic solvents as well as in water. This means they don't take attempts at crystallizing them very well and can therefore not be characterized by techniques like x-ray crystallography in the majority of cases.

5.2 Materials and methods

MSP protein were reacted with Alexa633 succimidyl ester reactive dye, and subsequently purified and used to make nanodiscs by Jens Bæk Simonsen. Dye and protein were used in stochiometric amounts, so each protein was marked by one dye molecule on average. In reality the marking is of course expected to exhibit a Poisson distribution. Since every disc contains two proteins the average number of dyes per disc is also two. The lipids used to make the discs contained about 0.4% lissamine (rhodamine labeled DMPC) giving one marked lipid per disc on average.

Since the neutron scattering experiments were done on a heavy water subphase, it was decided to do the FCS experiment in the same way in order to eliminate a parameter that could potentially change the result. The higher density of the heavy water might help the nanodiscs to the surface quicker than if light water were used.

The trough was filled with a pH 7.4 20mM tris buffer with 100mM NaCl. The surface were cleaned and the pressure sensor zeroed as described in chapter 3.4. Then a solution of DODAB in chloroform were spread on the surface and the barriers were moved until a surface pressure of 25mN/m was achieved.

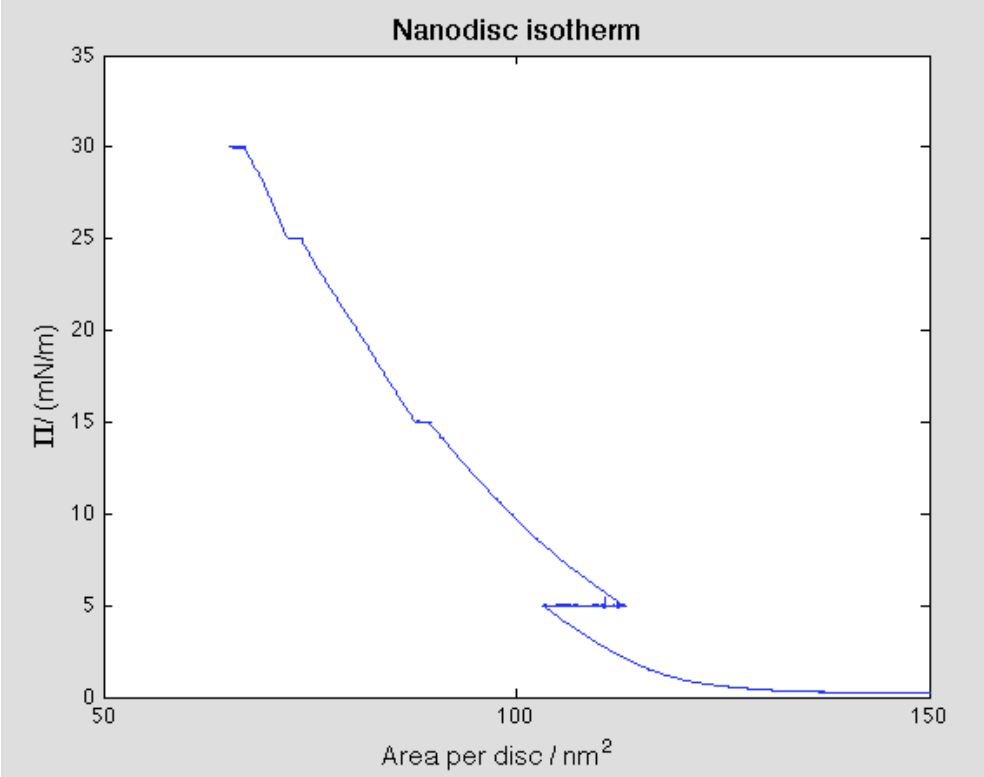

Figure 44: Example of isotherm recorded on nanodiscs while recording FCS spectra. Compression was stopped at 5, 15, 25 and 30 mN/m in order to record the spectra, during these periods the area was adjusted in order to keep a constant pressure. It is evident that discs were still moving to the surface while at 5mn/m, giving an increase in area during this time. At the next three stops the increased pressure is driving some amount of lipid and/or protein back into the solution. Whether it reforms as nanodiscs or not is unknown.

5.3 Results

Some preliminary data from collaborators at the nano-science center of Copenhagen, let to the belief that the discs, although being water soluble, formed a monolayer of intact discs (which would actually mean a bilayer in terms of lipids) on the surface of their solution. This was attempted confirmed with fluorescence correlation spectroscopy.

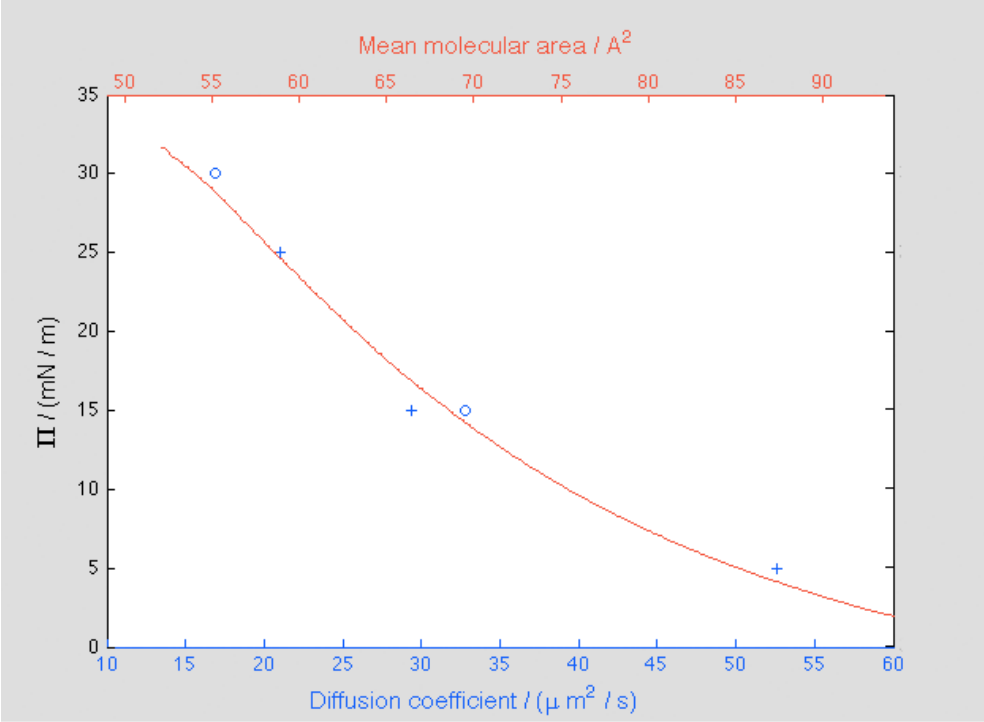

Figure 45: Three measurements of the diffusion coefficient of DMPC-rhodamine from nanodiscs at the surface of water as determined by FCS, plotted against the surface pressure **Π** (blue crosses). For reference is also given two measurements of the diffusion of pure DMPC-rhodamine / DMPC (blue circles), and the isotherm measured on pure DMPC (red line). It is evident that the MMA and the diffusion coefficient follows the same trend as predicted by the free area model, and that there is no dicernable difference between the behavior of the supposed nanodiscs and pure DMPC.

The results showed quite conclusively that the discs does not stay intact, but rather breaks up and forms a regular monolayer on the surface. In Figure 45 is shown the diffusion constants in a nanodisc layer at three different surface pressures, and a DMPC layer at two pressures, all of them found by using the minimum obtained diffusion constant in a series where the water level drops through the focal point by evaporation. The diffusion constants measured in a DMPC layer and a nanodisc layer are consistent with each other and when plotted along with the pressure-MMA isotherm for DMPC it is evident that both follow the expected trend

predicted by the free area model, namely that the diffusion constant is proportional to the MMA - 40Å^2, where the 40Å^2 is the “hard area” taken up by each lipid. One would expect a much lower diffusion coefficient for intact discs. It was therefore concluded that the discs break up when they reach the water surface, and wheter the proteins aggregate, stay in the subphase or dissolves into the formed DMPC monolayer, they do not appreciably alter it. In light of this conclusion the subject of nanodiscs were dropped for a long time.

Later new data from the nano-science centershowed that if a monolayer of the positively charged surfactant di-oleoyl-dimethyl-amoinum bromide (DODAB) was first spread on a Langmuir trough, and nanodiscs made negatively charged by DMPG was then injected into the subphase, then the discs would adsorb underneath the monolayer due to electrostatic attraction. This was conclusively

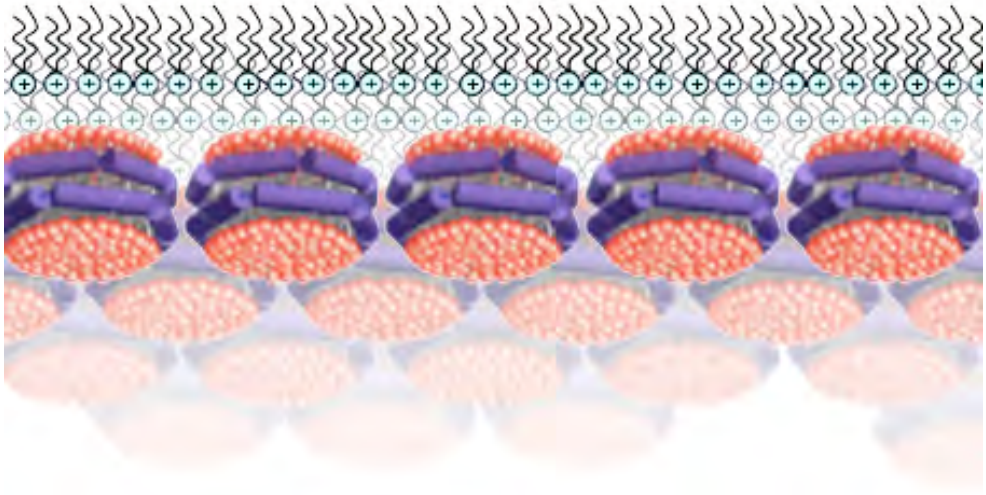

Figure 46: Schematic representation of the assumed model. A positively charged DODAB layer attracts the negatively charged nanodiscs, floating in the bulk, so they self-assemble into a monolayer of discs. Modified from art taken from www.m-cntc.illinois.edu/

shown by neutron reflectivity, which indicated the formation of a bilayer of phospholipids beneath the surface with a coverage of about 65% as reported in (Wadsäter et al. 2011). To further confirm that this was indeed a monolayer of discs attracted to the positive DODAB layer two colour FCS was attempted. Unfortunately several unforeseen problems were encountered. In order to use the high numerical aperture objective it is necessary to have only a very thin water film covering the glass above the objective (see chapter 2.8.2 and 3.3). This meant that the discs had to be added in the side of the trough where the water was deeper, away from the raised glass window. This in turn meant that the discs had a long way to diffuse before they would enter the measurement region. Several centimeters of this was across the thin ~100µm water film where convection was heavily suppressed.

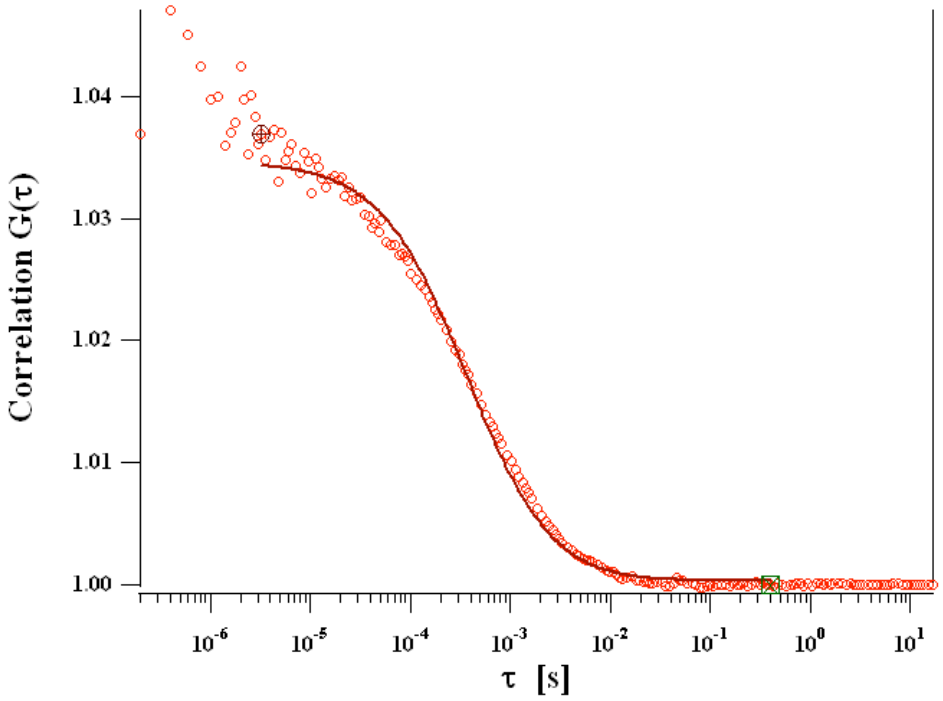

Figure 47: Correlation spectrum of nanodiscs in bulk solution. Red circles are the measured autocorrelation function, the bordaux line in the theoretical fit of a diffusion time of 294 µs, corresponding to a diffusion constant of 48µm²/s. This gives a Stokes radius of 4.5nm, well consistent with the known size of the discs. The fit is not perfect, the drop off is slower than the theoretical expectation, indicating that the discs are not completely monodisperse.

Some of the lipid from the discs always enters the DODAB layer as desribed in (Wadsäter et al. 2011). This meant that some of the lipid fluorophore also entered the monolayer. This interfered with the measurement of the nanodisc diffusion. At the surface pressure used this mixed monolayer is very inhomogenous with small domains. This gives a huge contribution to the autocorrelation function at large time lags, which interferes with the fitting of nanodisc diffusion to the data.

Diffusion in monolayers are actually slower than bulk nanodisc diffusion therefore fluorophores in the monolayer might not be expected to show up in the field of view before the nanodiscs has had time to diffuse through the 100µm thick subphase layer. However, the incorporation of lipids from the nanodiscs into the monolayer changes the local surface pressure, an imbalance in surface pressure across the layer is able to push it along the surface in ordered motion at quite high speeds. This explains why nanodisc signal was completely drowned out by the monolayer.

Some correlation spectra were recorded on nanodiscs in bulk solution, see Figure 47. They were found to have a singular diffusion constant of about 294µs giving a hydrodynamic radius of 4.5nm. The fact that only a single diffusion constant was

detected shows that the discs are relatively monodisperse, and the calculated size corresponds well to the expected size of the discs, showing that they are intact discs in bulk solution.

5.4 Outlook

The neutron reflectometry data of (Wadsäter et al. 2011) show pretty conclusively that the negative discs does indeed assemble in intact form under a DODAB layer. It should definitely be possible to extract more information about the organization and diffusion of these discs by FCS if the problem of the too thin water film can be overcome. A possible way would be to start out with the water level a few millimeters higher, inject the nanodiscs above the coverglass, and then immediately remove water from the side in order to lower the level down to where measurements can be begun. This approach is also foreseen to present some problems. Removing exactly the right amount of water quickly will require a great deal of skill and experience with the trough, but then it should be possible. Alternatively it would be possible on an entirely new and more advanced setup where water level could be automatically assessed and controlled. Changing the water level also changes the updraft on the tension probe, which would preclude following the increase in surface pressure accompanying the adsorption of the discs - again unless it could be automatically corrected.

Nevertheless adding discs, then lowering the water level would have been the next attempt at this project, if time had allowed it.

6 Stretching of DPPC and DSPC vesicles

6.1 Introduction

Vesicles of DPPC and DSPC were stretched in an optical stretcher at Cambridge University in order to examine the elasticity of lipid bilayers as a function of temperature. The stretcher employed was build and maintained by members of the Guck research group led by Jochen Guck at Cavendish Laboratory in Cambridge. It had two infrared lasers one at 1064nm and one at 1480nm, each individually dimmable and each split into two beams by a 50/50 beamsplitter and then coupled into optic fibers terminating at each side of a microfluidic chamber. Water is very transparent in the visual spectrum with only a very weak absorption in the red end accounting for the blue color of deep bodies of water. In the infrared this absorption gradually increases in strength with increasing wavelength. This means that, at the high powers employed in the optical stretcher, up to three watts, the 1064nm laser is sufficiently absorbed to cause significant heating of the water bearing the vesicles. 1064nm was chosen as a compromise when the stretcher was build, because it is made for use on living cells, visible light at high intensities are

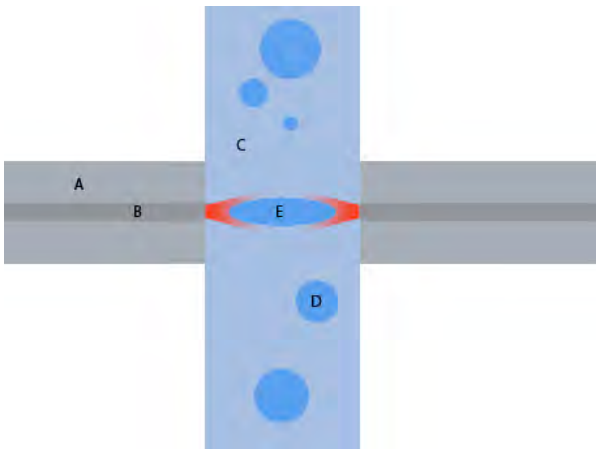

Figure 48: Close up of test chamber a seen in the microscope. A: optical fiber. B: fiber core. C: Microcapillary containing glucose buffer solution. D: vesicles containing sucrose solution. E: Vesicle trapped and stretched by laser beams emanating from the fiber cores.

much more harmful to cells than infrared. 1064nm causes manageable heating while being gentle to the cells. The 1480nm line was added to enable this study of temperature effects. It is absorbed much more strongly and therefore causes much more heating at lower power. Varying the relative powers of the two lasers enabled a wide variety of temperatures at the same stretching power.

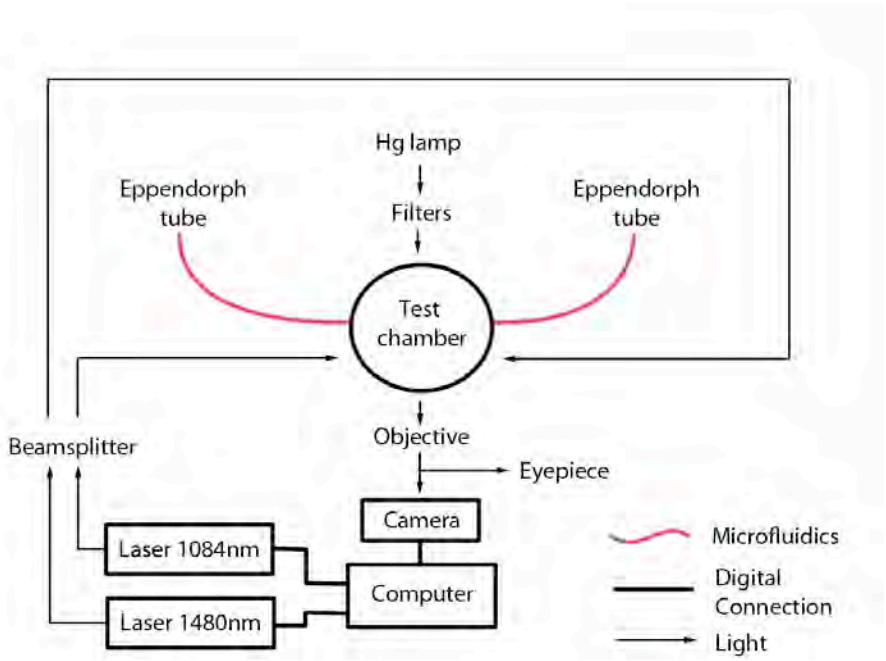

Figure 49: Schematic overview of the stretcher setup. Sample solution flows through microfluidic tubes from one Eppendorph tube to another, through the test chamber. Light from an Hg lamp passes vertically through the chamber to an objective. Various interchangeable filters allow for either fluorescent or phase contrast imaging. The image formed by the objective could then be projected either to an eyepiece or a digital camera, or split between them. Two lasers were controlled electronically. Both lasers were split 50/50 into two identical optical fibers. The laser light propagates entirely enclosed in optical fibers until it enters the test chamber. The test chamber itself consists of a horizontal glass micro capillary with a square cross section. The two optical fibers are aligned with each other on each side of the capillary and perpendicular to it. As mentioned imaging and illumination is done from above and below. A close up of the testchamber is described in Figure 48.

The test chamber consisted of a square cross section glass capillary going between the fiber ends, all in a horizontal plane (see Figure 48). Each end of the capillary was connected to plastic tubes each one ending in an eppendorph tube, one with the vesicle containing solution, the other with a matching buffer. Vesicles were allowed to flow slowly trough a capillary between the fibers. The flow was controlled by gravity. Each eppendorph tube stood on a movable platform so that their relative height could be adjusted for optimal flow rate.

The test chamber was positioned in a commercial microscope with an objective above and a light source underneath. The microscope was capable of several illumination and imaging modes. Among which phase contrast and fluorescent imaging, and the light could be diverted to either eyepieces, a camera or split between them. See Figure 49 for a principle diagram of the setup.

The vesicles used were made to contain a sucrose solution while the surrounding soltution was glucose. This allowed for similar osmotic pressures while still having different refractive indices. Bovine serum albumin (BSA) was added to both solutions in order to reduce sticking of the vesicles to the capillary walls.

6.2 Theory

6.2.1 Optical trapping

The optical strecher is a relatively novel tool, first presented by J. Guck in 2002 (Guck et al. 2002). Optical trapping has been known for a long time. Originally it was pioneered by A. Ashkin who reported manipulation of small objects with radiation pressure in 1970 and achieved the first stable optical trapping the year after (Ashkin 1970, Ashkin & Dziedzic 1971) and eventually developped the single beam optical tweezer in 1986 (Ashkin et al. 1986). When a refractive object is placed in a light beam it will feel a force due to its deflection of the light. Generally the force is separated into two parts, the gradient force and the scattering force. The scattering force is in the direction of the propagating light, and is easy to understand. Any light hitting the object and being scattered in another direction will leave behind some of its momentum. The gradient force is a second force towards regions of high intensity. It can be a bit harder to understand. It is generally calculated in one of two regimes, the ray optics regime when the wavelenght of the light is much smaller than the dimensions of the particle and is therefore ignored, and the field regime when the opposite is the case and the light is simply treated as a quasi-static field. In the ray optics regime the gradient force arises from the fact that rays of light which enters a spherical object off center and refracts will bend around the center picking up momentum along the line from the ray to the center, with the result that the center is dragged towards the ray. Different parts of the ray will compete, with the result that the object is being dragged towards the place with highes intensity. In the field regime it is straight forward that an object with higher permittivity and permeability (and therefore higher refractive index) will be pulled towards regions of strong fields. In most practical applications of optical trapping the trapped object has a size comparable to the wavelenght of the light, meaning that neighter of these regimes are really applicable. This complicates a quantitative theoretical description, nevertheless the qualitative behaviour is usually unchanged.

In order to achieve a stable trapping it is necessary to counteract the scattering force in some way. The most versatile and commonly used is to focus a laser through a high NA objective. This way the focal point of high intensity is very localized in all three dimensions and the gradient force can be big enough to overcome the scattering force. Another way is to have an external force counter the scattering force. If for example the object is heavier than the surrounding medium, then gravity will apply a constant downwards force on it. A localized parallel beam

propagating upwards along a vertical axis will trap the object stably in the horizontal plane by the gradient force, while the scattering force can be countered by gravity. Add a slight spread of the beam, or attentuation due to absorption in the medium, and the trapping will be stable along the vertical axis too.

In the optical stretcher the refractive object is placed between two non-focused laser beams like in the gravity stabilized trap, with the second laser replacing gravity. There will be a stable trapping point at with the forces from the lasers cancel out, and where any deviation from this point will lead to a restoring force, and it is no longer dependent on a particular orientation.

6.2.2 Optical Stretching

As the name implies the optical stretcher not only traps objects but also stretches them. Until now we have only considered the net forces on the trapped object. By definition the net forces cancel at the stable trapping point. There is, however, also some surface forces, which cancel, but act on different parts of the object, and if the object is pliable then this will lead to a deformation. Light that enters a medium of high refractive index apply a backwards force on the boundary. This is explained by the fact that the speed of the light is reduced in the medium, but since its frequency and therefore its energy remains the same its momentum has to be increased by a factor n1/n2; this extra momentum is taken from the medium it enters. As light leaves the medium the exces momentum is left behind, giving rise to a forwards force. In both cases these forces are pointing outwards from the medium of high index to the medium of low index. As both lasers shine along the same axis, the object experiences a deforming force stretching it along this axis (see Figure 50).

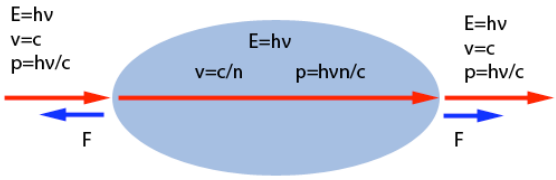

Figure 50: Light that enters a medium of refractive index n_2 from a medium with index n_1 will grab an extra $E\cdot(n_2-n_1)/c$ momentum from the medium. When it exits on the other side it leaves this momentum behind again meaning that the net force on the object cancels. Internally the force is still able do affect the object.

The magnitude of this force can be trivially calculated to be:

$$F = \frac{P(n_1 - n_2)}{c} \qquad \text{Eq. 6.1}$$

where P is the light power entering the object, n_1 and n_2 are the respective refractive indices and c is the speed of light. Since all the light works to deform the object,

while only a small part is scattered, the deformation force can be very large compared to the scattering force (Guck et al. 2001).

With a refractive index of the object n_2=1.382 corresponding to a 1M sucrose solution, and a surounding medium index of n_1=1.354 (1M glucose), the Fresnel equations predict a reflectivity of (assuming a right angle of incidence):

$$R = \left(\frac{n_2 - n_1}{n_2 + n_1} \right)^2 \approx 0.01\% \qquad \text{Eq. 6.2}$$

At 1W of power the total scattering force from the reflection at both ends of the object is therefore:

$$F_{total} = 2 \cdot \frac{R \cdot P \cdot n_1}{c} = \frac{2 \cdot 10^{-4} \cdot 1W \cdot 1.354}{3 \cdot 10^8 \frac{m}{s}} = 0.9pN \qquad \text{Eq. 6.3}$$

In comparison the individual faces of the object feels a force on the order of

$$F = \frac{P(n_2 - n_1)}{c} = \frac{1W \cdot 0.028}{3 \cdot 10^8 \frac{m}{s}} = 93pN \qquad \text{Eq. 6.4}$$

Among the discoveries made with the optical stretcher is the fact that cancer cells tend to be more pliable (deform easier) than regular cells. This property is now being developped as a way to screen patients for cancer (Remmerbach et al. 2009).

6.3 Materials and methods

6.3.1 Preparation of vesicles for stretching

Two slides of ITO covered glass was washed thoroughly and then a solution of lipid (DPPC, DSPC) in chloroform was added applied to the central area of the conductive side of both slides. The chloroform was allowed to evaporate and the slides was desicated for an hour to ensure no chloroform remains in the lipid. An edge spacer of teflon film was applied on three of four sides of the lipid on one of the slides and the other slide was put on top. The two slides were kept in this position by two clamps, then cell was filled with a 1M solution of sucrose with 0.02% BSA and sealed of with laboratory wax.

The cell was put in an oven heated to some way above the transition temperature of the lipid in question (50-60C for DPPC and 70-80C for DSPC), and allowed to thermalize. Then an alternating voltage of about 3V at 10Hz was applied across the cell for about an hour. Finally the cell was split open and the vesicle solution was diluted in 1M glucose solution with 0.02% BSA and was ready to use.

6.3.2 Preparation of the strecher.

The microfluidic system was rinsed by forcefully pushing a 70% ethanol solution trough the system in both directions using a syring Then the same was done with the 1M glucose + BSA solution without vesicles. The setup was then allowed to stand for at least 30min to allow the BSA to adsorb on the walls of the test chamber capillary. After this the vesicle solution pushed into the system by syringe in a slower pace to avoid unnecessary disruption of the vesicles. After filling the entire system with vesicle solution the laser, mercury lamp and camera was turned on, and experiments begun.

6.3.3 Experiments

The capillary was watched for suitable vesicles for experiments. Vesicles were selected for being solitary, round and not too small. When a suitable vesicle drifted into view the trap was turned on at minimum power giving fairly stable trapping, typically 300mW, and the flow was stopped. The output from the camera was then recorded as video while the laser was turned up to a certain stretching power typically for two seconds and then relaxed back to normal trapping power. This was then repeated for as long as the vesicle would survive. Occasionally trapped vesicles lysed, usually when subjected to high stretching powers and high heating. When a vesicle lysed the sucrose solution would rapidly diffuse out. This would result in a loss of refractive contrast, at the same time rendering it neigh invisible and unaffected by the trap. When that happened the procedure was repeated with another vesicle.

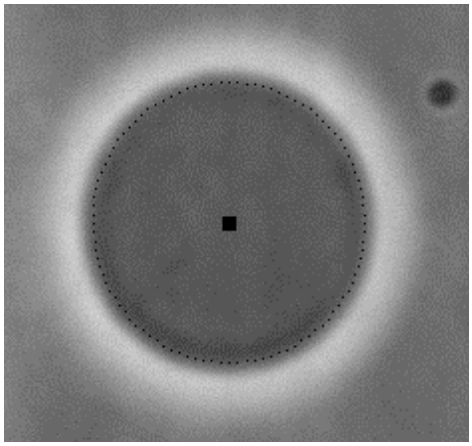

Figure 51: Example of image output from the image analysis script. The big black square marks the vesicle centre and the small ones the hundred found edge points.

A few times vesicles were prepared with a small amount of fluorescently labeled lipids in order to enable visualization of lysed vesicles, lose pieces of membrane and other aggregations of lipid not visible in phase contrast imaging.

6.3.4 *Image analysis.*

A short matlab script was written to analyze the images of the vesicles from the strecher and quantify the deformations. The script worked by loading the first frame of a video and asking for a manual assesment of the position of the center of the trapped vesicle. It then analyzed the intensity profile of the image in a hundred lines radiating outwards from this center, looking for the edge of the vesicle. As the phase contrast imaging produces images where the interior of the vesicles appear dark compared to the background ilumination and the edges light with a relatively sharp transition from dark to light, the script was made to look for a sharp increase

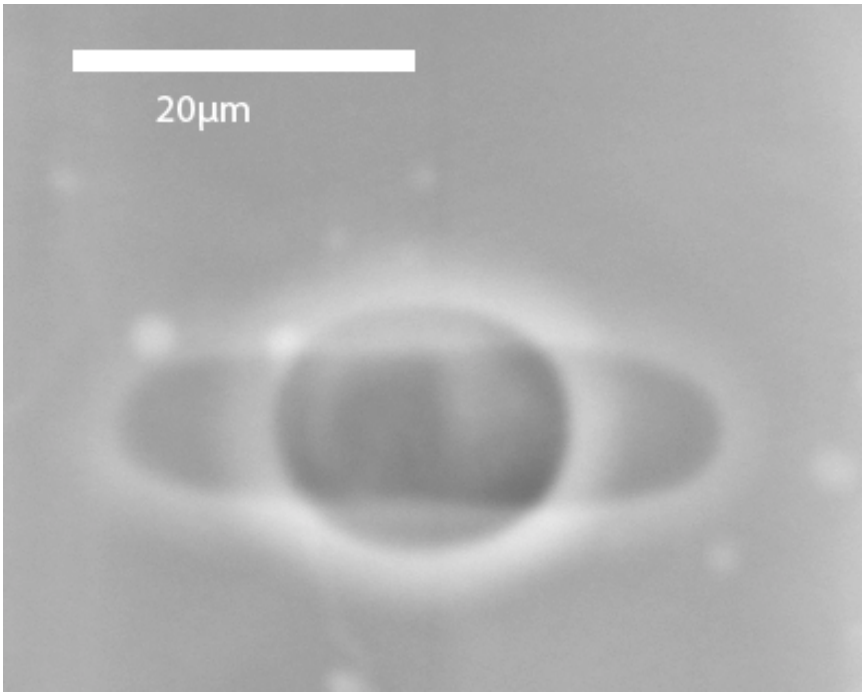

in Figure 52: Single frame showing two overlayed shapes of the same vesicle, demonstrating that shapechange can be very rapid.

intensity. For speed this was coded as simply the point at which the brightness increase from pixel n to pixel n+3 was the largest. As an addition the script was made to weigh edges close the the radius of the previously found edge more favorably. This reduced the risk of brigthness variations far from the vesicle being interpreted as the vesicle edge, although at the exepense of a computationally expensive divison in the innermost loop of the script.

After a hundred such points was found at evenly spaced angles from the defined center, the points were fitted with an ellipsoid with vertical axis a and horizontal axis b. It should be noted that this procedure will only recongnice strethcing and

compression along the optical axis of the lasers and the perpendicular, a stretching tilted 45 degrees to the axis would be invisible with this scheme.

Occasionally the script failed to properly determine the dimensions of the vesicle, especially when a tempoary imbalance in the stretcher caused the trapped vesicle to move close to one side of the microfluidic chamber. This allowed the bright edge of

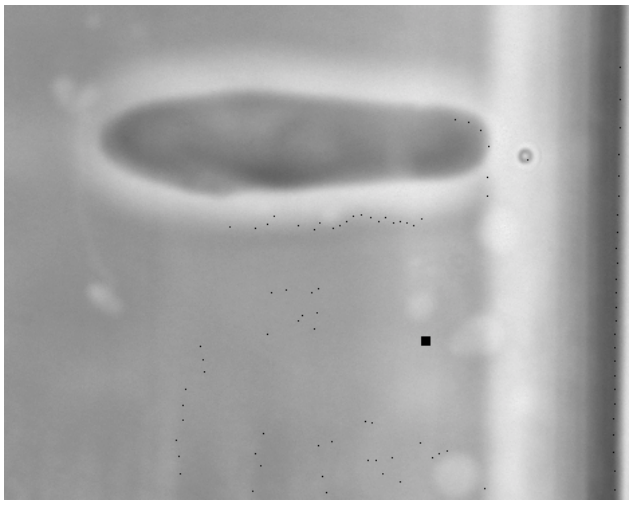

Figure 53: Example of the image recognition failing. The square marking the determined center of the vesicle is clearly not inside the vesicle, and the edges found (black dots) are scattered around the image. Whenever an image like this was encountered the data from that clip was discarded.

the chamber to interfere with the image recognition. Once the assumed center moved outside the vesicle the algorithm was unlikely to re-find it, producing nonsense data for the remainder of the clip. Therefore the script was made to save every tenth frame as an image with black dots indicating the found edge as well as the center of the vesicle (see Figure 53, Figure 51). The resulting ca. 6000 images was manually controlled and the data from videoclips in which the script had failed were discarded.

6.4 Results

Pure lipid vesicles appear to be almost perfectly rigid below their main transition. Above the transition they become very soft, and shape change occurs virtually instantly, although the phase change may take some hundred milliseconds. Figure 52 shows a videoframe captured at the instant of aplication of the stretching of an already melted vesicle. It shows an image of the vesicle stretched and unstretched superimposed on each other but no blur from intermediate shapes are apparent. This means that the shapechange took place over a time scale much less than the exposure time of the frame that is about 100ms.

Figure 54 shows an overview of the results of several hundred stretches of DPPC and DSPC vesicles. One thing is immediately apparent, deformations are minimal to nonexistant when the two lasers powers are beneath a threshold line. That is, when the vesicles are too cool to have gone through the main transition. These threshold lines allow for a callibration of the heating effects of each laser. It is evident that the power required to melt DSPC vesicles are somewhat higher than what is needed to melt DPPC vesicles, as would be expected. However the power is not much higher when compared to the relative melting points of these lipids.

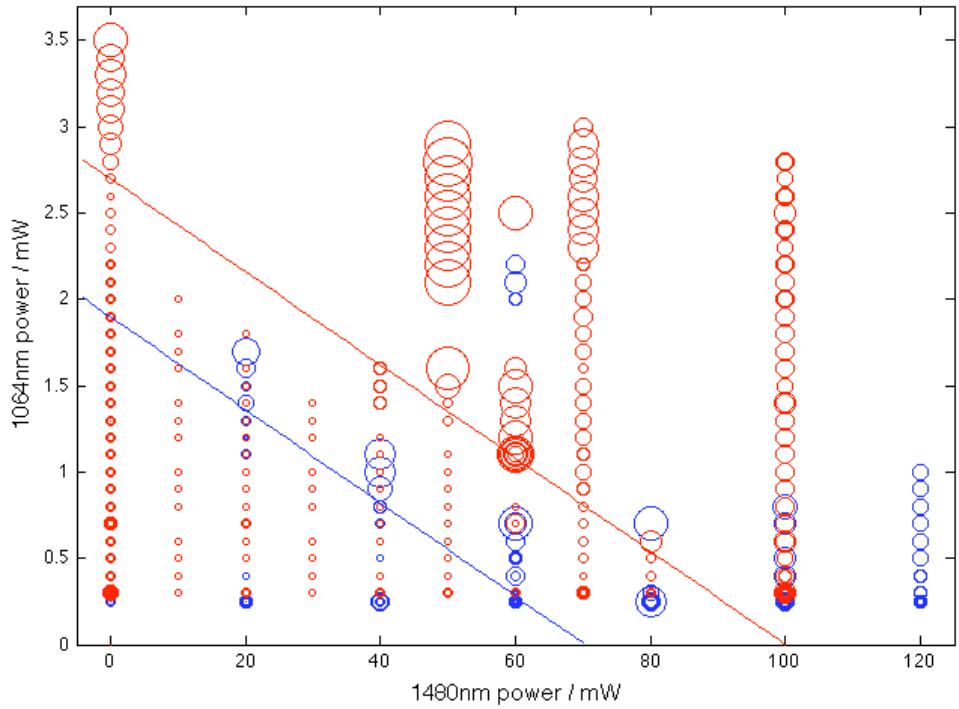

Figure 54: The results from several hundred vesicle stretches. Each circle represents one experiment, with the size of the circle indicating how elongated the vesicle was, bigger circle meaning more deformation; the position of the circles along the x and y axes indicate the power of the 1480nm and the 1064nm laser, respectively. Blue circles represent experiments on DPPC vesicles, red circles DSPC vesicles. Deformation seems to increase dramatically above the two plotted lines, showing that the lipids melt when higher powers are applied.

The expected deformation of a vesicles as its membrane melts can be calculated. It is assumed that the volume does not change, while the area of membrane increases by 25%. If the deformed vesicle to a good approximation is a prolate spheroid then the expected relation between its big and small axis can be calculated as follows. The surface area of a prolate spheroid with great axis c and minor axis a, is:

$$S = 2\pi a^2 \left(1 + \frac{c}{a\sqrt{1-\left(\frac{a}{c}\right)^2}} Sin^{-1}\sqrt{1-\left(\frac{a}{c}\right)^2} \right)$$ Eq. 6.5

this area is expected to be about 25% bigger than the surface area of the former sperical vesicle of radius r:

$$S = 1.25 \cdot 4\pi r^2$$ Eq. 6.6

At the same time the volume inside the vesicle remains constant. The volume of the ellipsoid is:

$$V = \tfrac{4}{3}\pi a^2 c = \tfrac{4}{3}\pi r^3$$ Eq. 6.7

The above equations can be solved nummerically for a and c. With the following results:

$$c = 3.7a = 2.4r$$ Eq. 6.8

This seems to agree pretty well with what is seen in many cases.

Below the transition no vesicle deformation is visible to the naked eye, however the image recognition script does pick up a slight deformation. To quantify this deformation the best four stretch series below the transition was picked out. In particular the ones wich seemed to be without other interfering vesicles or other pieces of membrane around. These were the DSPC series at a 1480nm power of 10mW, 30mW, 50mW and 70mW, respectively. Since the deformation was right at the detection limit of the camera and script, and since the vesicles changed a bit over time, it was necessary to normalize the deformation observed. This was done by averaging the big axis/small axis ratio for the duration of the two second strech, and then dividing by the same ratio averaged over the preceding two seconds, (during which the 1064nm power was 0.3W, the minuímum for stable trapping). Finally one was subtracted so that zero corresponds to no deformation:

$$D = \frac{\left\langle \frac{c}{a} \right\rangle_{Stretch}}{\left\langle \frac{c}{a} \right\rangle_{Bef\,ore}} - 1$$ Eq. 6.9

Then this D was plotted as function of the applied power (see Figure 55). Although the noise is high the deformation was found to be approximately proportional to the applied 1064nm power, with the regression crossing zero at a power of 0.3W as expected due to the normalization. Curiously the the slope of the regressions seems to increase dramatically with higher 1480nm power applied.

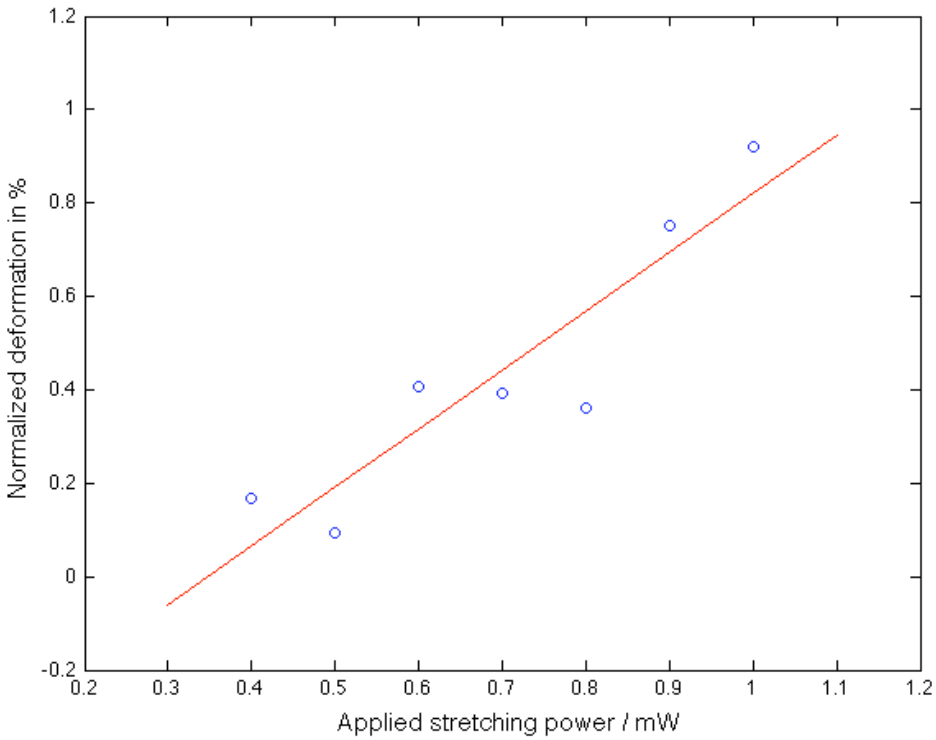

Figure 55: Blue circles: Deformation of DSPC vesicles as function of applied 1064nm laser power. Deformation is normalized by dividing the ratio of the average axis lengths during the two-second stretch by the ratio of the average axis lengths in the preceding two seconds (power 300mW), then subtracting one. For elaboration see text. Red line: Linear regression to the experimental data. Due to the normalization it is expected to cross the point (0.3W,0) which is very nearly the case.

Figure 56 shows the slope of regression from the four dataseries discussed above, plotted against the power of the 1480nm laser with a logarithmic y-axis. When plotted in this way the datapoints form a nearly straight line, leading to the emiprical conclusion that the pliability of the vesicles increases exponentially with the applied 1480nm power as shown in eq. 6.10.

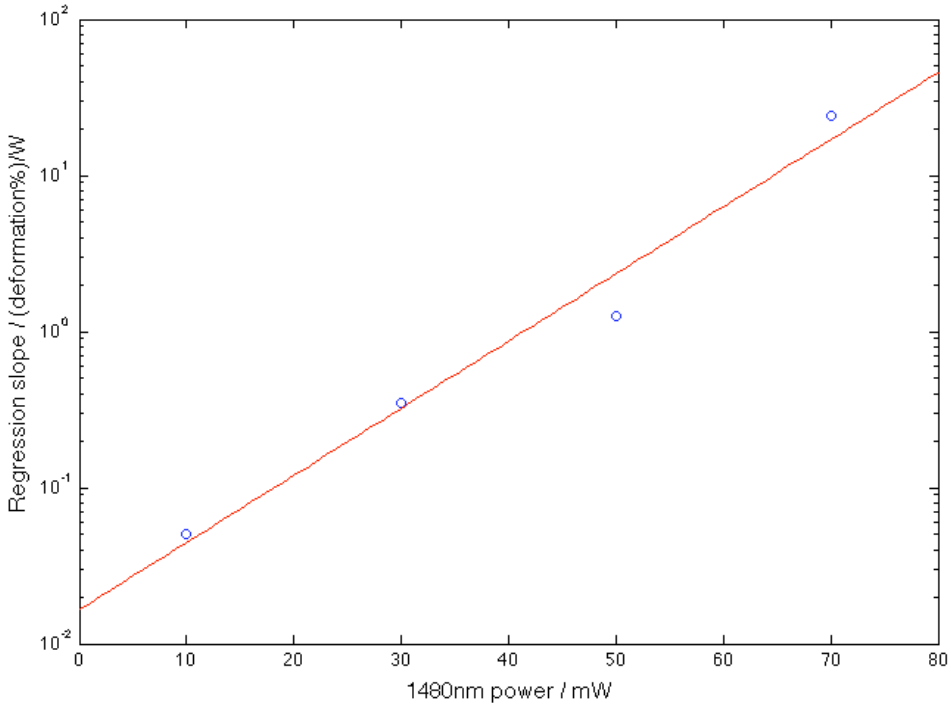

Figure 56: Plot of the results from four stretching series below the membrane melting point. Slope the regression obtained as in Figure 55 plotted as function of the 1480nm power used during the series.

6.4.1 All-or-nothing loss of contrast

The vesicles were prone to lysing when the phase transition were crossed. This is no surprise since it is well known that the permeability of lipid membranes increase dramatically in the phase transition when fluctuations becomes large. Blicher showed that the timescale for leaking of rhodamine 6G out of DPPC vesicles changed from weeks to seconds when going through the transition (Blicher et al. 2009). However one would expect to see a gradual loss of contrast as the sucrose leaked out if the permeability was high. This was not observed. Rather, when the temperature was moved through the transition regime, a vesicle would either survive with no dicernable loss of contrast, or it would very rapidly disappear completely. When observed using flourescence the vesicle was still intact, but invisible in phase contrast imaging, and no longer responding to the trap. The likely reason for the sudden breaking is that a spontaneous pore formed becomes unstable if it becomes big enough. A hole in a membrane will cost an amount of energy proportional to its circumference because of linetension around the hole. If the membrane is under tension then a hole also liberates an amount of energy proportional to its area. This means there will be a size at which the energy falls with size, the hole will therefore grow without bound, until the sucrose have leaked out. In the absence of a refractive index contrast the force on the membrane is removed and line tension are allowed to reclose the hole.

6.5 Discussion

Experiments with fluorophores show that vesicles that looks nice and spherical in phase contrast microscopy, often are not. shows a lot of lose membrane flapping around the vesicle as well as a second vesicle inside, neither of these features were visible in phase contrast. shows a vesicle inscribed with two further vesicles. This may mean that the deformation seen in phase contrast is less telling of the deformability of the membrane than previously thought, as loose membrane might insert to increase the area when streched, or multiple layers may give a higher stifness than a single membrane layer would.

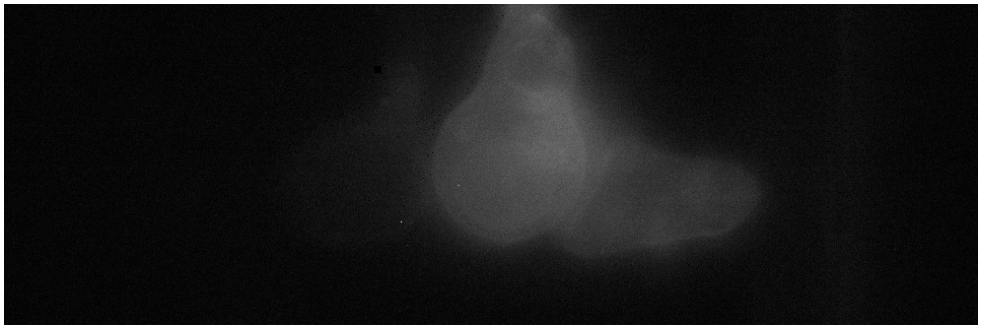

Figure 57: Fluorescence photograph showing lose sheets of membrane / deflated vesicles flapping around what looked like an isolated spherical vesicle in phase contrast.

As with any technique, which generates large amounts of data interspersed with many artifacts and faulty measurements that require weeding; extreme care is needed to avoid confirmation bias. By selecting only the “good” vesicles it would be possible to produce almost any result. A lot of the vesicles does seem to confirm the expected area increase of the membrane of 25%, but just as many do not.

If the data from the stretching below the melting point is to be trusted then the deformation follows an empirical law like:

$$D = 0.00017W^{-1} \cdot y \cdot \exp\left(\frac{x}{10mW}\right) \qquad \text{Eq. 6.10}$$

where y is the power of the 1064nm laser and x is the power of the 1480nm laser. If time had permitted it more experiments should have been done to confirm whether such a law really exist or whether I am seeing patterns in random noise. A good idea would be to vary both lasers at once in such a way as to keep the temperature constant (as determined by Figure 54) using the same vesicle.

No theoretical explanation for the law of eq. 6.10 is available at the moment.

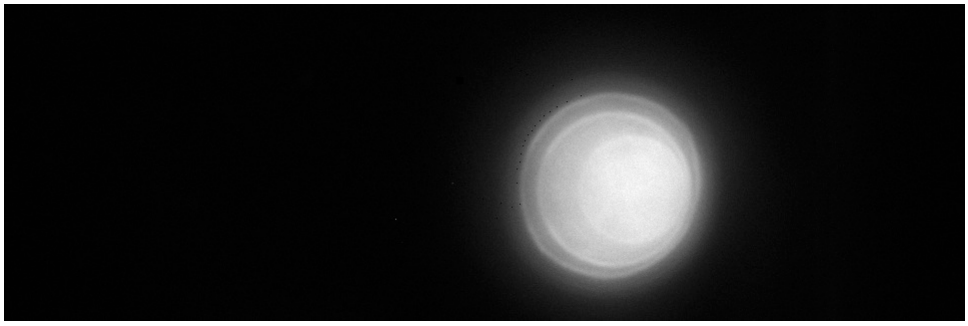

Figure 58: Fluorescence photograph showing several inscribed vesicles even though phase contrast showed only one.

7 Direct deposition patterning

Nanopatterning is a very important field. Regular microscopic patterns are used for everything from electronics and microfluidics (Menz *et al.* 2001) to structuring arrays of nanoscopic bio reactors (Stamou *et al*. 2003). When only a small area need to be structured, but the accuracy and degree of control needs to be very high, top-down methods are generally preferred. In other cases it is necessary with large amounts of relatively structured material to be prepared quickly and cheaply. In these cases it s usually necessary to turn to self-assembly.

It was found that when a solution of DPPC in hexane/ethanol was deposited on a freshly cleaved mica substrate, it spontaneously formed a very regular stripe pattern, which could be subsequently observed with atomic force microscopy (AFM). The patters were approximately 700nm wide. The pattern was highly reproducible, was formed within a minute of deposition, and was extremely stable too, showing no degradation in the course of several weeks at room temperature exposed to ambient oxygen and moisture. Figure 59 show such an AFM image along with a Fourier transform demonstrating the regularity of the pattern. Figure 60 shows a line profile demonstrating that the height of the stripes in constant and almost exactly 5nm, consistent with the thickness of a bilayer. Figure 61 shows a larger picture of another sample with a similar highly regular stripe pattern and also shows a highly complex structure formed another place on the mica. In Figure 62 is shown a zoom out from the first picture in Figure 61 covering a very large area of 90µm by 90µm with almost no defects

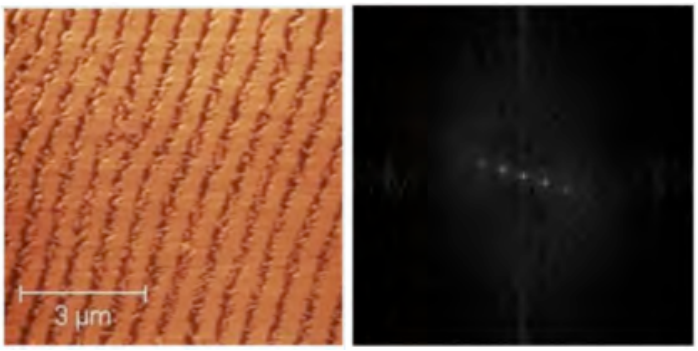

Figure 59: Left: AFM picture of self assembled DPPC stripes from a hexane/ethanol solution on mica. Right: Fourier transform of the picture to the left.

It is tempting to attribute this pattern to electrostatics like the stripe phase of monolayers, or alternatively that the pattern forms as the solvent evaporates, leading to a shrinking of the deposited material, akin to the hexagonal patterning often observed in dried mud. However we do not believe either of these to be the case.

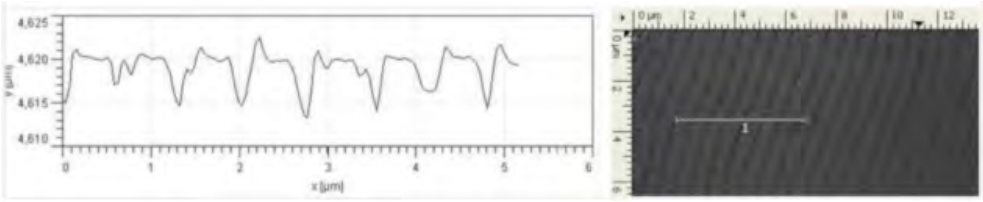

Figure 60: Line profile across the stripe pattern. The dips between the stripes are almost exactly five nanometers, consistent with the thickness of a bilayer.

It has been known since the 90's that lipids can be deposited in regular self-assembled stripes using the Langmuir-Blodgett technique. Simulations have shown that such patterns form because of an instability along the receding three phase boundary between the air, water and substrate as the substrate is being pulled out of the water during the transfer procedure (Li *et al.* 2012).

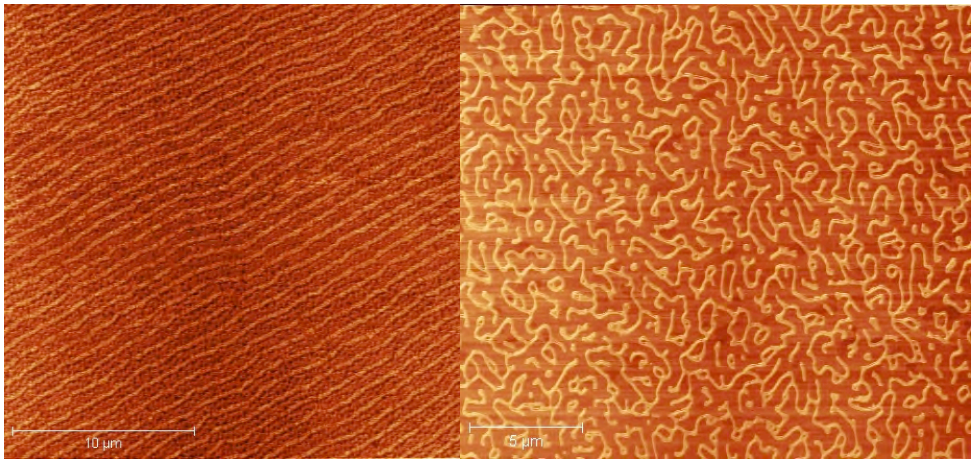

Figure 61: AFM pictures of DPPC on mica, deposited directly from a solution of 90% hexane / 10% ethanol. Left: The stripe pattern covering most of the surface of the mica. Right: Example of more complicated structure found in other rare places.

We theorize that a similar thing happens as the hexane/ethanol evaporates from the surface of the mica. Because the organic solution is more volatile than water the speeds of the receding solvent front is much higher than when water evaporate; comparable to the speeds used when making stripes by the Langmuir-Blodgett technique.

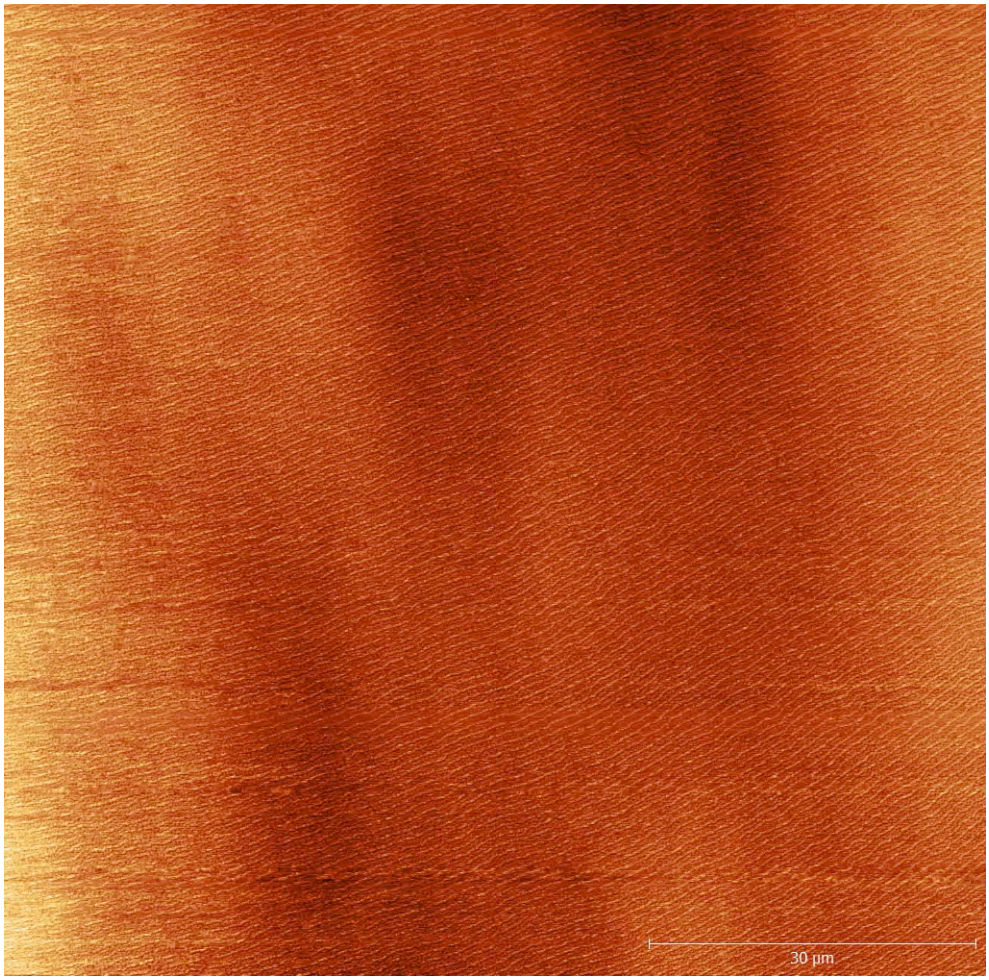

Figure 62: 90µm by 90µm AFM scan, showing that the stripe pattern covers huge areas with surprisingly few defects.

The exact mechanism of formation is hard to ascertain. It is likely that a Gibbs monolayer will form at the mica/hexane interface given the micas polar nature. One might then assume that a second monolayer is deposited on top when the solvent retreats in a mechanism similar to a Langmuir-Blodgett transfer. However, this would presuppose a monolayer of lipids at the hexane/air interface with the headgroups in air, this is not likely to happen since the dielectric constant of air is close to one, even lower than the 2-4 of an organic solvent, therefore the headgroups are even less stable in the air than in the hexane. Rather the second (and possibly more) monolayer has to be deposited directly from solution. The ethanol content in the solvent may also play a significant role. It was not possible to study this phenomenon without ethanol since DPPC is poorly soluble in pure hexane. Figure 63 sums up the proposed mechanism.

The amount of lipid in the solution is enough for many monolayers covering the mica surface, but spreading a thinner solution did not result in this pattern. This is more evidence that the deposition happens directly from solution and requires a certain concentration before it happens. The flatness of the samples suggests that only a few monolayers covers the mica, the rest of the material is presumably concentrated at very localized places from where the last concentrated solution evaporates.

Many studies remain to be done on these systems, both to determine the mechanism of the deposition and whether it applies to other solvents and other lipids; and to see whether the pattern can remain stable under water and whether proteins can be incorporated into it for further utilization.

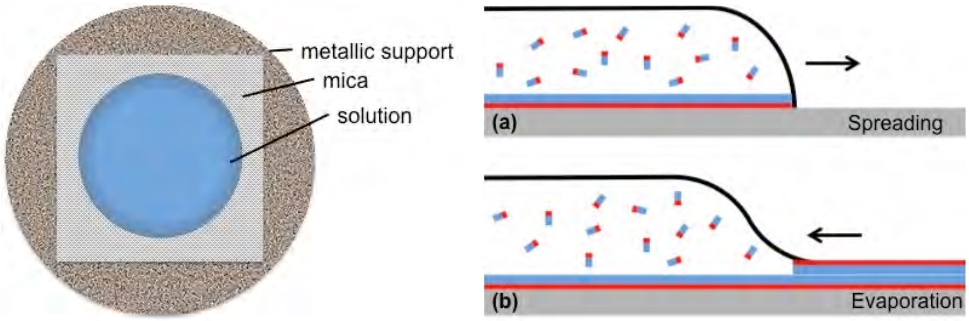

Figure 63: Proposed mechanism of deposition of the supposed bilayer making up the stripe pattern.

8 Summary and outlook

In this study many aspects of the organization of phospholipids have been investigated.

Many different techniques for evaluating the line tension, and dipole moment of lipid monolayers have been tested and discussed, including:

- The width of domain strips in balance between line tension and electrostatic repulsion (both).
- Domain size distribution (both).
- Dynamic dragging of domain by line tension (line tension).
- Electrostatic attraction of domains (dipole moment).
- Kelvin probe (dipole moment).

Further the assumptions of the frictious forces in the subphase used in the line tension dragging and the electrostatic dragging experiments were tested by examining the diffusion of small domains by individual tracking.

The recorded pictures show the extremely complicated morphology that can arise due to the high line tension and dipole moment density differences of pure lipid monolayers in the fluid-gas coexistence regime. Photosystem one was incorporated into a monolayer, and found to preferentially position itself on the domain boundaries, illustrating the effect that the phase behavior of lipids can have on membrane organization.

Attempts were made to force a DPPC monolayer into the phase coexistence regime using an electric field; this was, however, unsuccessful, and subsequent theoretical calculations called into doubt whether such a scheme is at all feasible.

It was conclusively disproven that nanodiscs form a Gibbs monolayer of intact discs at the air/water interface. The possibility of characterizing a Gibbs monolayer of discs beneath a Langmuir monolayer of DODAB were discussed and is promising, but presents some technical challenges which precluded its inclusion in this thesis.

Several matlab script were written which allowed automatic analysis of large amounts of data in the form of videofiles of vesicles or monolayer domains.

It was shown that one can control temperature conveniently in an optical stretcher by using different wavelengths of light and the elastic properties of membranes were examined.

A surprisingly easy and reliable way to fabricate a regular nanoscopic stripe pattern of lipids on mica was discovered. The regularity and reproducibility of this pattern formation surpasses many methods using much more complicated means. The

mechanism of this formation should be further studied and is expected to yield exiting insights into the complex behavior of solutes in an evaporating solvent. If it can be used to pattern more complex molecules it holds the potential for many applications in a wide variety of fields.

Appendix A

Matlab scripts

Script for finding edge and center of vesicles.

```
%clc
%clear
%close all

%threshold = input('Threshold ');
%number = input('Number of points ');     %Number of edgepoints to
find in each frame
number = 100;

co=cos((1:number)*2*pi/number);           %make internal sin and cos
table for speed
si=sin((1:number)*2*pi/number);

rr=50;

cd('/Volumes/Time Machine Backups/kasper/2011-02-01');

files=dir;
disp(files);

valg=f:numel(files);


%for f=valg
%    if files(f).isdir
%          cd(strcat('/Volumes/Time Machine Backups/kasper/2011-02-
01/',files(f).name));%
%        mov = aviread(strcat(files(f).name,'.avi'));          %Read
in video
%        [im1,map] = frame2im(mov(1));
%        figure(1);
%        imshow(im1);                              %show first frame
%        [xxx(f),yyy(f)] = ginput(1);
%    end
%end


for f=valg
    f
    if                        files(f).isdir                        &&
not(exist(strcat('/users/feld/documents/vesicle2/',files(f).name,'.c
sv')))
        cd(strcat('/Volumes/Time   Machine   Backups/kasper/2011-02-
01/',files(f).name));

        mov = aviread(strcat(files(f).name,'.avi'));          %Read
```

```
in video

        cd('/Users/feld/documents/vesicle2/pictures');

        %[im1,map] = frame2im(mov(1));
        %figure(1);
        %imshow(im1);                              %show first frame

        %beep;
        %[xx,yy] = ginput(1);                          %input initial
guess of center of vesicle
        xx=xxx(f);
        yy=yyy(f);
        x0= [100;0];                                 %default guess of
radius and deformation

        length=(numel(mov));                      %lenght of main loop
equal to number of frames in movie
        [heigth,width]=size(frame2im(mov(1)));
        clear def
        clear rad
        def(1:length)=0;
        rad(1:length)=0;
        data=zeros(number,length);

        for n=1:length
            [im1,map] = frame2im(mov(n));       %Load n'th frame
            x=uint16(xx);
            y=uint16(yy);                             %set center of
vesicle as x,y
            line(1:300)=0;
            avg(1:290)=0;
            xx=uint32(0);                            %reset xx,yy for
determining new center
            yy=uint32(0);
            sample=not(mod(n,10));
            for angle = 1:number
                for r = 1:300                         %get brightness
profile in a line radiating from center
                    a=uint16(y+r*si(angle));
                    b=uint16(x+r*co(angle));

line(r)=im1(max(min(a,heigth),1),max(min(b,width),1));
                end
                for r = 1:290
                    avg(r)=(sum(line((r+7):(r+10)))-
sum(line(r:(r+3))))/(4000+(r-rr)^2);        %find point of steepest
increase that is close to last edge
                    %avg(r)=line(r)+line(r+1)+line(r+2)+line(r+3);
%make four point floating average of line profile
                end
                [C,r] = max(avg);                  %edge of vesicle
defined as point of maximum brightness - found to work better than
fancy edge fittings
                rr=r;
                a=y+r*si(angle);
                b=x+r*co(angle);                          %determine
coordinates of found edge point
                if a && b && a<heigth && b<width && sample
```

```
                    im1(a,b) = 0;                    %place black dot
at found point, used for quality testing, commented out in final
version for speed
                end
                xx=xx+uint32(b);
                yy=yy+uint32(a);                                 %sum up
edgepoints to improve center position for next frame
                data(angle,n)=r;                  %store edge-center
distance as function of angle
            end
            xx=xx/number;
            yy=yy/number;                         %sum of edge point
positions divided by thier number -> new center

            if sample

                for a=yy-3:yy+3
                    for b=xx-3:xx+3
                        im1(a,b) = 0;                    %draw black
square at center of vesicle, commented out for speed.
                    end
                end
                figure(1);
                imshow(im1);

imwrite(im1,strcat(files(f).name,num2str(n),'.bmp'),'bmp');
            end

            [x,resnorm]                                                =
lsqcurvefit(@fit,x0,(1:number)*2*pi/number,data(:,n).');        %fit
data to determine radius and deformation of vesicle
            rad(n)=x(1);
            def(n)=x(2);                              %save radius and
deformation
            x0=x;                                 %make found radius
and deformation the new initial guess
        end

        %Save = fopen('Vesicle.txt');
        %fprintf(Save, def);
        %fclose(Save);

        cd('/Users/feld/documents/vesicle2');
        csvwrite(strcat(files(f).name,'.csv'),[def;rad;data],0,0);

        figure(3);
        plot(def);
    end
end
```

Script for tracking liquid domains

```
if go==2
    track = 1;

    mov = aviread('/Volumes/USB DISK/Lisamin2.avi');

    for n=1:600
        [imcell{n},map] = frame2im(mov(n));
    end

    clear mov
    imcell2=imcell;
end

if go==1
    xdata(track,:)=x;
    ydata(track,:)=y;

    track=track+1;
    imcell=imcell2;
end

go=0;

x=zeros(1,600);
y=zeros(1,600);

im=imcell{1};
figure(1);
imshow(im);                                %show first frame
[y(1),x(1)] = ginput(1);

im(uint16(x(1)-3):uint16(x(1)+3),uint16(y(1)-3):uint16(y(1)+3))=0;
imcell2{1}=im;

%x=uint8(j);
%y=uint8(k);

for n = 2:600
    im=imcell{n};

    x(n)=x(n-1);        %Initial center guess at last center
    y(n)=y(n-1);

    for t=-4:4          %Set descreasing search area size wide at
first to
                        %find domain, then narrower for accuracy
        xx=double(0);
        yy=double(0);

        for a=t-7:7-t       %find center of intensity within search
square
            for b=t-7:7-t

xx=xx+double(x(n)+a)*double(im(uint16(x(n)+a),uint16(y(n)+b)));
```

```
yy=yy+double(im(uint16(x(n)+a),uint16(y(n)+b)))*double((y(n)+b));
            end
        end

        M=sum(sum(im((x(n)-7+t):(x(n)+7-t),(y(n)-7+t):(y(n)+7-t))));

        x(n)=(xx/M);
        y(n)=(yy/M);
    end

    figure(1);
    im2=im;
    im(uint16(x(n)+7):uint16(x(n)+10),uint16(y(n)))=200;
    im(uint16(x(n)-10):uint16(x(n)-7),uint16(y(n)))=200;
    im(uint16(x(n)),uint16(y(n)+7):uint16(y(n)+10))=200;
    im(uint16(x(n)),uint16(y(n)-10):uint16(y(n)-7))=200;


    imshow(im);

    im2(uint16(x(n)-3):uint16(x(n)+3),uint16(y(n)-
3):uint16(y(n)+3))=0;
    imcell2{n}=im2;
end

go=1;
```

Script for tracking gas domains

```
if go==1                    %If previous track was succesful then
save the data
    xdata(track,:)=x;
    ydata(track,:)=y;

    track=track+1;          %new tracking number
end


if go==2                    %Initialization stuff
    track = 1;

    mov = aviread('/Volumes/USB DISK/bubblediffusion.avi');

    for n=1:600
        imcell{n} = frame2im(mov(n));   %Save movie in cell array
    end

    clear mov
    imcell2=imcell;         %make copy of movie
end

t=250;
x=zeros(1,600);
y=zeros(1,600);

number=4;                   %number of edgepoints used to determine
position of domain
```

```
go=0;                       %Set go=0 so data is not saved if script
was interupted prematurely

co=cos((1:number)*2*pi/number);         %make internal sin and cos
table for speed
si=sin((1:number)*2*pi/number);

rr=0;
im=imcell{t};
figure(1);
imshow(im);                             %show first frame
[y(t),x(t)] = ginput(1);
[a,b]=ginput(1);
radius=int16(sqrt((y(t)-a)^2+(x(t)-b)^2));
%x=uint8(j);
%y=uint8(k);
for a=y(t)-3:y(t)+3
    for b=x(t)-3:x(t)+3
        im(uint16(b),uint16(a)) = 0;              %draw black square
at center of vesicle, commented out for speed.
    end
end
imcell{t}=im;


for n = t+1:600
    im1=imcell{n};

    x(n)=x(n-1);
    y(n)=y(n-1);

            for it=1:2
            line(1:300)=0;
            avg(1:290)=0;
            xx=uint32(0);                       %reset xx,yy for
determining new center
            yy=uint32(0);

            for angle = 1:number
                for r = 1:radius+10                   %get
brightness profile in a line radiating from center
                    a=uint16(y(n)+r*si(angle));
                    b=uint16(x(n)+r*co(angle));
                    line(r)=im1(b,a);
                end
                for r = 1:radius
                    avg(r)=(sum(line((r+7):(r+10)))-
sum(line(r:(r+3))));       %find point of steepest increase that is
close to last edge
                    %avg(r)=line(r)+line(r+1)+line(r+2)+line(r+3);
%make four point floating average of line profile
                end
                [C,r] = max(avg);               %edge of vesicle
defined as point of maximum brightness/increase - found to work
better than fancy edge fittings
                r=r+5;
                a=y(n)+r*si(angle);
                b=x(n)+r*co(angle);                %determine
coordinates of found edge point
```

```
                if a && b && a<512 && b<512 && it==2

                    rr=rr+r;
                    im1(uint16(b),uint16(a)) = 0;
%place black dot at found point, used for quality testing, commented
out in final version for speed

                end
                xx=xx+uint32(b);
                yy=yy+uint32(a);                          %sum up
edgepoints to improve center position for next frame
            end
            x(n)=xx/number;
            y(n)=yy/number;                         %sum of edge point
positions divided by their number -> new center
            end

            rdata(track)=rr/number/n;


                for a=y(n)-3:y(n)+3
                    for b=x(n)-3:x(n)+3
                        im1(b,a) = 0;              %draw black
square at center of vesicle, commented out for speed.
                    end
                end

                figure(1), imshow(im1)

    imcell{n}=im1;
end

go=1;       %If script was not interupted, make sure data is saved
on next run.
```

Appendix B: Image enhancement

Over time the image quality of the microscope deteriorated, likely due to dust buildup in the optic system. Dirt on the lenses would distort the laser and lead to an uneven illumination of the sample. Washing of the lenses was cumbersome, largely ineffective and always carries the risk of damaging the sensitive optical equipment. As a possible quicker intermittent solution digital image enhancement was attempted. The uneven illumination meant a more or less stable background of artifacts superimposed on the dynamic patterns of the monolayer.

A monolayer in the liquid expanded phase far removed from the phase coexistence regions is believed to be completely homogenous and anisotropic. A picture recorded of this phase will therefore be featureless except for the artifacts of the system. On the large scale the edges will be darker than the center both because of reduced laser intensity of center and because of possible vignetting in the recording part of the optical system. The laser intensity profile is Gaussian and therefore brightest in the middle. In addition to this there is the small scale variations of the laser because of dirty lenses. In some places the illumination intensity is larger than others and therefore the fluorophores will emit more light making the image of these parts brighter than others even though the fluorophore concentration is the same.

In order to enhance visibility of the real (variation in fluorophore concentration) features an image is recorded in the LE phase before each experiment and used that as a standard for comparison of the images from the actual experiment. If the photon count of each pixel is divided by that pixels count from the reference picture, that makes the non-artifact features can be made more visible. If we assume that both the fluorophores response to excitation light and the cameras response to collected light are linear (half excitation intensity will give half emitted fluorescence giving half the intensity on the image) then the artifacts should be completely removed, the brightness of each pixel being directly proportional to the amount of fluorophore present at the corresponding point.

This approach is complicated by several problems. The cameras response function is not linear. At the very least it has a dark count. Even in the complete absence of light thermal fluctuations will make the CCD chip give nonzero counts. If this is simply a fixed background added to the optic count, then it should be subtracted from both the data pictures and the reference picture before dividing. If this is not done it will reduce contrast in the areas that are naturally dark.

Of course the actual number of photons registered at a pixel is stochastic in nature. That means one can never know the exact right amount to subtract. These

stochastics of course add noise to any picture, where it becomes a problem is when the intensity is very low. Due to vignetting and reduced laser intensity, the edges of the field of view are pretty much black. Before the image is enhanced these areas are naturally disregarded as dark and containing no data, but when the enhancement is done on such an area the return is basically zero divided with zero. The result is that random fluctuations determine if such a pixel is completely white or completely black. This makes for a very esthetically unpleasing appearance. In order to make more pleasing pictures the scheme can be adjusted slightly so that the areas containing no data remain dark. Yet this method has clearly been capable of revealing actual features in an area that looked black in the raw data, so a compromise has to be made between squeezing the picture for the last bit of field of view and not giving it unnecessary noisy edges with no information.

The following equation describes all the ways this was attempted tweaked to give the resultant picture R:

$$R = a\frac{(I - D_I)}{(R - D_R)} + k \qquad \text{Eq. B.1}$$

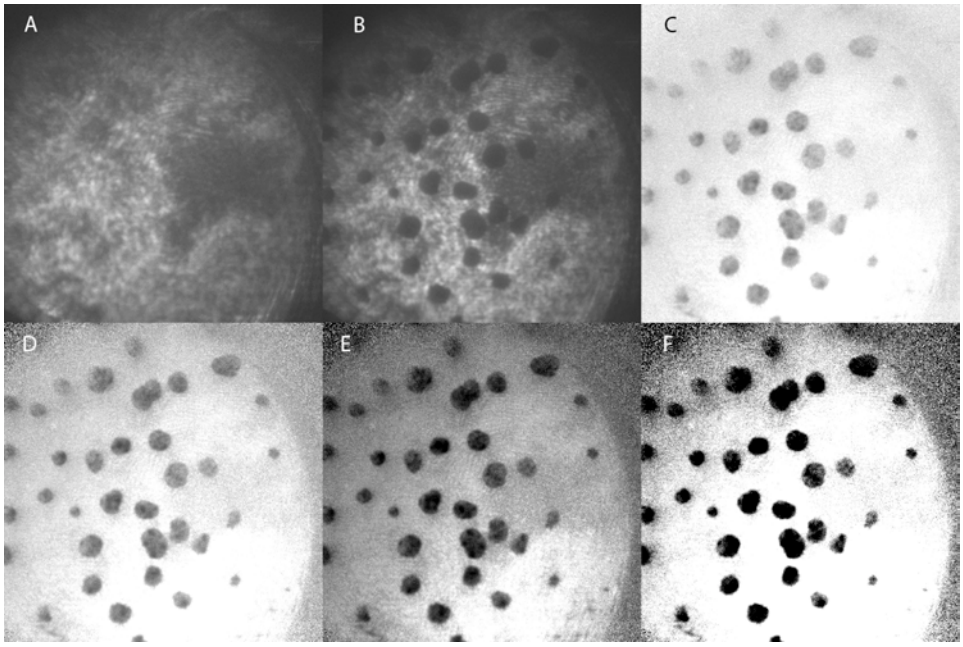

Figure 64: Various attempts at image enhancement. A: Featureless reference image. B: Raw data. C: Simple division of A and B. D: D_I and D_R equal to 30. E: As D but darkened by setting k = -0.3. F: As D with contrast enhanced by setting a=3 and k=-1.5.

With free parameters a, k D_i and D_R I is the recorded image data, R is the reference data D_i is the dark count subtracted from the original, D_R is the dark

count subtracted from the reference, this is not necessarily the same as D_i and would generally be set a bit to low to avoid dividing by zero anywhere. By setting an a>1 and a negative k contrast is enhanced.

The patterns formed by the laser varies with the distance from the objective, this means that if the focus has been moved just a little bit then the reference picture does not mach the artifacts perfectly, even if the movement is small enough that the picture is still focused. In a monolayer experiment water is always evaporating, moving the focus, meaning that the uncompensated artifacts gradually gets worse.

In order to keep the compensation optimal it was attempted to write a script that would continually update the reference. In most of these experiments any feature, whether they be LC phase or gas phase, always shows up as dark areas on the more or less homogenous LE background. By increasing contrast a lot and smoothing the picture slightly it was possible to consistently identify domain regions automatically. Then the domains and a margin around them could be excluded and the rest used to update the background reference. Given that the domains move around, every part of background would get updated eventually. Giving a possibility of better looking, easier to follow movies.

Appendix C: Numerical calculation of field around electrode

In order to find the field surrounding the electrode in the domain electrophoresis experiment, the electrode was treated like an infinite conducting vertical cylinder of radius r terminating at height h, and the Langmuir through like an infinite conducting plane at height zero. These define a boundary condition of potential V and 0 respectively. In between the potential φ is found by the Laplace equation.

Since the problem is cylindrically symmetric the problem reduces to finding φ as a function of the coordinates ρ and z. The Laplace equation then takes the form:

$$\nabla^2\varphi = \frac{1}{\rho}\frac{\partial}{\partial\rho}\left(\rho\frac{\partial\varphi}{\partial\rho}\right) + \frac{\partial^2\varphi}{\partial z^2} = 0 \qquad \text{Eq. C.1}$$

In order to solve this numerically a discrete matrix of points is set up. Here the derivative of a function F can be approximated by:

$$\frac{dF(x)}{dx} \approx F(x+\tfrac{1}{2}) - F(x-\tfrac{1}{2}) \qquad \text{Eq. C.2}$$

A double derivative will therefore become:

$$\frac{d^2F(x)}{dx^2} \approx F(x+1) + F(x-1) - 2F(x) \qquad \text{Eq. C.3}$$

And similarly:

$$\frac{1}{\rho}\frac{\partial}{\partial\rho}\left(\rho\frac{\partial\varphi(\rho)}{\partial\rho}\right) \approx \left(1+\frac{1}{2\rho}\right)\varphi(\rho+1) + \left(1-\frac{1}{2\rho}\right)\varphi(\rho-1) - 2\varphi(\rho) \qquad \text{Eq. C.4}$$

Putting it all together and solving for $\varphi(\rho,z)$ yields the following expression:

$$\varphi(\rho,z) = \tfrac{1}{4}\cdot\left(\varphi(\rho,z-1) + \varphi(\rho,z+1) + (1+\tfrac{1}{2\rho})\varphi(\rho+1,z) + (1-\tfrac{1}{2\rho})\varphi(\rho-1,z)\right) \qquad \text{Eq. C.5}$$

in which potential at each point is a function of the potentials at the for points around it in the discrete matrix. In order to use this to calculate the potential in a finite area, the boundary conditions need to be defined. Apart from the boundary conditions of the trough and the electrode, the potential was set to zero at a large but finite ρ, at a similarly large but finite z the potential was assumed to no longer be changing with z. At ρ = 0 there is a coordinate singularity at which eq. C.5 breaks down, so here the potential was calculated with a cartesian approximation:

$$\varphi(0,z) = \tfrac{1}{6} \cdot \left(\varphi(0,z-1) + \varphi(0,z+1) + 4\varphi(1,z)\right) \qquad \text{Eq. C.6}$$

φ was then iterated until it no longer changed appreciably. The electric field E was calculated as the gradient of phi. Then the magnitude of the field at z=0 were differentiated with respect to ρ to find the field gradient working on the domains in the monolayer.

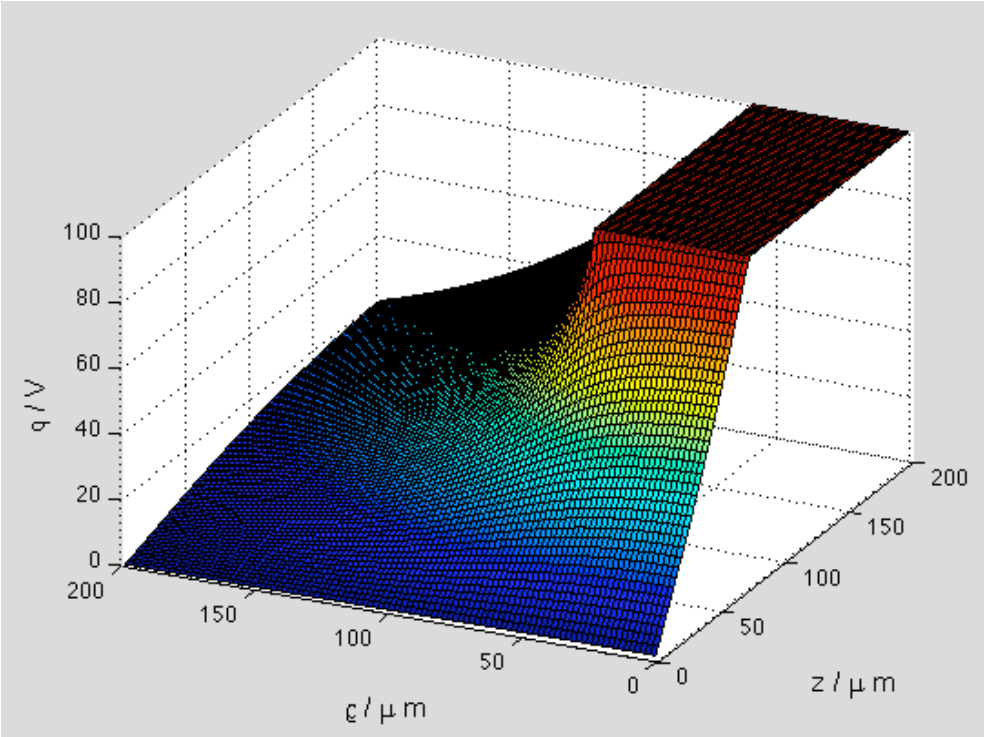

Figure 65: Calculated electric potential as function of z and **ρ**. The E field in Figure 66 is calculated as the absolute value of the gradient of this function. The actual simulated area is five times bigger in both **ρ** and z.

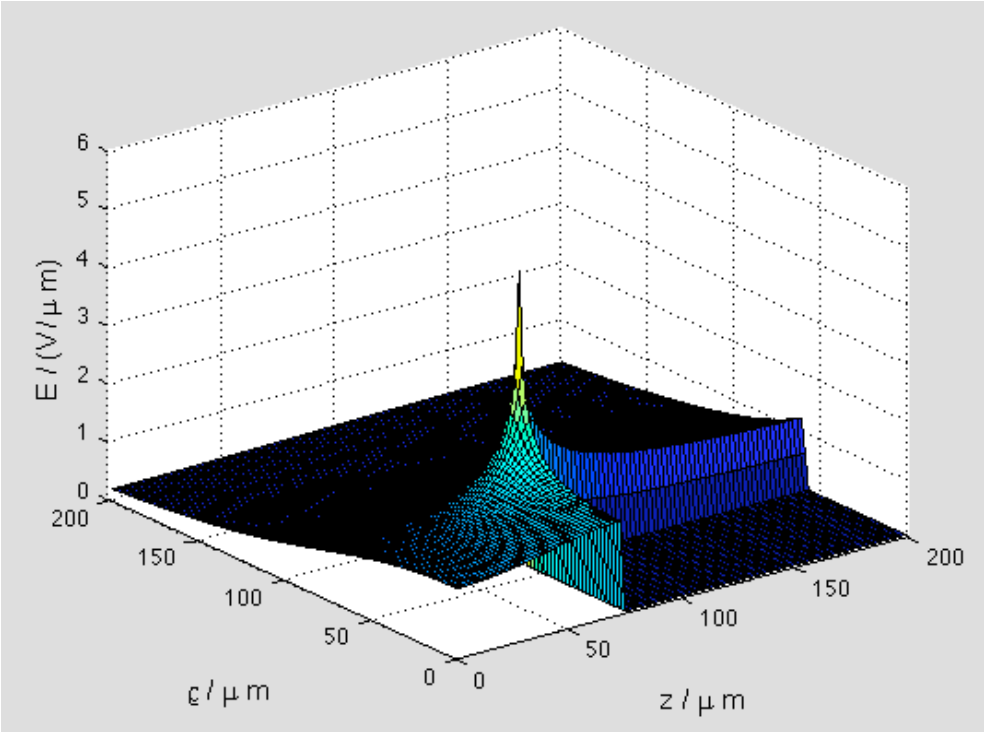

Figure 66: Calculated magnitude of electric field E as function of z and ρ. As expected the field is nearly independent of z at large z and drops close to zero for large ρ confirming the validity of these boundary conditions. The simulated area is five times larger in both z and ρ than what is shown here. Close to the sharp edge of the cylindrical electrode the field reaches a very large value, and between the electrode and the sample it is close to uniform. The curve in the z=0 plane is differentiated and used to calculate the theoretical line in Figure 42.

Appendix D: Gallery

The following is a gallery of interesting pictures, which were recorded over the years, but didn't fit into the thesis itself due to lack of analysis or relevance; nevertheless are interesting enough, or contain enough beauty that it would be a shame not to share them. They illustrate how immensely complicated the world of Langmuir monolayers is when one looks closely.

LE/Gas phase:

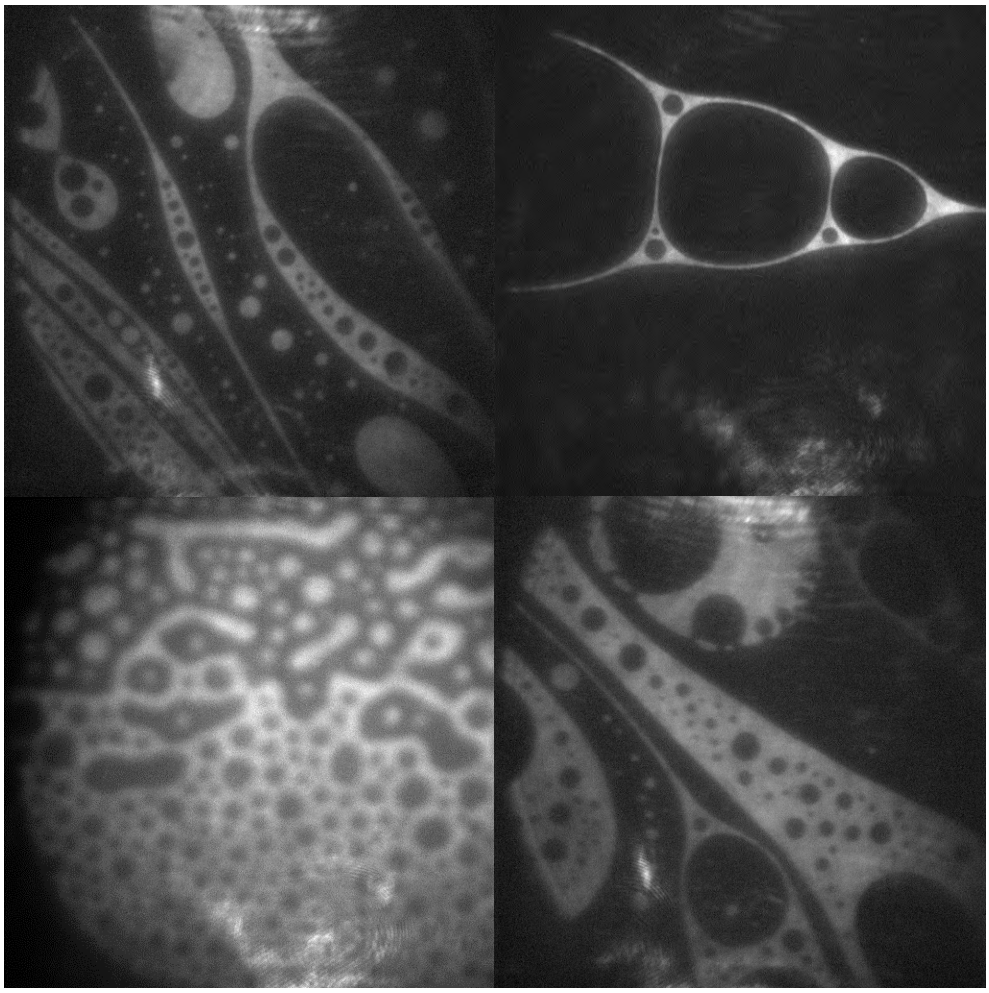

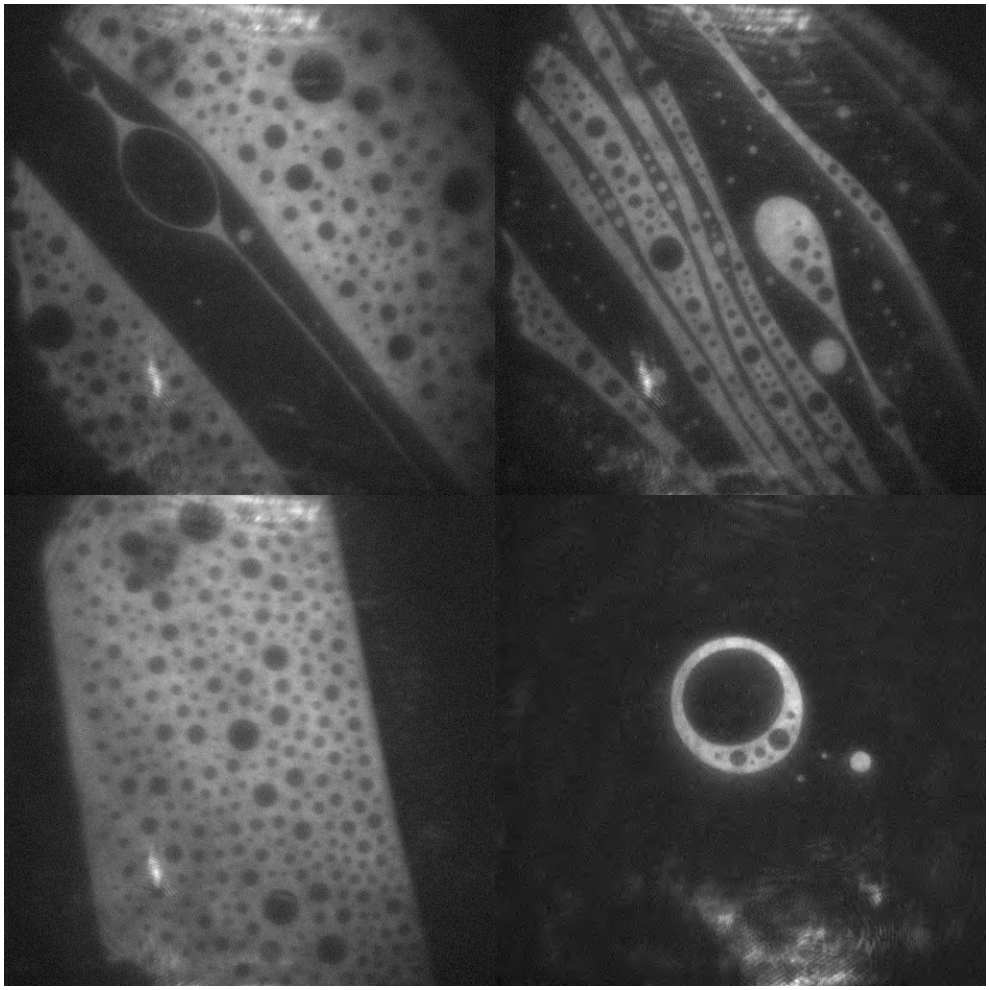

LE-LC phase:

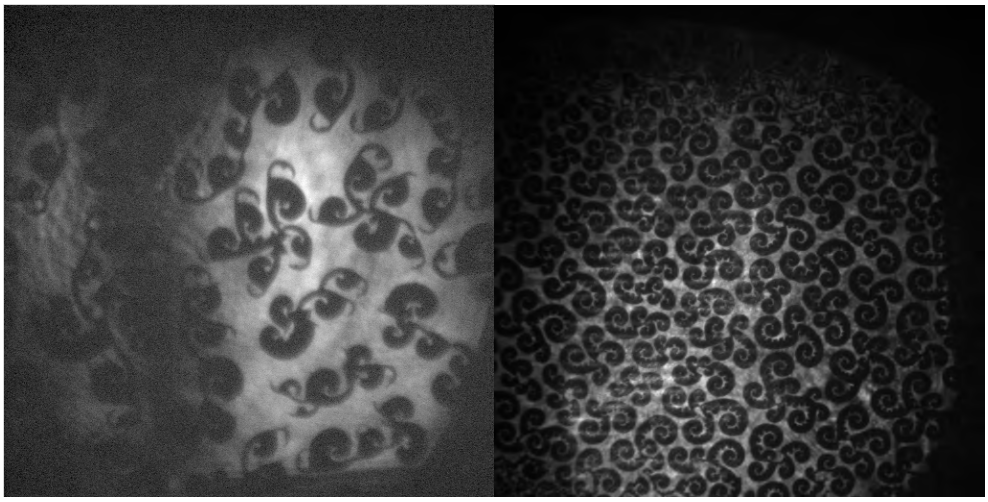

References

Aragón, S. R. & Pecora, R. (1976): “Fluorescence Correlation Spectroscopy as a Probe of Molecular Dynamics.” Journal of Chemichal Physics 64, p. 1791-1803.

Ashkin, A. (1970): “Acceleration and Trapping of Particles by Radiation Pressure.” Physical Review Letters 24, p. 156.

Ashkin, A & Dziedzic, J. M. (1971): “Optical Levitation by Radiation Pressure.” Applied Physics Letters 19, p. 283.

Ashkin, A., Dziedzic, J. M., Bjorkholm, J. E. & Chu, S. (1987): “Observation of a single-beam gradient force optical trap for dielectric particles.” Optics Letters 11 5, p. 288-290.

Batchinski, A. J, (1913): "Untersuchungen über die innere Reibung der Flussigkeiten." Zeitschrift für Physikalische Chemie 84, p. 643.

Bayburt, T. H., Grinkova, Y. V. & Sligar, S. G. (2002): “Self-Assembly of Discoidal Phospholipid Bilayer Nanoparticles with Membrane Scaffold Proteins.” Nano Letters 8 2, p. 853-856.

Benedetti, A. Birarelli, A., Brunelli, E., Curatola, G., Ferretti, G., Delprete, U., Jezequel, A. & Orlandi, F. (1987): “Modification of lipid-composition of erythrocyte-membranes in chronic-alcoholism.” Pharmacol Res, 19 10, p. 651–663.

Blicher, A., Wodzinska, K., Fidorra, M., Witherhalter, M. & Heimburg, T. (2009): “The Temperature Dependence of Lipid Membrane Permeability, its Quantized Nature, and the Influence of Anestetics.” Biophysical Journal 96, p. 4581-4591.

Blicher, A. (2011): “Electrical Aspects of Lipid Membranes.” PhD thesis. University of Copenhagen.

Blom, H. (2003): “Correlation Spectroscopy of Single Emitters – Fundamental Studies and Applications Related to Quantum Optics and Life Sciences.” Ph.D Thesis. Department of Microelectronics and Information Technology. Laboratory of Optics, Photonics and Electronics. Stockholm, Royal Institute of Technology KTH.

Cohen, M. H. & Turnbull, D. (1959): "Molecular Transport in Liquids and Glasses." The Journal of Chemical Physics 31 5, p. 1164-1169.

Courty, S., Dollet, B., Elias, F., Heinig, P. & Graner, F. (2003):"Two-dimensional shear modulus of a Langmuir foam." Europhys. Lett., 64 5, p. 709.

Denisov, I. G., Grinkova, Y. V., Lazarides A. A. & Sligar S. G. (2004): "Directed Self-Assembly of Monodisperse Phospholipid Bilayer Nanodiscs with Controlled Size." J. Am. Chem. Soc. 126, p. 3477–3487.

Dennin M. & Knobler, C. M. (1997): "Experimental Studies of Bubble Dynamics in a Slowly Driven Monolayer Foam." Physical Review Letters 78 12, p. 2485.

Douglas S. M., Forstner M. B. & Käs, J. A. (2002): "Apparent Subdiffusion Inherent to Single Particle Tracking." Biophysical Journal, Volume 83, Issue 4, 2109-2117

Doolittle, A. K. (1951): "Studies in Newtonian Flow. II. The Dependence of the Viscosity of Liquids on Free-Space." Journal of Applies Physics 22 12, p. 1471.

Ehrenfest, P (1933): "*Phasenumwandlungen im ueblichen und erweiterten Sinn, classifiziert nach dem entsprechenden Singularitaeten des thermodynamischen Potentiales*" Verhandlingen der Koninklijke Akademie van Wetenschappen (*Amsterdam*) 36, p. 153–157

Einstein, A. (1905): "The motion of elements suspended in static liquids as clamied in the molecular kinetic theory of heat." Annalen der Physik. 17 8, p. 549-560.

Fick, A. (1855): "Ueber Diffusion." Annalen der Physik. 170 1, p. 59-86.

Fischer, T. M. & Lösche, M. (2004): "Pattern Formation in Langmuir Monolayers Due to Long-Range Electrostatic Interactions." Lect. Notes Phys. 634 p. 383.

Flörsheimer, M. & Möhwald, H. (1989): "Development of equilibrium domain shapes in phospholipid monolayers." Chemistry and Physics of Lipids, 49, p. 231-241.

Flörsheimer, M. & Möhwald, H. (1990): "Growth of Large Liquid Crystalline Domains of Phospholipids at Air-Water Interfaces." Thin Solid Films 189, p. 379-387.

Galvani L (1791): "*De viribus electricitatis in motu musculari commentarius*". Bon Sci. Art Inst. Acad. Comm. 7, p. 363–418

Gorter, E. M. D &Grendel, F. (1925): "On bimolecular layers of lipoids on the

chromocytes of the blood." The Journal of Ewperimental Medicine 41, p 439-443.

Guck, J., Ananthakrishnan, R., Mahmood, H., Moon, T. J., Cunningham, C. C. & Käs, J. (2001): "The Optical Stretcher: A Novel Laser Tool to Micromanipulate Cells." Biophysical Journal 81 2, p. 767–784.

Guck, J., Ananthakrishnan, R. & Cunningham, C. (2002): "Stretching biological cells with light." Journal of Physics-Condensed Matter 14 19, p. 4843-4856.

Gudmand, M. (2008): "Phase Behaviour and Enzyme Dynamicsat the Lipid-Water Interface." Niels Bohr Institute, University of Copenhagen. Ph.D Thesis.

Hac, A. (2003): "Diffusion process in membranes containing coexisting domains investigated by fluorescence correlation spectroscopy." Max Planck Institute (Göttingen) / Niels Bohr Institute (University of Copenhagen). Ph.D. Thesis.

Hazel, J. & Williams, E. (1990): "The role of alterations in membrane lipid-composition in enabling physiological adaptation of organisms to their physical-environment." Prog Lipid Res, 29 3, p. 167–227.

Heckl, W. M., Miller, A. & Möhwald, H. (1988): "Electric-Field-Induced Domain Movement in Phospholipid Monolayers." Thin Solid Films, 159, p. 125-132.

Heimburg, T. & Jackson, A. D. (2005a): "Mechanical Aspects of Membrane Thermodynamics. Estimation of the Mechanical Properties of Lipid Membranes Close to the Chain Melting Transition From Calorimetry." Biochimica Et Biophysica Acta-Biomembranes, 1415, p. 147.

Heimburg, T. & Jackson, A. D. (2005b): "On soliton propagation in biomembranes and nerves." PNAS 102 28, p. 9790-9795.

Heimburg, T. (2007a): "Thermal biophysics of membranes." Wiley-VCH, Berlin, 1st edition.

Heimburg T. & Jackson, A. D. (2007b): "The Thermodynamics of General Anesthesia." Biophysical Journal 92, p. 3159–3165.

Heinig, P., & Fischer, T. M. (2003): "Dipolar Foams in Langmuir Monolayers Dry at Low Bubble Fraction." J. Phys. Chem. B 107, p. 11757.

Hess S. T. & Webb, W. W. (2002): "Focal Volume Optics and Experimental Artifacts in Confocal Fluorescence Corelation Spectroscopy." Biophysical Journal 83 4 (2002), p. 2300-2317.

Hewson, W. (1773): “On the Figure and Composition of the Red Particles of the Blood Commonly Called the Red Blood Globules.” Philosophical Transactions 63, p. 306-324.

Hodgkin, A. L. and Huxley A. F. (1952): “*Propagation of Electrical Signals Along Giant Nerve Fibres*” Proceedings of the Royal Society of London B, 140 899, p.177-183

Hossain, M. M., Suzuki, T., Limura, K. and Kato, T. (2006): “Kinetic Appearance of First-Order Gas-Liquid Expanded and Liquid Expanded-Liquid Condensed Phase Transitions below the Triple Point.” Langmuir 22, p. 1074.

Holmberg, K., Jonsson, B., Kronberg, B. and Lindman, B. (2006): “*Surfactants and Polymers in Aqueous solution 2Edition*” Wiley.

Jaeger, G. (1997): “*The Ehrenfest Classification of Phase Transitions: Introduction and Evolution*” Archive for History of Exact Sciences 53 1, p. 51-81

Johnson, M. J., Majmudar, C., Skolimowski J. J. & Majda, M. (2001): “Critical Temperature and LE/G Phase Transitions in Monolayer Films of the Amphiphilic TEMPO Derivatives at the Air/Water Interface.” J. Phys. Chem. B 105, p. 9002.

Kaganer, V. M., Möhwald, H. & Dutta, P. (1999): “Structure and Phase Transitions in Langmuir Monolayers.” Reviews of Modern Physics 71 3.

Kastrup, L., Blom, H., Eggeling c. & Hell, W. S. (2005): “Fluorescence Fluctuation Spectroscopy in Subdiffraction Focal Volumes.” Physical Review Letters 94, p. 178104.

Kelsall, R. W., Hamley, I. W. and Geoghegan M. (2005): “*Nanoscale Science and Technology*” Wiley.

Knecht, V., Müller, M., Bonn, M., Marrink, S. J. & Mark, A. E. (2005): “Simulation studies of pore and domain formation in a phospholipid monolayer”. The Journal of Chemical Physics. 122 p. 24704.

Knobler, C. M. (1990): “Seeing Phenomena in Flatland: Studies of Monolayers by Fluorescence Microscopy”. Science 249, p. 870.

Koker, R. & McConnell, H. M. (1994): “Shape Transitions of Lipid Monolayer Domains in an External Field”. J. Phys. Chem. 98, p. 5389.

Lautrup, B., Jackson, A. & Heimburg, T. (2005): “The Stability of Solitons in Biomembranes and Nerves”.

Lee, D. W., Min, Y., Dhar, P., Ramachandran, A., Israelachvili, J. N. & Zasadzinski, J. A. (2011): “Relating domain size distribution to line tension and molecular dipole density in model cytoplasmic myelin lipid monolayers.” PNAS 108 23, p 9425-9430.

Li, L., Köpf, M. H., Gurevich, S. V., Friedrich, R. & Chi, L. (2012): “Structure Formation by Dynamic Self-Assembly” Small 8 4, p. 488–503.

Lösche, M., Sackmann, E. & Möwald, H. (1993): “A Fluorescensce Microscopic Study Concerning the Phase Diagram of Phospholipids”. Ber. Bunsenges. Phys. Chem. 87 , p. 848.

Mann, E. K. & and Primak, S. V. (1999): “Stability of Two-Dimensional Foams in Langmuir Monolayers”. Physical Review Letters 83 25.

Mabrey, S. & Sturtevant, J. (1976): “Investigation of phase-transitions of lipids and lipid mixtures by high sensitivity differential scanning calorimetry.” P National Acadademi of Science Usa, 73 11, p. 3862–3866.

Magde, D., Elson, E. L. & Webb, W. W. (1974): "Fluorescence Correlation Spectroscopy. II. An Experimental Realization." Biopolymers 13 1, p. 29-61.

McConnell, H. M. (1989): “Theory of hexagonal and stripe phases in monolayers.” Proc. Natl. Acad. Sci. 86, p. 3452.

Menz, W., Mohr, J. & Paul, O. (2001): “Microsystem Technology.” 2nd ed., Wiley-VCH, Weinheim, Germany.

Meyer H. H. (1901): “*Zur Theorie der Alkoholnarkose. Der Einfluss wechselnder Temperature auf Wirkungsstärke und Theilungscoefficient der Narcotica*” Arch. Exp. Pathol. Pharmakol. 46, p. 338–346

Miller, A. & Mohwald, H. (1986): “Collecting Two-Dimensional Phospholipid Crystals In Inhomogeneous Electric Fields.” Europhysics Letters 2, p. 67-74.

Muruganathan, R. M., Khattari, Z. & Fischer, T. M. (2005): “Nonequilibrium Bubbles in a Flowing Langmuir Monolayer.” J. Phys. Chem. B 109, p. 21772.

Möhwald, H. (1990): “Phospholipid and Phospholipid-Protein Monolayers at the Air/Water Interface.” Annu. Rev. Phys. Chern. 41, p. 441.

Overton, E. (1899): “On the general osmotic properties of the cell, their probable origin, and their significance for physiology.” Vierteljahrschrift der Naturforschende Gesselschaft (Zurich) 44, p. 88-135.

Overton C. E. (1901): “*Studien über die Narkose zugleich ein Beitrag zur allgemeinen Pharmakologie*” Gustav Fischer, Jena, Switzerland. English: C.E. Overton (1990) “*Studies of Narcosis*” Chapman and Hall, London

Parmahamsa, M., Reddy, K. & Varadacharyulu, N. (2004): “Changes in composition and properties of erythrocyte membrane in chronic alcoholics.” Alcohol Alcoholism, 39 2, p. 110–112.

Paula, S., Volkov, A., & Deamer, D. (1998): “Permeation of Halide Anions Through Phospholipid Bilayers Occurs by the Solubility-diffusion Mechanism.” Biophysical Journal, 74 1, p. 319-327.

Petty, M. C. (1996): “*Langmuir-Blodgett Films: An Introduction*” Cambridge University Press.

Porter, E. F. (1937): “Monomolecular Films of α-Aminostearic Acid, Stearic Acid, and Heptadecylamine.” J. Am. Chem. Soc., 59, p. 1883-1888.

Raschle, T., Hiller, S., Etzkorn M. & Wagner, G. (2010): “Nonmicellar systems for solution NMR spectroscopy of membrane proteins.” Current Opinion in Structural Biology 20 4, p. 471–479.

Remmerbach, T. W., Wottawah, F., Dietrich, J., Lincoln, B., Wittekind, C. & Guck, J. (2009): “Oral Cancer Diagnosis by Mechanical Phenotyping.” Cancer Research 69 5, p. 1728-1732.

Rigler, R., Mets, Ü., Widengren, J. & Kask, P. (1993): “Flourescence Correlation Spectroscopy With High Count Rate and Low Background: Analysis of Translational Diffusion.” European Biophysics Journal 22 3, p. 169-175.

Saxton, M. J. (1997) “Single-Particle Tracking: The Distribution of Diffusion Coefficients.” Biophysical Journal 72, p. 1744-1753.

Saxton, M. J. (2007): “A Biological Interpretation of Transient Anomalous Subdiffusion. I. Qualitative Model.” Annual Review of Biophysics and Biomolecular Structure. 26, p. 373-399.

Siegel S. & Vollhardt, D. (1996): “Foam-like patterns in myristyl alcohol monolayers.” Colloids Surfaces A: Physicochem. 116, p. 195.

Singer, S. J. and G. L. Nicolson (1972). "The Fluid Mosaic Model of the Structure

of Cell Membranes" Science **175** 4023, p. 720-731.

Stamou, D. & Duschl, C. (2000): “Long-range attraction between colloidal spheres at the air-water interface: The consequence of an irregular meniscus.” Phys. Rev. E 62, p. 5263.

Stamou, D., Duschl, C., Delamarche, E. & Vogel, H. (2003): “Self-Assembled Microarrays of Attoliter Molecular Vessels.” Angewandte Chemie 115 45, p. 5738–5741.

Stine, K. J., Rauseo, S. A., Moore, B. G., Wise, J. A. & Knobler, C. M. (1990): “Evolution of foam structures in Langmuir monolayers of pentadecanoic acid.” Physical Review A 41 12, p. 6884.

Sugar, I. (1979): “Theory of the Electric Field-Induced Phase-Transition of Phospholipid-Bilayers.” Biochim Biophys Acta, 556 1 (1979), p. 72–85.

To, K., Akamatsu, S. & Rondelez, F. (1993): “Stripe Phase in the Gas-Liquid Coexistence Region of Langmuir Monolayers.” Europhys. Lett., 21 31, p. 343.

Vogel, V. & Möbius, D. (1988): “Local surface potentials and electric dipole moments of lipid monolayers: Contributions of the water/lipid and the lipid/air interfaces.” Thin Solid Films, 1 59, p. 73.

Wadsäter, M., Simonsen, J. B., Lauridsen, T., Tveten, E. G., Naur, P., Bjørnholm, T. Wacklin, H., Mortensen, K., Arleth, L., Feidenhans’l, R. & Cardenas, M. (2011): “Aligning Nanodiscs at the Air_Water Interface, a Neutron Reflectivity Study.” Langmuir 27, p. 15065–15073.

Widengren, J., Metsand U□. & Rigler, R. (1995): “Fluorescence Correlation Spectroscopy of Triplet States in Solution: A Theoretical and Experimental Study.” J. Phys. Chem. 99, p. 13368.

Wurlitzer, S., Steffen, P. & Fischer; T. M. (2000): “Line tension of Langmuir monolayer phase boundaries determined with optical tweezers.” J. Chem. Phys. 112, p. 5915.

Yee, K., Lee, C. & McConnell, H. M. (1995): “Effect of Electric Field Gradients on Lipid Monolayer Membranes.” Biophysical Journal 68 p. 1740.

Yoneyama, M., Fujii, A., Maeda, S. & Murayama, T. (1992):“Light-Induced Bubble-Stripe Transitions of Gaseous Domains in Porphyrin Langmuir Monolayers.” J. Phys. Chem. 96, p. 8982.

Zou, L., Bernoff, A. J., Mann, J. A., Alexander, Jr. J. C. & Mann, E. K. (2010):. “Gasous Hole Closing in a Polymer Langmuir Monolayer.” Langmuir 26 5, p. 3232.